DEPARTMENT OF PHYSICS
UNIVERSITY OF JYVÄSKYLÄ
RESEARCH REPORT No. 10/2015

DETAILED SPECTROSCOPY OF THE NEUTRON-DEFICIENT BISMUTH ISOTOPES ^{193,195}Bi

by

Andrej Herzáň

Academic Dissertation
for the Degree of
Doctor of Philosophy

To be presented, by permission of the
Faculty of Mathematics and Science
of the University of Jyväskylä,
for public examination in Auditorium FYS-1 of the
University of Jyväskylä on December 17, 2015
at 12 o'clock noon

Jyväskylä, Finland
December 2015

Preface

"I learned very early the difference between knowing the name of something and knowing something." And colleagues and friends that I have met at the Department of Physics of the University of Jyväskylä have greatly contributed to my understanding of "something". Hereby I would like to express my endless gratitude to my supervisors Doc. Sakari Juutinen and Prof. Rauno Julin, who have been the extraordinary teachers to me all the time. You opened many doors for me and let me pass through them. Each time it meant a new challenge. It made my will stronger and insight into world of nuclear physics deeper.
I had the privilege to become a member of the Nuclear Spectroscopy group in 2009 (`GAMMA` group at that time). And I must say I truly enjoyed all those years working with you, because no matter what, you all have been welcoming and helpful from the very first moment. Dr. Steffen Ketelhut and Dr. Pauli Peura were great support to me especially during my first year at JYFL. Pauli, the time you devoted to helping me with `JAVA` coding is greatly appreciated. I am also thankful to the "astatine/bismuth" crew for fruitful discussions and new ideas which pushed the data analysis forward and helped with solving many peculiarities. Mr. Juha Sorri and Mr. Janne Laulainen, it was a pleasure to share the office with you. You always made the time spent at work comfortable.
Going even further into the past, I owe a lot to Dr. Martin Venhart. It has been some time since we first met. And I believe I am not wrong when I say that I would not be writing these lines without meeting you, as I would have most likely ended up at somewhere completely different place. Thank you so much for telling me about Jyväskylä!
My family was unstoppable in their great support and kind words in every moment we were together. Thank you! To be alone, one thousand and five hundred kilometers from home, far away from all the people you have spent previous 24 years with, may be extremely difficult. Especially, if you add dark cold days of very long winter. One person always makes them bright and warm. You make me feel happy and put a smile on my face each time I see you or hear you. Even though, and I am pretty sure about it, the waiting was certainly not easy for you, since I was coming back to you so rarely. I know that the words cannot be enough to say how grateful I am, my beautiful Love Ivka!

Andrej Herzáň
Jyväskylä, November, 2015

Acknowledgements

This work was supported by the Academy of Finland under the Finnish Centre of Excellence Programme (Nuclear and Accelerator Based Physics Research at JYFL), ENSAR resources and National Graduate School in Particle and Nuclear Physics. The author would also like to thank the GAMMAPOOL European Spectroscopy Resource for the loan of germanium detectors for JUROGAM II array.

Abstract

Herzáň, Andrej
DETAILED SPECTROSCOPY OF THE NEUTRON-DEFICIENT BISMUTH ISOTOPES ^{193,195}Bi
Jyväskylä: University of Jyväskylä, 2015, 119 p.
Department of Physics Research Report No. 10/2015
ISSN: 0075-465X; 10/2015
ISBN: 978-951-39-6438-2 (paper version)
ISBN: 978-951-39-6439-9 (electronic version)
Diss.

Two experiments aiming to study the shape coexistence and competing structures in ^{193}Bi and ^{195}Bi isotopes have been performed at the Accelerator laboratory of the University of Jyväskylä, Finland (JYFL). Many new states have been found, hugely extending the previously known level schemes for both isotopes. The $\pi i_{13/2}$ bands were extended up to $I^{\pi} = 45/2^{+}$ in both the ^{193,195}Bi isotopes. In case of ^{193}Bi, the $I^{\pi} = 31/2^{+}$ member of the $\pi i_{13/2}$ band was found to de-excite also to a long-lived isomeric state. This link determines the energy of the isomeric state to be 2350(1) keV and suggests a spin and parity of $29/2^{+}$. The half-life of the isomeric state was measured to be 85(3) μs. A level structure on top of this isomeric state was constructed. The newly observed 49 keV $E2$ transition provides a link between the $(29/2^{-})$ isomeric state and lower-lying structures in ^{193}Bi. A superdeformed band almost identical to that present in the neighboring isotope ^{191}Bi has been identified. Both the $29/2^{+}$ and $(29/2^{-})$ isomeric states, together with the full decay-paths have also been identified in ^{195}Bi. In both isotopes, the decay cascades from $31/2^{+}$ states to the $29/2^{+}$ isomeric states are surprisingly similar. Compared to ^{193}Bi, measured half-lives of these isomeric states are considerably shorter in ^{195}Bi. Experimental evidence is given proving the smaller quadrupole deformations in ^{195}Bi when compared to ^{193}Bi nucleus. Moreover, several new rotational collective structures have been identified in ^{195}Bi, even though their variety is not as rich as in ^{193}Bi. This is the first time the collective structures have been observed up to a high spins and excitation energies in ^{195}Bi. Strong manifestation of shape coexistence is thus proved to be present also in ^{195}Bi.

Keywords: γ-ray spectroscopy, recoil-decay tagging, isomer tagging, shape coexistence, superdeformation

Author's address Andrej Herzáň
Department of Physics
University of Jyväskylä
Finland

Supervisors Doc. Sakari Juutinen
Department of Physics
University of Jyväskylä
Finland

Prof. Rauno Julin
Department of Physics
University of Jyväskylä
Finland

Reviewers Prof. Mark A. Riley
Department of Physics
Florida State University
United States of America

Dr. Martin Venhart
Institute of Physics
Slovak Academy of Sciences
Slovakia

Opponent Prof. Filip Kondev
Physics Division
Argonne National Laboratory
United States of America

Contents

Chapter 1

Introduction

In the 5^{-th} century B.C, ancient philosophers Démokritos and Leukippos came up with an idea that all entities in the universe are in their nature a substance, which consists of many single, indestructible particles - *atoms* (*gr. atomos*). It was the very beginning of the *atomic era*. Long time passed, until chemist and physicist John Dalton revived the honorable idea and became a founder of the *atomistic theory* in the beginning of the 19^{-th} century, stating that all atoms of one nuclide have the same atomic weight. This lead to postulating the *conservation of mass law* in the chemical reactions. The year 1896 truly has its exceptional place in the history of science, since the experiments with uranium salts and photographic plates performed by Henry Becquerel lead to the discovery of *nuclear radiation*, or as it is commonly called nowadays - *radioactivity*. Following this amazing observation, Marie Curie initiated experiments in order to reveal the nature of the radioactivity. For their groundbreaking work, H. Becquerel, M. Curie and her husband P. Curie were awarded a Nobel Prize in 1903. Shortly after, in 1908, the Lord Rutherford of Nelson, the great scientist responsible for discovery of atomic nucleus, was awarded a Nobel Prize for explaining the concept of radioactivity. Since then, huge progress has been made in the field of nuclear physics. Not only that we now know much more about the structure of the nucleus itself, but humankind was also able to use and implement it in different technologies, which we consider to be common nowadays.

Considering the atomic nuclei, many of their aspects can be studied. One way of looking at the nucleus is to study its gross features, *e.g.* shape, rotational and/or vibrational motion, decay modes etc. Behavior of these single particle and/or collective features of a wide range of nuclei is usually stored in the energy and time spectra measured by state-of-the-art experimental setups. Close examination of such spectra often reveals unexpected features of the nuclei,

which may then set a new milestone in nuclear research as such. The methodology just mentioned is commonly known as *nuclear spectroscopy*. It uses a set of different techniques, many of which are also applied on the data sets of the present study, and more explanation about those is provided later in the text.

To this date, thousands of isotopes have been identified. On the basis of systematic studies performed so far, it has been found that many observable properties of nuclei vary as a function of the proton and/or neutron number. In accordance to these observations, nuclides have been grouped to form regions exhibiting specific features (α decay, β^+ / β^- decay, EC, prolate / oblate shape, enhanced stability etc.). Focus of the present work is aimed at study of the proton-rich isotopes in the vicinity of the proton magic number $Z = 82$. The region around the $Z = 82$ proton number has been under intense investigation for many years, and even today, many nuclei still remain to be investigated. It is mainly the isotopes along the proton dripline, where the cross-sections and proton, or even two proton evaporation process limit the knowledge about these isotopes, despite the advanced spectroscopic tools available today. On the other hand, neutron-deficient $Z \approx 82$ nuclei near the neutron mid-shell are rich in cases, in which coexisting deformed configurations at low excitation energies have been observed [Heyde81, Julin01]. In nuclear reactions, it is not always necessary to populate the corresponding nuclei to very high spin, since *shape coexistence* is predominantly defined by low-lying excited states associated with a variety of nuclear shapes. The only exception may be superdeformation, or even hyperdeformation observed in some atomic nuclei [Galindo93, Krasznahorkay98].
The bismuth nuclei are of interest as they have only one extra proton coupled to the $Z = 82$ proton magic lead core. It is therefore desirable to perform investigations of shape coexistence and studies of the isomeric states built on multiquasiparticle configurations. The odd-A ^{193}Bi and ^{195}Bi isotopes of the present work turn out to be prime examples of the structural changes in atomic nuclei. Until the present study, very limited spectroscopic information on ^{195}Bi was available [Lonnroth86, Pai12], and both the ^{193,195}Bi isotopes were believed to lie in the transitional region between lighter very neutron-deficient odd-A prolate bismuth nuclei [Hurstel02] and heavier odd-A bismuth isotopes with the absence of any regular band-like structures for the low-lying states [Hubel78, Piel85, Mabala05].

The richness of the variety of shapes in specific regions of the chart on nuclei extends even further. A superdeformed (SD) nucleus forms an ellipsoid shape with axes in ratios of approximately 2:1:1. The first experimentally observed SD states were the low-spin states of fission isomers of elements in the actinide and lanthanide series. Superdeformed band was first time observed in ^{152}Dy. Superdeformation has now been found in several regions of the nuclear chart, in nuclei around A = 60, A = 80, A = 130, A = 150 and A = 190. The extremes of angular momentum and deformation represented by SD nuclei have provided a new testing-ground for the standard nuclear models, which had been well

examined for lower spins and "normal" (lower) deformations. Experimental evidence for a new region of superdeformation near A = 190 first became available in 1989, when a weak rotational band of twelve transitions was observed in the nucleus ^{191}Hg [Carpenter90]. A large quadrupole deformation $\beta_2 \approx 0.5$ was assigned to this SD band based on the measured average quadrupole moment of 18±3 eb. Since then, more than 40 SD bands have been identified in Au, Hg, Tl, Pb with A ≈ 190 [Henry91, Pilotte94, Schuck97, Singh96, Wilson03, Wilson05]. Quite a few theoretical calculations [Chasman89, Satula91, Krieger92] predict well-defined secondary SD minima persisting in the bismuth and polonium nuclei. Experimentally, this has been confirmed by observations of SD bands reported in [Clark95, Clark96, Herzan15, McNabb96, Nyman15]. The SD bands in the proximity of the A = 190 have in common characteristics which include (1) a γ-ray energy spacing which results in an upsloping dynamic moment of inertia with respect to the rotational frequency, and (2) an intensity pattern that suggests SD bands are populated over several of the highest-spin states and are sharply depopulated over 1-3 of the lowest energy states. The population is thought to occur in the high-spin region at which the SD band becomes yrast [Schiffer90, Lauritsen92]. In the present study, one SD band is observed in ^{193}Bi. The similarities between the SD band observed in this work and those seen in ^{191}Bi [Nyman15] are emphasized. An interpretation in terms of a specific proton excitation is presented.

This thesis is a detailed spectroscopic study of two neutron-deficient odd-A isotopes ^{193}Bi and ^{195}Bi. The main goal of the thesis is to identify nuclear structures present in both isotopes and compare them with the systematics know to this date. Motivation of the second from the two experiments is a search for shape coexistence in ^{195}Bi, since signs of a strongly-coupled band were reported in [Pai12].
As a result of this work, the onset of collectivity is found to extend up to ^{195}Bi. In previous studies of very neutron-deficient odd-A ^{191,193}Bi isotopes [Nieminen04, Nyman15], several isomeric states have been observed. One of them has the spin and parity of $I^\pi = 13/2^+$, built on the 13/2[606] Nilsson orbital. The $13/2^+$ state posses its isomeric character up to ^{199}Bi, where it is found to be associated with spherical shape. Strongly coupled yrast rotational bands on top of these isomeric states have been observed in ^{191,193}Bi, and are now also identified in ^{195}Bi. Yrast negative parity bands based on the proton 7/2[514] Nilsson orbital are also found to be common for the three ^{191,193,195}Bi isotopes. They are associated with the oblate shape. Regarding the low-lying structures, the $1/2^+$ proton intruder states are known to exist in many neutron-deficient Bi isotopes. However, the knowledge on their feeding structures is very limited. So far, irregular band-like structures upon the $1/2^+$ proton intruder state have only been observed in the ^{191}Bi [Nyman15] and ^{193}Bi [Nieminen04]. In ^{195}Bi the corresponding state is also known, but its long half-life avoids identification of the feeding level structure. Regular band-like structure upon the $1/2^+$ proton intruder state is observed and extended in

^{193}Bi. On the other hand, several high-spin isomeric states were identified in heavier Bi isotopes in the past. However, in some cases their exact excitation energies, together with the spin and parity assignments have remained unknown or tentative due to missing depopulating transitions. As we move to more neutron-deficient Bi isotopes, high-spin states become less populated due to rapid decrease of the fusion-evaporation cross-sections. To this date, ^{193}Bi is the lightest odd-A Bi isotope, in which a high-spin isomeric state has been reported [Nieminen04]. This isomeric state, with measured half-life $T_{1/2}$ = 3 μs, has been tentatively assigned with a spin and parity of $I^{\pi} = (29/2^{-})$. This assignment was made based on systematics in heavier odd-A Bi nuclei [Hubel78]. As for the heavier Bi isotopes the depopulating transition was not observed. The structure of the $(29/2^{-})$ isomer is understood as the coupling of an $h_{9/2}$ proton to the 12^{+} isomer in the semi-magic ^{192}Pb core. In several odd-mass astatine isotopes, isomeric states with a spin and parity of $I^{\pi} = 29/2^{+}$ have been observed [Bergstrom70, Sjoreen76, Davie84, Jakobsson10, Auranen15]. These isomeric states were associated with the $\pi((h_{9/2})^2 i_{13/2})$ configuration. In the present study, new high-spin isomeric states with the same spin and parity are identified in both the ^{193}Bi and ^{195}Bi isotopes. Both the $29/2^{+}$ and $(29/2^{-})$ isomers have been connected firmly to the rest of the level schemes. Altogether, four isomeric states have been observed in ^{193,195}Bi, with half-lives ranging from a hundred nanoseconds up to a few seconds. Surprising similarities between the two odd-A Bi isotopes of the present study are found. Even though the ^{195}Bi isotope was believed to posses very little collectivity in the past, the rotational-like bands are observed to survive to high spins and excitation energies.

The experiments presented in this work were carried out at the Accelerator laboratory at the Department of Physics of the University of Jyväskylä. To produce the nuclei of interest, two different fusion-evaporation reactions were employed. Heavy-ion beams provided by an ECR ion source and accelerated by the K-130 cyclotron were impinging on thin and backed (^{195}Bi part) targets, respectively. The fusion-evaporation residues were after their flight through the gas-filled separator RITU [Leino95, Saren11] detected at the RITU focal plane spectrometer GREAT [Page03]. The emitted radiation was measured by the JUROGAM II [Beausang92, Alvarez93, Duchene99] and the GREAT spectrometer high-purity germanium arrays, respectively.
The present work will start with a brief introduction into theoretical background given in Chapter 2, necessary for the discussion of the features observed in both Bi isotopes. Experimental instruments and data-analysis techniques used during the runs and in the data analyses will be explained in Chapter 3. Chapter 4, divided into two sections, will provide a reader with the original results, which are documented with relevant spectra and level schemes for both ^{193,195}Bi isotopes. Interpretation of the results in terms of multi quasi-particle excitations and comparisons with the known systematics of Bi and At isotopes will be discussed in Chapter 5, followed by conclusions and future prospects at

the end of the thesis.

"The saddest aspect of life right now is that science gathers knowledge faster than society gathers wisdom."
Isaac Asimov

Chapter 2

Theoretical Background

2.1 Nuclear models

The nucleus can be defined as a compact object formed by the individual particles, called nucleons, which are bound together through the generally attractive and short-range nuclear force. The nucleons must unconditionally obey the two rules:

- They are independent - noninteracting particles (in a sense of their motion).
- The effects of the Pauli principle.

The ultimate goal of nuclear structure physics is to describe the motions of these individual nucleons (protons and neutrons) and to deduce the behavior of the nucleus from this basis.

2.1.1 Spherical nuclei

Liquid-drop model

At the beginning, an analogy with the liquid drop is taken into consideration. A focus of the nuclear theory is aimed at the attempt to understand the behavior of the curve of nuclear binding energies B characterized by the variation of B with mass number of the nucleus A. The model is required to posses an

important feature. It has to follow an experimentally observed increasing trend of the B/A energies for nuclei below $A = 60$ (nuclear fusion), and smoothly decreasing B/A values for nuclei above $A = 60$ (nuclear fission). These efforts have been finally summarized in the development of the semi-empirical *liquid-drop model*, which gives the following expression (Weiszäcker formula) for the nuclear binding energy:

$$B = a_v A - a_s A^{2/3} - a_c Z(Z-1)A^{-1/3} - a_{sym}\frac{(A-2Z)^2}{A} + \delta. \qquad (2.1)$$

In this expression, the first three terms govern some of the gross collective features of nuclei. The last of these three (collective) terms corrects the resulting B for the Coulomb repulsion of the protons, considering the nucleus as a uniformly charged sphere. The last two terms in the mathematical expression of the model deal more with individual nucleons. These are the so called *symmetry* term and the *pairing* term δ, that accounts for the tendency of like nucleons to couple pairwise.
In this model, the nucleons move independently and are bound together to form a system similar to a charged liquid drop. The *liquid-drop model* can predict and explain some of the nuclear features and processes, like e.g. nuclear fission. It however fails when it comes to explain more sophisticated observations as enhancing the nuclear stability for heavier systems, represented by the proton and/or neutron *magic numbers* (Z or N = 2, 8, 20, 28, 50, 82, and 126), a phenomenon so essential for nuclear structure studies that it cannot be avoided in any proper model.

Shell model

As mentioned earlier, the *liquid-drop model* is unsuccessful in explaining several experimental observations. One of these is the *separation energy* of protons (S_p) or neutrons (S_n). The only reliable explanation is that the sharp discontinuities in the measured separation energy spectra correspond to the filling of major shells in the nucleus. This theorem is one of the pillars of the *shell model*. The *shell model* is generally recognized as the fundamental nuclear model, and serves as the standard against which others are compared. In the *spherical shell model*, trajectories of noninteracting nucleons are defined by the orbits of a spherically symmetric potential $V(r)$, which is itself produced by all the nucleons. In general, the *shell model* uses the Woods-Saxon nuclear potential of the form

$$V(r) = \frac{-V_0}{1 + e^{\frac{r-R_{ave}}{a}}}, \qquad (2.2)$$

where the parameters R_{ave} and a give, respectively, the mean radius and skin thickness of the nucleus. V_0 is the depth of the potential well, and is usually adjusted to give the proper separation energies.

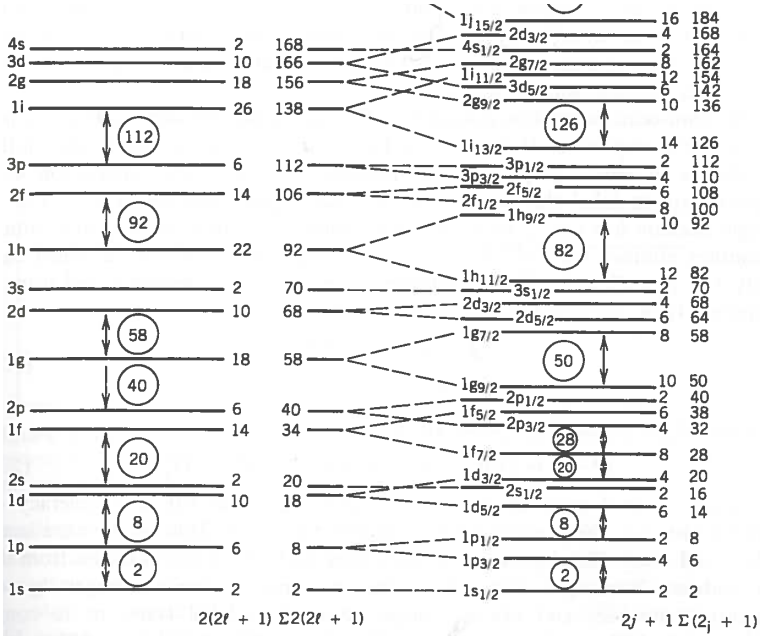

Figure 2.1: On the left-hand side, calculated energy levels based on potential defined by Eq. 2.2 are shown. To the right of each level are its capacity and cumulative number of nucleons up to that level. On the right-hand side, effect of the inclusion of a spin-orbit interaction on the levels with $\ell > 0$ is demonstrated. The proper separation of the subshells as well as reproduction of the magic numbers is apparent. (Reprinted from [Krane88] Fig. 5.6).

The shell model potential still lacks an improvement at this stage. The spherical potential does not allow distinction between magnetic substates (m) of a given orbit, all of which are degenerate. As a result, a wave function of a single-particle in a spherical shell model orbit will as well be spherical, since all m-substates are equally occupied. Following the spectroscopic notation, the orbital labels in Fig. 2.1 can be generally written as $n\ell j$. The quantum number n stays for the number of orbitals with certain ℓ value and can therefore take on only discrete integer values 1, 2, 3 etc. ℓ = s, p, d, ..., is the *orbital angular momentum* (s = 0, p = 1, d = 2, ...) and j denotes the *total angular momentum* of the orbital

$$\boldsymbol{j} = \boldsymbol{\ell} + \boldsymbol{s}, \tag{2.3}$$

where $s = 1/2$ is the *intrinsic angular momentum* or *spin* of the nucleon(s). The total number of nucleons (protons or neutrons) that can occupy the orbital with total angular momentum j is $2j + 1$.

The effort of tuning the nuclear potential is accomplished by adding of a strong

spin-orbit interaction term [Mayer50]

$$\langle \ell \bullet \mathbf{s} \rangle = \frac{1}{2}[j(j+1) - \ell(\ell+1) - s(s+1)]\hbar^2. \tag{2.4}$$

Consequently, thanks to splitting of the j orbitals into $j = \ell + s$, $j = \ell$ - s orbitals, the proper separation of the nuclear shells is observed and correct magic numbers (2, 8, 20, 28, 50, 82, 126) emerge from the calculations.

In the simplest shell model approach, the behavior of the nucleus is determined solely by the motion of the last (valence) unpaired nucleon. Especially in the heavy odd-A nuclei, such as bismuth nuclei of the present study, all the paired nucleons are treated as a one tightly bound core (In this work, ^{192}Pb and ^{194}Pb, respectively.) and the experimentally observed characteristics are described by the core excitation and the coupling of the unpaired particles to the core.

2.1.2 Deformed nuclei

The spherical shell model can explain many features of spherical nuclei, but large discrepancies are observed when it is applied to describe nuclei with many nucleons outside a closed shell. In order to be able to describe the nuclei possessing axially symmetric shapes, the *Deformed shell model* was developed.

Deformed shell model

For non-spherical, deformed nuclei, a preferred axis has to be defined, in order to define their rotation. Assuming a constant nuclear volume of the nucleus, the nuclear radius can be expressed as

$$R(\Theta, \Phi) = R_{ave}\left[1 + \sum_{\lambda=2}^{\infty}\sum_{\mu=-\lambda}^{\lambda} \alpha_{\lambda\mu} Y_{\lambda\mu}(\Theta, \Phi)\right], \tag{2.5}$$

where $\alpha_{\lambda\mu}$ are the coefficients of the spherical harmonics $Y_{\lambda\mu}(\Theta, \Phi)$. The $\lambda = 1$ terms are not considered due to their relation to a translation of the center of mass. The indices λ and μ define the surface coordinates as a function of angles Θ and Φ, respectively. For axially symmetric nuclei, hence independent of Φ, the previous equation reads as

$$R(\Theta, \Phi) = R_{ave}\left[1 + \beta_2 Y_{20}(\Theta, \Phi)\right]. \tag{2.6}$$

The deformation parameter β_2 (originally α_{20}) can be related to the axes of the spheroid as follows

$$\beta_2 = \frac{4}{3}\sqrt{\frac{\pi}{5}}\frac{\Delta R}{R_{ave}}. \tag{2.7}$$

Here, the average radius is

$$R_{ave} = R_0 A^{1/3}, \tag{2.8}$$

and ΔR is the difference between the semi-major and semi-minor axes. The value of parameter β_2 is directly proportional to degree of deformation. Negative and positive β_2 values represent the oblate and prolate shapes of nuclei, respectively. The quadrupole deformation is likely the most common type of deformation in nuclei. It is therefore convenient to express the degree of deformation in term of quadrupole deformation parameter ϵ_2. The basic relation between these two deformation parameters β_2 and ϵ_2 is

$$\beta_2 = \sqrt{\frac{\pi}{5}} \left[\frac{4}{3}\epsilon_2 + \frac{4}{9}\epsilon_2^2 + \frac{4}{27}\epsilon_2^3 ... \right]. \tag{2.9}$$

The deformation parameter can also be used to calculate an electric quadrupole moment Q_0, an indicator of the stable deformation of a nucleus. The relationship between these two parameters is

$$Q_0 = \frac{3}{\sqrt{5\pi}} R_{ave}^2 Z \beta_2 (1 + 0.16\beta_2). \tag{2.10}$$

So far, only axially symmetric deformations have been discussed. Experimentally, also nuclei with axially asymmetric nuclear shapes, called triaxial, were observed. In order to describe the *triaxiality*, an approach called the *Lund convention* [Andersson76] was established. In addition to β_2 quadrupole deformation parameter, it introduces the new parameter γ [Nilsson95] to describe the magnitude of the axial asymmetry of the nucleus. Depending on the axis of rotation, it can take on values -120° $\leq \gamma \leq$ 60°, where few typical values are γ = 60° (single-particle oblate rotation), 0° (prolate symmetric shape) and -60° (collective oblate rotation). The triaxial deformation is described by values of γ that are located in between these predefined values.

Coriolis force

The presence of the last odd particle affects the rotational motion of odd-A nuclei. In the rotating frame, these individual, unpaired particles are subject to the *Coriolis force*. It incorporates the effect of the rotation on the single-particle motion, and becomes relevant in situations, when the rotational frequency becomes comparable with the difference in the frequencies of the particle motion parallel and perpendicular to the symmetry axis. The Coriolis force modifies the single-particle orbits in such a way, that the individual nucleons have a tendency to align their angular momenta in the direction of the axis of rotation. As a direct consequence, the increase in the moment of inertia is observed.

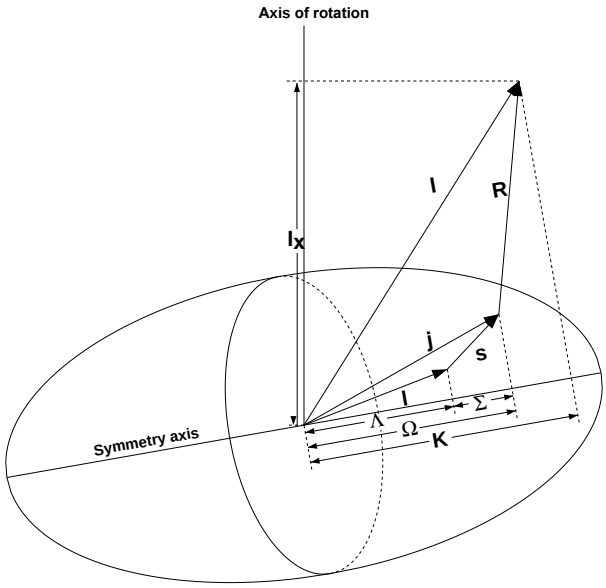

Figure 2.2: Asymptotic quantum numbers for the deformed shell model. The total angular momentum $\boldsymbol{I}$ is composed of contributions from the valence nucleon, $\boldsymbol{j} = \boldsymbol{l} + \boldsymbol{s}$, and the core $\boldsymbol{R}$. In a case of several valence nucleons, a summation is applied.

Nilsson model

Considered as an extension of the deformed shell model, the Nilsson model is a major tool when it comes to description of a new experimental information on single-particle levels in deformed nuclei. In the essentially single-particle model, a filling of orbits is based on their m values instead of their j values. The total angular momentum j used in the spherical shell model is not a good quantum number here anymore. Instead, a set of four Nilsson quantum numbers is introduced in order to define and describe the *Nilsson diagram*. Each Nilsson orbit is labeled by its unique set of $\Omega^{\pi}[Nn_z\Lambda]$ quantum numbers. These are geometrically explained in Fig. 2.2. Ω^{π} gives the projection of the total angular momentum on the symmetry axis of the deformed nucleus. In Nilsson diagram shown in Fig. 2.3, the three parameters inside the brackets are, in their order, N, the principal quantum number denoting the major shell; n_z, which tells the number of nodes in the wave function in the z direction (symmetry axis), and Λ indicates the component of orbital angular momentum L along symmetry axis. The following relation naturally shows up, $\Omega = \Lambda + \Sigma = \Lambda \pm 1/2$, where Σ is the projection of the intrinsic spin of nucleon (fermions have $1/2\ \hbar$ intrinsic spin) on the symmetry axis.

As a consequence of the *Pauli principle*, the crossing of any two lines in the Nilsson diagram corresponding to the same K value and parity is forbidden.

Cranked shell model

The contribution of the aligned particle(s) (i_x) to the total angular momentum (I_x) is obtained as

$$i_x(\omega) = I_x(\omega) - I_{x,ref}(\omega), \tag{2.11}$$

where the rotational frequency ω and the total projection of angular momentum on the rotational axis I_x are defined as

$$\omega = \frac{E(I+1) - E(I-1)}{I_x(I+1) - I_x(I-1)}, \tag{2.12}$$

$$I_x(I) = \sqrt{(I(I+1))^2 - K^2}. \tag{2.13}$$

$E(I)$ denotes the experimentally observed energy of the nuclear state with total angular momentum I. Based on the reference configuration, the experimental Routhians $e(\omega)$ are evaluated using relation

$$e(\omega) = E(\omega) - E_{ref}(\omega). \tag{2.14}$$

Quasiparticle Routhians and aligned angular momenta of the reference configuration, defined for the even-even nucleus to which the experimentally measured rotational structures are compared [Frauendorf81], can be expressed via the following relations

$$I_{x,ref}(\omega) = \omega[J_0 + J_1\omega^2], \tag{2.15}$$

$$E_{ref}(\omega) = -\frac{J_0}{2}\omega^2 - \frac{J_1}{4}\omega^4 + \frac{\hbar^2}{8J_0}. \tag{2.16}$$

Parameters J_0 and J_1 are so called Harris parameters [Harris65].

2.2 Rotations of axially symmetric deformed nuclei

For the energies of a rotating quantum object, such as deformed even-even nuclei, the following representation applies

$$E_{rot}(I) = \frac{\hbar^2}{2\Im} I(I+1), \tag{2.17}$$

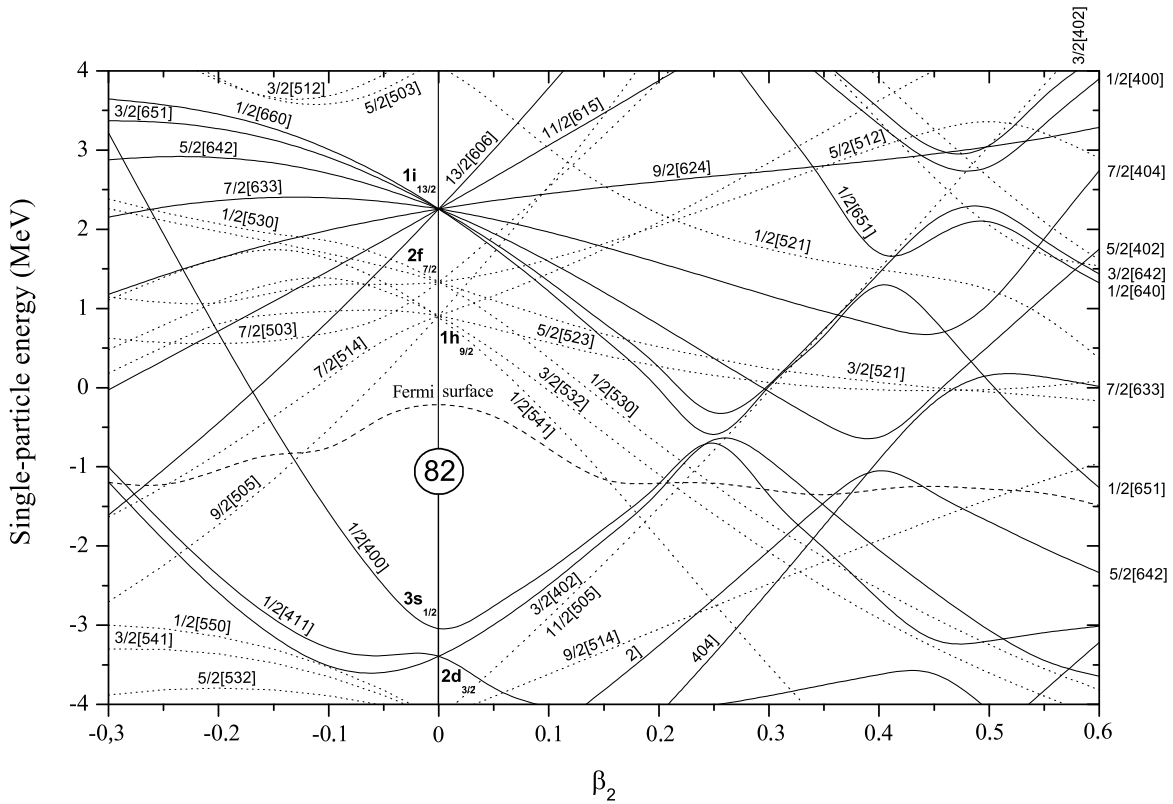

Figure 2.3: A Nilsson diagram for $Z = 83$ protons calculated using a Woods-Saxon potential [Nyman09]. The β_4 deformation parameter was set to zero.

where $\Im$ is the moment of inertia. By increasing the angular momentum I, a contribution to rotational energy of the nucleus is added. As a result, discrete *excited states* are created, hence forming a sequence called *rotational band*. This is possible only in nuclei with nonspherical equilibrium shapes. In ^{193,195}Bi nuclei, an oblate shape has been associated with the observed rotational bands. If we assume an odd-A nucleus (like e.g. those being the subject of this study), the total angular momentum I and its projection on the symmetry axis K of the band-head of the rotational band is solely determined by the valence single particle. The total angular momentum of the corresponding band members can then take on values $I = K,\ K+1,\ K+2$, etc. The rotational energy expression, Eq. 2.17, becomes

$$E_{rot}(I) = \frac{\hbar^2}{2\Im}[I(I+1) - K(K+1)]. \tag{2.18}$$

2.2.1 Spin-dependent moments of inertia

In an analysis of aformentioned rotational energies, the moment of inertia $\Im$ is constant. However, this is not always the case. Effects such as *Coriolis mixing*, discussed earlier, and *centrifugal stretching* make the moment of inertia spin dependent. The *kinematic* $\Im^1$ and *dynamic* $\Im^2$ moments of inertia are used to characterize the evolution of rotational motion. They are defined as

$$\Im^1 = \frac{I_x}{\omega}\hbar \tag{2.19}$$

$$\Im^2 = \frac{dI_x}{d\omega}\hbar, \tag{2.20}$$

where ω and I_x are defined in Eqs. 2.12 and 2.13.

2.2.2 Magnetic moments

The rotational collective motion gives the deformed nucleus a magnetic moment μ. Assuming zero contribution from neutrons, the magnetic moment of a rotational state of angular momentum I, predicted by the collective model, is

$$\mu(I) = I\frac{Z}{A}\mu_N, \tag{2.21}$$

where $\mu_N = 3.1525 \times 10^{-8}$ eV/T is the *nuclear magneton*. It is defined as

$$\mu_N = \frac{e\hbar}{2m_p}, \tag{2.22}$$

where m_p is the proton mass. In fact, both protons and neutrons have the observable magnetic moments μ, mathematically defined in the forms

$$\begin{aligned} \mu &= g_\ell \ell \mu_N \\ \mu &= g_s s \mu_N, \end{aligned} \tag{2.23}$$

where g_ℓ is the *orbital g factor* associated with the orbital angular momentum ℓ, and the quantity g_s is known as the *spin g factor*. Quantitatively, these are

$$\begin{aligned} proton &: g_\ell = 1, g_s = 5.58569 \\ neutron &: g_\ell = 0, g_s = -3.82608. \end{aligned}$$

Finally, the single-particle *g factors* can be calculated using relation

$$g = g_\ell \pm \frac{1}{2\ell + 1}(0.6 g_s - g_\ell), \tag{2.24}$$

where the plus sign refers to $j = \ell + 1/2$ orbital and minus sign to $j = \ell$ - 1/2 orbital, respectively.

2.2.3 B(M1)/B(E2) ratios

To analyze the behavior of the rotational bands, and their intrinsic structure in particular, *B(M1)/B(E2)* ratios are usually extracted from the experimental data. The formula, which compares the transition probabilities of the competing $M1$ and $E2$ transitions is

$$\frac{B(M1)}{B(E2)} = 0.697 \frac{E_\gamma^5(E2) I_\gamma(M1)}{E_\gamma^3(M1) I_\gamma(E2)(1+\delta^2)}, \tag{2.25}$$

where δ denotes the mixing ratio of ΔI = 1 transitions.

For the quasiparticles considered, theoretical estimates for the B($M1$)/B($E2$) ratios are calculated using the semi-classical formalism of Dönau and Frauendorf [Frauendorf81, Donau87], given by the following explicit expression

$$\begin{aligned} \frac{B(M1)}{B(E2)} = \frac{12}{5 Q_0^2 cos^2(\gamma + 30^\circ)} \left(1 - \frac{K^2}{(I-1/2)^2}\right)^{-2} \\ \times \left\{ \left(1 - \frac{K^2}{I^2}\right)^{1/2} \left[\Omega_p (g_a - g_k) \left(1 \pm \frac{\Delta e'}{\hbar\omega}\right)^2 + \sum_n \Omega_n (g_n - g_k) \right] \right. \\ \left. - \frac{K}{I} \left[(g_a - g_k) i_a + \sum_n (g_n - g_k) i_B \right] \right\}^2 . \end{aligned} \tag{2.26}$$

The expression assumes one proton and n neutrons, where subscript a denotes the proton. Parameter Q_0 is defined by Eq. 2.10, K, Ω and γ deformation parameter are discussed in sec. 2.1.2, g denotes the *g factors* defined by Eq. 2.24.

2.3 Radioactive Decay

Radioactive decay is statistical in nature and represents changes in the individual atoms. It is governed by the exponential law. Assuming an isolated system, where N radioactive nuclei are present in the whole sample at time T, then the number of nuclei dN, which have decayed in time interval dT is proportional to total number of nuclei N

$$dN = \lambda N dT \tag{2.27}$$

where λ is the so-called decay constant. By integrating the Equation over observation time T we get the exponential law of radioactive decay in a form

$$N(T) = N_0 e^{-\lambda T} \tag{2.28}$$

where N_0 is the number of nuclei at zero time.

The inverse of the decay constant is the mean lifetime

$$\tau = \frac{1}{\lambda} \tag{2.29}$$

The half-life $T_{1/2}$ determines the time interval needed for the half of the nuclei to decay, and can be expressed in a form

$$T_{1/2} = \tau \; ln2 \tag{2.30}$$

or

$$T_{1/2} = \frac{ln2}{\lambda} \tag{2.31}$$

2.3.1 Alpha decay

Alpha decay becomes increasingly important for heavy nuclei because of the Coulomb force (Z^2 dependence). The alpha particle consists of two protons and two neutrons, thus forming a system known as ${}^4_2\mathrm{He}^{2+}$ nucleus. The spontaneous emission of an α particle is formally represented by the following process:

$${}^A_Z X_N \rightarrow {}^{A-4}_{Z-2} Y_{N-2} + \alpha \tag{2.32}$$

The first theory covering the α particle emission process was developed in 1928 by Gamow [Gamow28] and by Gurney and Condon [Gurney28]. The theory

describes an α decay as a quantum tunneling of an α particle through potential wall. The probability to penetrate the complete barrier is

$$P = e^{-2G} \tag{2.33}$$

where G is the *Gamow factor*, which can be expressed as

$$G = \sqrt{\frac{2m}{\hbar^2}} \int_a^b [V(r) - Q]^{1/2} dr \tag{2.34}$$

The decay constant of an α-particle emitting isotope can then be given by

$$\lambda = fP \tag{2.35}$$

where f is the frequency with which the α particle "attacks" the barrier. In addition, the α-particle pre-formation probability has to be taken into account in order to achieve as precise estimate of the α-decay half-life as the theory can give.
In a case, when the α particle carries out a non-zero orbital angular momentum ℓ, a potential well is approximated as follows

$$V^{eff}(r) = \frac{2(Z-2)e^2}{4\pi\epsilon_0 r} + \frac{\ell(\ell+1)\hbar^2}{2mr^2}, \tag{2.36}$$

where the second term is the so-called *centrifugal potential*. Incorporation of this term to the total potential definition describing the potential well explains the longer half-lives for non-equal spins α decays.

2.3.2 Gamma-ray emission

If the excitation energy of the nucleus avoids further evaporation of baryons or α particles, the nucleus can get rid of its energy excess by electromagnetic (EM) radiation. This can happen via emission of energy quanta called γ rays. The energies of γ-ray transitions can vary significantly. There is, however, a strong spin and parity dependence, allowing only certain type of γ-ray transitions. The selection rule, which dictates the allowed multipoles L, and hence the electromagnetic characters σ are:

$$\left|I_i - I_f\right| \leq L \leq I_i + I_f, \tag{2.37}$$

$$\begin{aligned} electric &: \pi_i \pi_f = (-1)^L \\ magnetic &: \pi_i \pi_f = (-1)^{L+1}. \end{aligned} \tag{2.38}$$

From the experimental point of view, the $L = 1$ *dipole* and $L = 2$ *quadrupole* are the most frequently occurring multipoles of the γ-ray transitions. In Table 2.1, Weisskopf single-particle estimates [Weisskopf51] for transition probabilities λ_W together with the reduced transition probabilities B_W are listed for $L \leq 2$ γ-ray transitions.

Table 2.1: In the 2^{-nd} column are listed the transition probabilities λ; the reduced transition probabilities $B(EL)$ are to be given in $e^2\mathrm{fm}^{2\lambda}$, $B(ML)$ in $(\mu_N/c)^2\mathrm{fm}^{2\lambda-2}$ units. Weisskopf single-particle estimates [Weisskopf51] for reduced transition probabilities B_W and transition probabilities λ_W for first few multipoles L of electric and magnetic transitions are in the 3^{-rd} and 4^{-th} columns, respectively. Greek symbol σ distinguishes between electric (E) and magnetic (M) character of the transitions. The transitions energies E are to be given in MeV.

σL	$\lambda(\sigma\mathrm{L})$ (s^{-1})	$B_W(\sigma\mathrm{L})$ ($e^2\mathrm{fm}^{2\lambda}$)	$\lambda_W(\sigma\mathrm{L})$ (s^{-1})
$E1$	$1.587 \times 10^{15}\mathrm{E}^3\mathrm{B(E1)}$	$6.446 \times 10^{-2}A^{2/3}$	$1.023 \times 10^{14}E^3A^{2/3}$
$M1$	$1.779 \times 10^{13}\mathrm{E}^3\mathrm{B(M1)}$	1.790	$3.184 \times 10^{13}E^3$
$E2$	$1.223 \times 10^{9}\mathrm{E}^5\mathrm{B(E2)}$	$5.940 \times 10^{-2}A^{4/3}$	$7.265 \times 10^{7}E^5A^{4/3}$
$M2$	$1.371 \times 10^{7}\mathrm{E}^5\mathrm{B(M2)}$	$1.650\mathrm{A}^{2/3}$	$2.262 \times 10^{7}E^5A^{2/3}$

2.3.3 Conversion-electron spectroscopy

Internal conversion is the competing process to the γ-ray emission. The lower the transition energy, the higher is the probability for the specific γ ray to interact with the electron cloud of the nucleus, resulting in ejecting an atomic electron. The energy of the electron is then given by the difference of the initial γ-ray energy and of the binding energy of emitted electron. This rule can be written as

$$E_e = E_\gamma - E_B, \tag{2.39}$$

where E_e is the actual kinetic energy of the emitted conversion electron, E_γ is the γ-ray energy and E_B is the binding energy of the emitted conversion electron, which is determined by the electron-shell from which the electron is emitted. This process is also characterized by emission of specific X-rays, as a consequence of filling the holes in the electron cloud created in the electron conversion process by electron transitions from higher electron shells. The energy of such an X-ray is then solely determined by the energy difference of corresponding electron shells (K, L, M ...).
For specific EM transition, the ratio between the internal conversion probability λ_e and the γ-ray transition probability λ_γ is expressed via *internal conversion coefficient* α:

$$\alpha = \frac{\lambda_e}{\lambda_\gamma}. \tag{2.40}$$

In contrast to γ-ray transitions, internal conversion process is favored by low level energy differences and higher orbital angular momenta ℓ the rotating nuclei loose in the de-excitation process.
Due to strong competition between the internal conversion and γ-ray emission, especially for low-energy $L = 1$, 2 transitions, it is sometimes more convenient

to give the total transition probability λ_{tot}, which is the sum of the two just described probabilities, hence

$$\lambda_{tot} = \lambda_\gamma + \lambda_e. \tag{2.41}$$

Chapter 3

Experimental Techniques

3.1 The fusion-evaporation reaction

Considering stable beam-target combinations, fusion-evaporation reactions, often referred to as heavy ion reactions, can bring in a huge amount of energy and angular momentum and access unstable, neutron-deficient nuclei. The heavier the compound nucleus, the stronger the competition between the fusion-evaporation and fission processes. Nevertheless, the fusion-evaporation reactions allow for studying the high-spin states of nuclei one cannot reach by any other type of nuclear reactions. The target is bombarded by heavy-ion beam with an energy sufficient to overcome the Coulomb barrier that exists between itself and the target nucleus. Assuming spherical nuclei, the Coulomb barrier V_C in MeV units is approximately given by the equation

$$V_C \approx \frac{Z_p Z_T}{A_p^{1/3} + A_T^{1/3}}, \tag{3.1}$$

where the subscripts p and T refer to the projectile (heavy-ion beam particle) and target nucleus, respectively.
In most cases, the compound nucleus is highly excited and almost instantly undergoes particle (proton, neutron etc.) evaporation, depending on the excitation energy of the fusion product. Such compound nucleus, even though still oriented to a certain direction, remains in rotational motion until it reaches its ground state via characteristic γ-ray and electron emission. This happens, when the difference between the excitation energy of the nucleus and the yrast line is insufficient to evaporate any more neutrons or charged particles.

3.2 Instrumentation

3.2.1 The JUROGAM II array

JUROGAM II is a spectroscopic array consisting of 39 high-purity Compton-suppressed germanium (HPGe) detectors. It is divided into four separated rings, all positioned at different angles θ relative to the beam direction. There are altogether 15 Eurogam Phase1[Beausang92] and/or GASP type [Alvarez93] detectors (Rings 1 and 2) and 24 composite clover type [Duchene99] HPGe detectors (Rings 3 and 4). It is mounted in a sphere-like arrangement around the target chamber to measure the prompt γ rays. These detectors are instrumented with Lyrtech VHS-ADC cards, which allows direct digitization of the preamplifier signals. The energies of detected γ rays are determined using a moving window deconvolution (MWD) algorithm [Georgiev93] implemented in the field-programmable gate-array (FPGA) of the analog-to-digital converters (ADC) cards.
Since the evaporation residue (further recoil, Re) is after its creation flying at a velocity of a few per cent of the speed of light, the measured γ-ray energies E'_γ must be afterwards corrected for Doppler effect in order to get the correct energies of the emitted γ-ray transitions E_γ. The correction is made using formula

$$E'_\gamma = E_\gamma(1 + \beta cos\theta) \tag{3.2}$$

where $\beta = \frac{v}{c}$, v is the recoil velocity and θ is the angle of the centre of the HPGe detector relative to the beam propagation.
The energy calibration of JUROGAM II array is done using the standard mixed ^{133}Ba-^{152}Eu radioactive source and *ENCAL* program from the RadWare software package [Radford95a, Radford95b]. In the data analysis, to make the correction of the measured γ-ray intensities for the detection efficiency of the JUROGAM II array, program called *EFFIT* [Radford95a, Radford95b] is applied on the same set of calibration data. Equation 3.3 is the mathematical expression of the fitting function used for the efficiency ϵ calibration in this study

$$\epsilon(E_\gamma) = exp\left\{\left[\left(A + B \times X + C \times X^2\right)^{-G} + \left(D + E \times Y^2\right)^{-G}\right]^{(-1/G)}\right\}, \tag{3.3}$$

where $X = ln(E_\gamma/E1)$ and $Y = ln(E_\gamma/E2)$. Values of 100 keV and 1 MeV are used for the constants $E1$ and $E2$, respectively. In the case of JR107 experiment (^{195}Bi data), the following coefficients fit best the measured JUROGAM II efficiency: $A = 6.195$, $B = 1.79$, $C = 0$, $D = 5.49$, $E =$ -0.635, $F = 0.032$ and $G = 20$. The total photopeak efficiency of the fully-digitized JUROGAM II array using the add-back technique is 5.2 % at 1.3 MeV.

Angular distribution

Analysis of angular distributions $W(\theta)$ determine the multipole order of EM radiation. The angular-distribution function for a transition connecting two nuclear states is usually expressed as [Newton67]

$$W(\theta) = 1 + A_2 P_2(cos\theta) + A_4 P_4(cos\theta). \tag{3.4}$$

Determination of parameters A_2 and A_4 yields information on the multipolarities and multipole mixing of the transitions involved, and hence on the spins and parities of the corresponding states. $P_2(cos\theta)$ and $P_4(cos\theta)$ are the second and fourth order Legendre polynomials, respectively. In fact, parameter A_4 representing the multipole mixing is set to zero in the present study due to limitations in the current experimental set-up and the statistics. The first oder estimate of the transition multipole is obtained by fitting the $W(\theta)$ function

$$W(\theta) = A_0[1 + A_2 P_2(cos\theta)] \tag{3.5}$$

to the γ-ray intensity vs $cos^2\theta$ plot. The parameter A_0 reflects the amount of data. Positive value of parameter A_2 indicates a stretched quadrupole and negative value a stretched dipole character of the transition, respectively.

Directional correlations

An approach known as **D**irectional **C**orrelations from **O**riented states (DCO) is used, when there is an interest in determining the nature (dipole and/or quadrupole) of the γ-ray transitions. In the studies of weak transitions, large arrays of detectors are commonly used. The directional correlation from any oriented state in nucleus of interest is given by

$$R_{DCO} = \frac{J(\theta_1, \theta_2, \Psi)}{J(\theta_2, \theta_1, \Psi)}. \tag{3.6}$$

Here, $J(\theta_1, \theta_2, \Psi)$ is the intensity of γ_1 γ-ray transition detected by detectors at angle θ_1 in coincidence with γ-ray transition γ_2 detected by detectors at angle θ_2. Consequently, $J(\theta_2, \theta_1, \Psi)$ is the intensity of γ-ray transition γ_1 detected by detectors at angle θ_2 in coincidence with γ_2 γ-ray transition detected by detectors at angle θ_1, while Ψ is the angle between the detectors.
The corresponding experimental R_{exp} ratio is defined by expression

$$R_{exp} = \frac{I_{\theta_1}^{\gamma_2}\left(gate_{\theta_2}^{\gamma_1}\right)}{I_{\theta_2}^{\gamma_2}\left(gate_{\theta_1}^{\gamma_1}\right)}, \tag{3.7}$$

where I_θ^γ is the experimentally measured γ-ray intensity, corrected for the detection efficiency of detectors at an angle θ relative to the beam direction.

In this study, the experimental values of angular distribution ratios (R_{exp}) were extracted from two γ-γ matrices, which were formed by sorting recoil-gated prompt coincidence events with (157.6°) vs. (all angles) and (75.5°) vs. (all angles) combinations. By setting the same energy gates on the (all angles) projection spectrum in both matrices, two coincidence spectra were made representing the aformentioned detection angles. The intensity of the γ rays of interest was extracted from these spectra and normalized for the detection efficiency ϵ. The R_{exp} ratios are calculated using the formula

$$R_{exp} = \frac{I_\gamma(157.6°)}{I_\gamma(75.5°)}. \tag{3.8}$$

In this study, the typical values for stretched dipole and quadrupole transitions are 0.8 and 1.3, respectively.

Linear polarization

In general, IPDCO (Integrated Polarizational-Directional Correlation from Oriented nuclei [Starosta99]) measurements combined with DCO analysis provide an essential information on the electromagnetic and multipole character of the transition, and hence on the spins and parities of the states the transition connects. The Compton linear polarimeter usually consists of at least two γ-ray detectors: a scatterer and an analyzer. The primary γ radiation from the target passes through the scatterer and is scattered in the direction specified by the Compton scattering angle into the analyzer positioned at an angle Φ. The electric vector of primary radiation is decomposed into two orthogonal vectors, one corresponding to the radiation for $\gamma = 0°$ and the other for $\gamma = 90°$.
In the present work, the JUROGAM II array is also used as a polarimeter device. In fact, one clover germanium detector can act as a polarimeter on its own, since only three crystals are needed. One crystal acting as a scatterer and the two remaining crystals as absorbers for vertically and horizontally scattered γ-ray transitions. In our setup, all 24 clovers placed in JUROGAM II at two different angles (rings) relative to the beam direction were used.
This kind of Compton polarimeter offers the following advantages:

- The segmented polarimeter (Clovers) has a high coincidence efficiency ϵ_{coinc}, due to the tight geometry and the large solid angles.
- The large volume of the crystals results in a high total detection efficiency ϵ_{tot}.
- The segmented polarimeter offers a nearly full symmetry. The apparative asymmetry is a very small ($a \approx 1$).
- The polarimeter is rather compact and can be easily shielded by active shieldings like an BGO-anti-Compton shield.

The quality of polarimeter can be evaluated by determining the polarization sensitivity Q. In other words, Q is a measure of the sensitivity of a system of finite detectors to linear polarization. The polarization sensitivity Q is defined via relation

$$A_P = PQ, \tag{3.9}$$

where A_P is the polarization asymmetry and P is linear polarization. P can be theoretically calculated using formula

$$P(\theta) = \frac{J(\Psi = 0°, \theta) - J(\Psi = 90°, \theta)}{J(\Psi = 0°, \theta) + J(\Psi = 90°, \theta)}, \tag{3.10}$$

where $J(\Psi = 0°, \theta)$ and $J(\Psi = 90°, \theta)$ are the intensities of the γ radiation with its electric vector lying in a plane at an angle Ψ to the plane containing θ. Experimentally, it can be obtained from precisely measured angular distributions $W(\theta)$ of the representative electromagnetic radiation. Considering pure dipole γ-ray transitions, the linear polarization P as a function of the angle of the detectors θ can be expressed as

$$P(\theta)^{M1,E1} = \pm\frac{3A_2 sin^2\theta}{2 - A_2 + 3A_2 cos^2\theta}, \tag{3.11}$$

The equation has a positive sign for $M1$ transitions and a negative sign for $E1$ transitions, respectively. Similarly, for pure quadrupole transitions, the equation for $P(\theta)$ can then be rewritten in the form [Lee02]

$$P(\theta)^{E2,M2} = \pm\frac{3A_2 sin^2\theta + A_4\left(\frac{35}{4}cos^4\theta - 10cos^2\theta + \frac{5}{4}\right)}{2 - A_2 + 3A_2 cos^2\theta + A_4\left(\frac{35}{4}cos^4\theta - \frac{30}{4}cos^2\theta + \frac{3}{4}\right)}, \tag{3.12}$$

where a negative sign corresponds to magnetic radiation and a positive sign to electric radiation, respectively. A_2 and A_4 are coefficients of Legendre polynomials, obtained by fitting the angular distributions $W(\theta)$ of the corresponding γ rays. In the present study, only values of A_2 coefficients can be achieved by fitting the experimental data points. Values of A_4 coefficients are calculated based on information in [Yamazaki67]. The maximum linear polarization P will be observed at $\theta = 90°$. Hence, the equations for $P(90°)$ immediately transform to

$$P(90°)^{M1,E1} = \pm\frac{3A_2}{2 - A_2}, \tag{3.13}$$

$$P(90°)^{E2,M2} = \pm\frac{12A_2 + 5A_4}{8 - 4A_2 + 3A_4}. \tag{3.14}$$

The signs of linear polarization for different types of electromagnetic radiation are summarized in Tab 2.1. In order to obtain the information on the linear polarization asymmetries A_P, two γ-γ matrices were created as follows: The first γ ray corresponds to a single-crystal hit in any detector of the array and the second one to the sum of the energy deposited in two crystals within the same

Table 3.1: The signs of the Legendre polynomials coefficients A_2, A_4 and resulting linear polarization $P(\theta)$ for γ-ray transitions of different character.

Transition character	A_2	A_4	$P(\theta)$
Stretched $M1$	-	0	-
Stretched $E1$	-	0	+
Stretched $M2$	+	-	-
Stretched $E2$	+	-	+

clover detector located at 75.5° or 104.5° relative to the beam axis, respectively. With such a procedure, the matrices contain events with either horizontally or vertically scattered γ rays in a clover (at the angles mentioned above) on one axis and a single-crystal hit on any of the detector on the other axis. The experimental polarization asymmetry is defined as

$$A_P = \frac{[a(E_\gamma)N_\perp] - N_\parallel}{[a(E_\gamma)N_\perp] + N_\parallel}, \tag{3.15}$$

where $a(E_\gamma)$ is the normalization factor corresponding to the asymmetry of the JUROGAM II array and is defined as

$$a(E_\gamma) = \frac{N_\parallel(unpolarized)}{N_\perp(unpolarized)}. \tag{3.16}$$

The normalization factor is a function of γ-ray energy and has been obtained from the measurement with a standard ^{152}Eu radioactive source. Figure 3.1 shows the variation of a with an energy E_γ. As one can see, the value of a is very close to unity and varies only minimally with the energy, therefore telling that the clovers' symmetry was nearly ideal. The number of horizontally ($N_\perp$) and vertically ($N_\parallel$) scattered events for a given γ ray was obtained by setting gates on coincident single-crystal hit γ-ray transitions in the two asymmetric matrices. Based on the experimental results obtained in this work (^{193}Bi part) using the JUROGAM II array, pure magnetic transitions have a value of A_P $\sim$ -0.1 and those of pure electric transitions of $\sim$ 0.1. Measured polarization sensitivity Q plotted against the energy of stretched M1 and E2 transitions is presented in Fig. 3.2. Experimentally measured values of A_2, A_P, P and Q are summarized in Table 3.2.

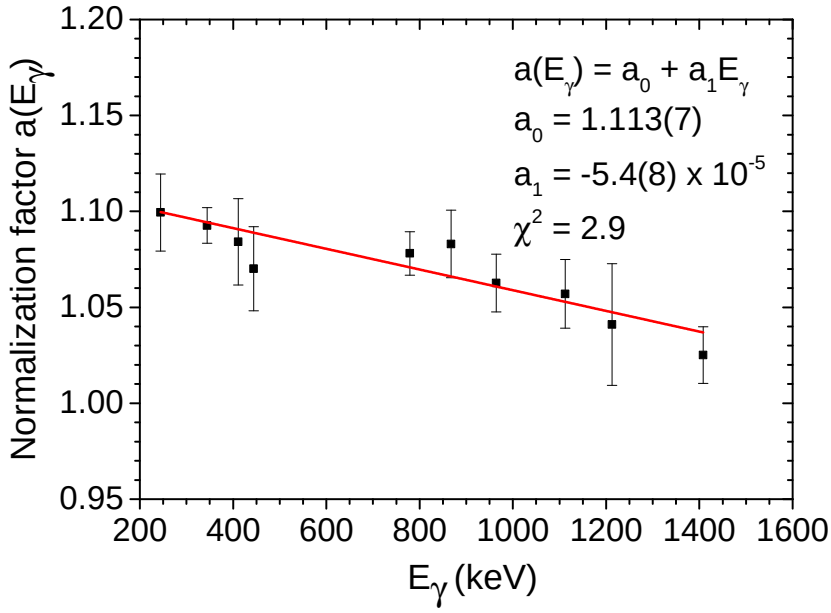

Figure 3.1: (Color online) Normalization factor a in the linear polarization measurements as a function of γ-ray energy (E_γ) for the JUROGAM II array.

Table 3.2: Energies E_γ, initial and final spins I_i^π and I_f^π, respectively, for the γ-ray transitions used in linear polarization measurement. Also A_2 coefficients of Legendre polynomials from the fitting of angular distributions $W(\theta)$, linear polarization asymmetries A_P , linear polarization factors P and polarization sensitivities Q are shown.

E_γ (keV)	I_i^π	I_f^π	A_2	A_P	P	Q
203.9(1)	$35/2^+$	$33/2^+$	-0.2733(487)	-0.130(9)	-0.346(62)	0.376(72)
550.0(1)	$15/2^-$	$11/2^-$	0.2029(690)	0.06(2)	0.282(96)	0.213(101)
626.2(1)	$19/2^+$	$15/2^+$	0.3690(1142)	0.094(9)	0.587(182)	0.160(52)
646.9(1)	$21/2^+$	$17/2^+$	0.3478(787)	0.091(4)	0.547(124)	0.166(38)
665.2(1)	$23/2^+$	$19/2^+$	0.2918(438)	0.072(7)	0.443(67)	0.163(29)
668.9(1)	$23/2^-$	$19/2^-$	0.3806(590)	0.103(11)	0.612(95)	0.168(32)
817.9(1)	$13/2^-$	$9/2^-$	0.1551(591)	0.039(3)	0.200(76)	0.195(76)
908.7(1)	$17/2^+$	$13/2^+$	0.2276(1275)	0.056(12)	0.326(182)	0.172(103)
954.7(1)	$33/2^+$	$29/2^+$	0.3155(1076)	0.060(3)	0.489(167)	0.123(42)

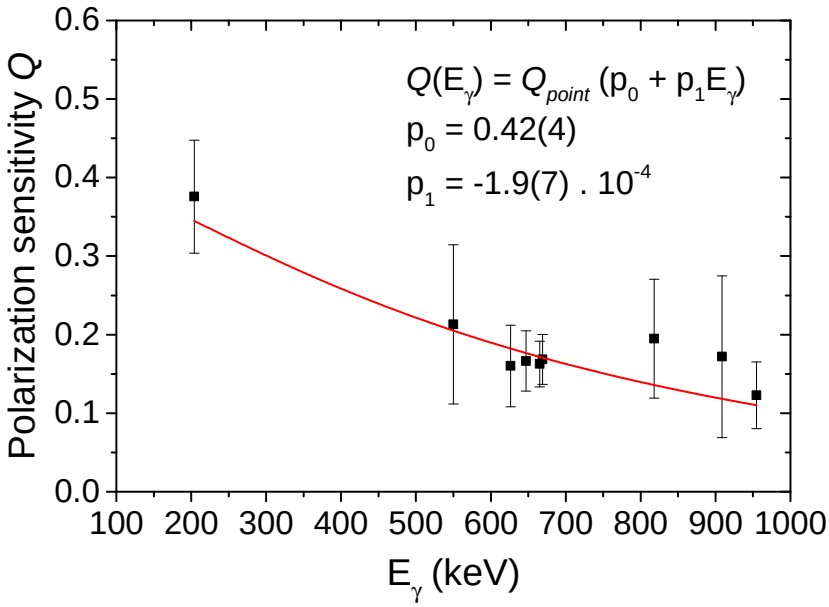

Figure 3.2: Polarization sensitivity of the JUROGAM II array as a function of γ-ray energy.

3.2.2 The RITU gas-filled separator

To clean the fusion-evaporation residues recoiling out from the target from the unwanted particles (in the present study mostly fission fragments and binary products from quasi-elastic reactions), the gas-filled recoil separator RITU (Recoil Ion Transport Unit) [Leino95, Saren11] positioned right behind the JUROGAM II array is used (see Fig. 3.2). The inner volume of the RITU separator is filled with a diluted gaseous helium to enhance the recoil transmission based on the charge equalization principle. In case of the RITU separator, the optical geometry is QDQQ. The usage of the first quadrupole (Q) magnet improves the focusing of the fusion-evaporation products recoiling out of the target chamber to the dipole magnet. As will be shown later, focusing of the fusion-evaporation products of interest by the RITU separator to its focal plane detector setup allows to employ several powerful data analysis techniques. The gas-filled RITU separator does not have the mass-resolving power of the separators working in the vacuum mode. However, this disadvantage against the vacuum-mode mass separators is out-weighted by higher transmission of RITU. In the case of asymmetric reactions, like those of the present study, the RITU transmission to the MWPC is about 40 %. This yields the overall fusion-evaporation products detection efficiency in the DSSD of $\sim$ 25(5) % [Saren11].

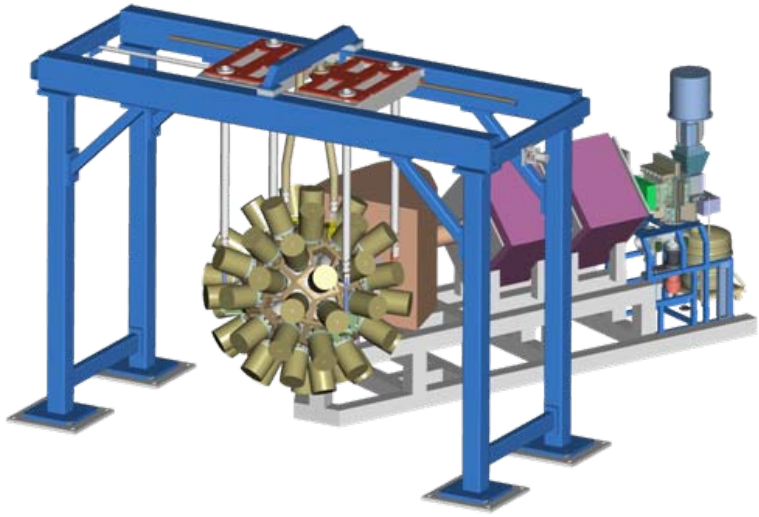

Figure 3.3: (Color online) The experimental setup used in the present study.

3.2.3 The GREAT focal plane spectrometer

The GREAT (Gamma Recoil Electron Alpha Tagging) spectrometer [Page03] measures the decay properties of reaction products transported to the focal plane of the RITU separator. In the present study, GREAT comprises a system of multi-wire proportional counter (MWPC), double-sided silicon strip detectors (DSSDs), and germanium detectors. The setup is optimized for detecting the arrival of the fusion-evaporation reaction products (further recoils) and correlating with subsequent radioactive decay involving the emission of α particles, γ rays, X-rays or conversion electrons.

Multi-wire proportional counter
In order to distinguish between recoiling reaction products and their subsequent decays, the MWPC is mounted right behind RITU as an entrance window of GREAT. The detector is filled with the circulating isobutane gas, so that a specific energy loss dE can be measured for each particle passing through the MWPC. For this reason the MWPC is sometimes called a gas counter, as it can only count the number of events, but cannot recognize their nature. Two thin Mylar foils keep the gas volume in the detector at constant level and protect it from leaking to other parts of the detector setup. The position sensitivity of the detector is achieved by horizontal and vertical wiring.

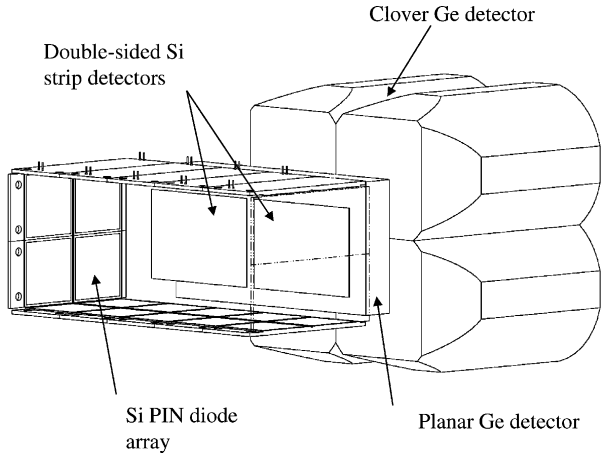

Figure 3.4: Schematic drawing of the GREAT spectrometer. The geometry was different in both experiments. The three Clover Ge detectors were positioned above and on sides of the vacuum chamber. Figure reprinted from [Page03].

Double-sided silicon strip detector

The main instrument of the GREAT spectrometer is a pair of adjacent double-sided silicon strip detectors (DSSDs) - 40 mm $\times$ 60 mm in size with a 1 mm strip pitch. The DSSDs are mounted in the vacuum chamber downstream from the MWPC. Their placement in the GREAT spectrometer is schematically shown in Fig. 3.4. In the present work, the thickness of each detector was 300 μm. The DSSDs were tuned and used for the recoil implantation and for detection of their subsequent α decay in horizontal strips (DSSD-Y side) and internal conversion electrons in vertical strips (DSSD-X side). As the internal conversion takes place inside the DSSDs, the energy deposited by the Auger electrons and low-energy X-rays, as accompanying process of internal conversion, sums up with the energy deposit of the conversion electron. This causes an additional $\sim$ 10 keV contribution to the total energy deposit. To calibrate the DSSDs, a mixed-α source (^{239}Pu, ^{241}Am and ^{244}Cm) was used. Due to the shallow implantation depth of the recoils, the α-particle detection efficiency of the DSSD is approximately 50 %. To improve the energy resolution, the DSSDs are cooled down to a temperature of -25 °C.

PIN diode detector

The probability that a certain portion of the recoil-decay products escape from the DSSDs is rather significant. In order to collect the α particles and conversion electrons, which do not deposit their full energy E in the DSSDs, an array of silicon PIN diode detectors is mounted in a box arrangement upstream from the DSSDs. The array consists of 28 silicon PIN diodes with a thickness of 500

μm. Each PIN diode has an active area of 28 $\times$ 28 mm. In this work, a simulated efficiency curve for PIN diode detectors [Andreyev04] was used, which gives approximately 20 % absolute efficiency for detection of a 300 keV conversion electron. As with the DSSDs, also the PIN diode detectors are cooled down by using the same cooling block.

Germanium detectors
Germanium detectors at the RITU focal plane are generally used to detect the delayed γ rays and X-rays, and hence identify isomeric states, which decay via emission of EM transitions. A planar Ge detector is mounted downstream of the DSSDs in the GREAT chamber and separated by the thin beryllium entrance window, as it operates in vacuum mode. It is designed to detect low-energy γ rays and X-rays. Geometrically, the planar double-sided Ge strip detector is of rectangular shape. The active area of the detector is 120 mm $\times$ 60 mm. Each strip is 5 mm wide and has a thickness of 15 mm. To detect high-energy γ rays, a set of three Clover detectors is added and placed to face the GREAT chamber from sides and from above.

3.3 Data analysis methods

In the experiments of the present study, all data channels are recorded synchronously using the triggerless total data readout (TDR) [Lazarus01] data acquisition system. Additionally to an energy stamp, all the events are time-stamped using a 100 MHz clock. The reaction products have been studied using in-beam γ-ray spectroscopy combined with decay spectroscopy. The data have been analyzed using the recoil-gating, recoil-decay tagging (RDT) [Schmidt86] and isomer-tagging techniques [Scholey01] and processed using the GRAIN [Rahkila08] and RADWARE [Radford95a, Radford95b] software packages.

3.3.1 In-beam gamma-ray spectroscopy with JUROGAM II array

In the fusion-evaporation reactions, the nuclei of interest are very often populated up to very high spin I. To extract the information on the γ-ray transitions depopulating the high-I levels, and hence to determine the level energies, employing of the prompt γ-ray spectroscopy is essential. In the present study, the JUROGAM II array measures the prompt γ rays. Thanks to in-beam JUROGAM II data not only the high-I levels can be identified, but moreover, the level structures feeding the isomeric states can be constructed.
In the experiments of the present work, the so-called recoil-gating technique is

used in order to clean the JUROGAM II data. The fusion-evaporation residues, often called recoils, are identified based on the combined information from the MWPC and the DSSD. Before the implantation in the DSSD, the flying recoil passes through the MWPC, where a characteristic energy loss dE is deposited. The signal from the MWPC also serves as the starting point of the *time-of-flight* (ToF) of the recoil event. Once implanted in the DSSD, the total energy loss E, together with the stop signal for ToF of the recoil event is recorded and available for further on-line/off-line analysis. If the event passes the 2-dimensional $TOF - dE$ gate, it is accepted and used for γ-ray selection.
To demonstrate the advantage of the recoil-gating technique on the prompt γ-rays measurement with JUROGAM II array, Fig. 3.5 is presented. Panel (a) corresponds to JUROGAM II data collected when triggering on the 4-fold γ-ray events in the backed target (Au-backing) experiment. In this high-fold γ-ray spectrum, transitions of many different reactions' products can be identified (fission products from Kr - Sn). It is worth mentioning that software high-fold γ-ray trigger is required to make ^{195}Bi γ rays more visible. This requirement removes many γ rays related to fission and quasi-elastic reactions. For the clarity of the figure, only the strongest transitions are labeled.
An energy spectrum shown in panel (b) of Fig. 3.5 contains only those γ-ray transitions measured in JUROGAM II, which are in the prompt coincidence with the recoils identified by the method described above. The background level is especially lower in the higher-energy part of the recoil-gated spectrum. The γ-ray transitions belonging to bismuth are clearly dominating the spectrum, and even γ-ray transitions from the Coulomb excitation of the Tb target vanish, when coincidences with the recoil events are demanded.

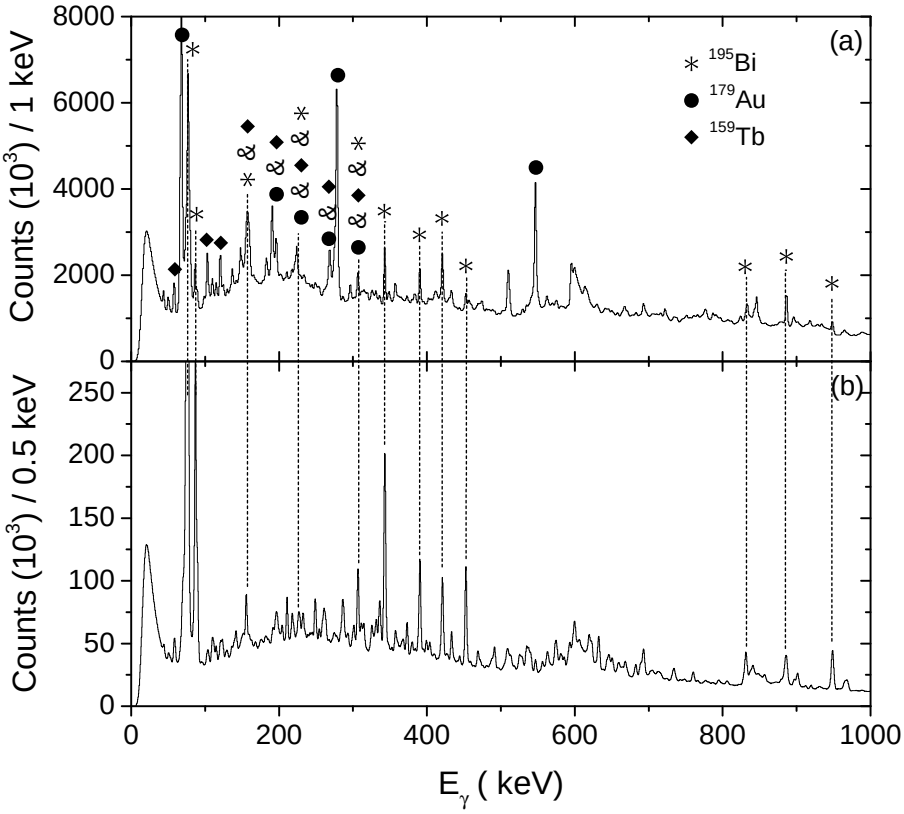

Figure 3.5: A total γ-ray energy spectrum measured in JUROGAM II and (a) gated on the γ-γ coincidences with multiplicity 4 required in the backed target experiment; (b) gated with recoils in the thin target experiment, in the reaction ^{40}Ar + ^{159}Tb, E_b = 175 MeV, $I_b \approx$ 3 pnA in (a) and 9 pnA in (b).

3.3.2 Recoil-decay tagging

The neutron-deficient nuclei such as bismuth nuclei of the present study often decay by the emission of charged particles. Under certain circumstances, it is possible to do correlations of the recoils with their characteristic decay particles. A technique that performs a selection of the prompt γ rays with respect to the characteristic radioactive decays of the recoil events is called the recoil-decay tagging (RDT) [Simon86, Paul95]. In RDT, the valid recoil event identification is done using the same principles as already explained above. A decay event (e.g. α-particle event) measured in the DSSD is identified and accepted for the correlation procedure if it is in anti-coincidence with a signal

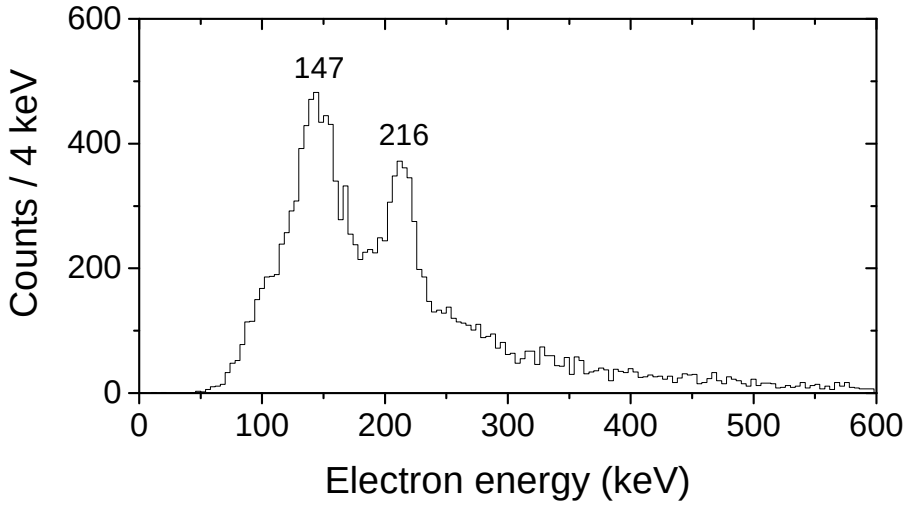

Figure 3.6: An energy spectrum of conversion electrons measured in the DSSD and gated on the 455 keV γ-ray detected in focal plane clover detectors in ^{193}Bi experiment. Since the recoil decay happens inside the DSSD in this case, the corresponding electron peaks are products of summation of all events energies. Peaks include contributions from electrons escaped from $K + L + M + \ldots$ shells. Also, addition of the *Auger* electron energies shift the final position of the electron peaks. Spectrum for decay of the $29/2^+$ isomeric state in ^{193}Bi.

from MWPC and passes an energy gate. The recoils and characteristic decay particles are correlated on the basis of the spatial and temporal information available for both events. It is worth mentioning that to perform a successful RDT analysis, a half-life of the corresponding state should be reasonably shorter when compared to random events' rate, and the branching ratio high enough so that an efficient tagging of γ rays is achieved.

3.3.3 Isomer tagging

Isomer tagging technique was used for the first time in the study done by Cullen *et al.* [Cullen98]. Instead of requiring the correlations between the recoils and charged particles such as α particles or protons, observation of the delayed electromagnetic transition in coincidence with recoils within beforehand specified time-window is necessary. Subsequently, only prompt γ rays gated with the recoils, which fulfill the aformentioned requirement are selected to fill the relevant spectra.

In this work, among other delayed transitions, also conversion electrons de-

tected in the DSSD have been used for isomer tagging. One example spectrum is presented in Fig. 3.6. Only electrons, which pass the energy and time gates, respectively, and gated with the delayed 455 keV γ-ray in ^{193}Bi are put in this energy spectrum. Close inspection of the structure of the spectrum confirms that only electrons from the internal conversion of the low-energy transitions below the isomeric state are present there.
Correlation of the recoils with electrons detected in the DSSD brings an enhanced selectivity. Recoil-electron correlations have extensively been used in the present analysis of the ^{193}Bi data. The analyzing power of both tagging techniques will be demonstrated in the following sections.

Chapter 4

Results

In the present work, detailed spectroscopic studies of two neutron-deficient nuclei ^{193,195}Bi were performed. Using almost a complete set of nuclear spectroscopic tools, an extensive knowledge about these two isotopes has been obtained. Both experiments were carried out at the Accelerator laboratory of the University of Jyväskylä (JYFL). The heavy-ion beams were produced in an ECR ion source and accelerated by the K-130 MeV cyclotron. In case of ^{195}Bi, in addition to the thin target experiment, also a thick target experiment was performed in order to gain information on the level structures fed by the decay of the short-lived isomeric states. In order to detect the prompt γ rays, the fully digitized JUROGAM II array surrounding the target chamber was employed. The unwanted particles were subtracted from the fusion-evaporation residues of interest after their creation by the gas-filled recoil separator RITU, and implanted in the DSSDs of the focal plane spectrometer GREAT for their further analysis. In the case of ^{193}Bi, the subsequent α decays for RDT analysis are measured there.

The measurable quantities in this type of experiments, which directly contribute to building as precise a picture about the nucleus as possible, are the energies and relative intensities of γ-ray transitions (both prompt and delayed), α particles and conversion electrons, the α-decay branches and half-lives of α-decaying and isomeric states.

The spin and parity assignments of the nuclear states are predominantly deduced on the basis of the information obtained from the angular distribution ratios and linear polarization measurements.

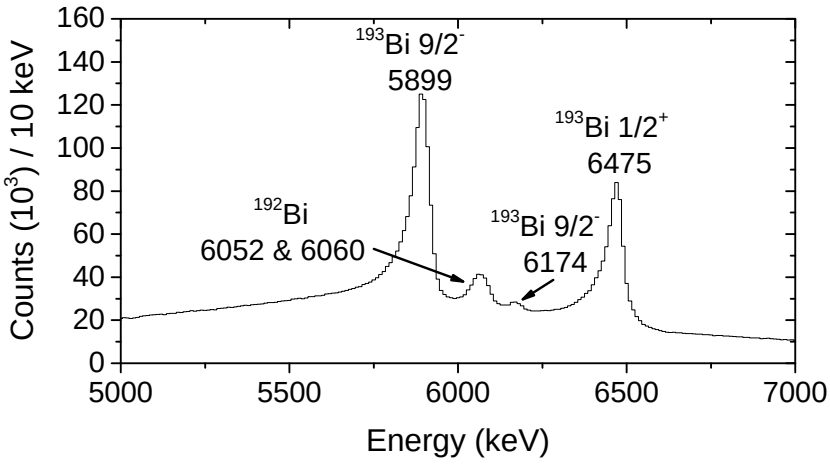

Figure 4.1: Energy spectrum of alpha particles (vetoed by MWPC) from the reactions ^{165}Ho(^{32}S,xn)$^{197-x}$Bi collected in the DSSDs.

4.1 ^{193}Bi

The fusion-evaporation reaction ^{165}Ho(^{32}S,xn)$^{197-x}$Bi was employed in order to study to shape coexistence in the ^{193}Bi nuclei. The self-supporting Ho target was bombarded with stable ^{32}S beams, accelerated by the K-130 cyclotron to an energy 152 MeV. The average beam intensity I_b was 17 particle nA (pnA). The total irradiation time was 130 hours.

The ^{193}Bi nucleus has two alpha-decaying states: The $9/2^-$ ground state (E_α = 5899(5) keV, I_α = 95.8 % and E_α = 6174(5) keV, I_α = 4.2 %) and the $1/2^+$ proton intruder state at an excitation energy of 307 keV (E_α = 6475(5) keV) [Coenen85]. The small α-decay branch of the ground state, b_α = 3.5(15) %, in combination with its long half-life of 67(3) s [Coenen85] makes it not suitable for obtaining clean recoil-α correlations. On the other hand, a total α-decay branch of $b_\alpha = 90^{+10}_{-20}$ % and an α-decay half-life of $T_{1/2}$ = 3.2(6) s of the $1/2^+$ intruder state [Coenen85] is a combination, which enables to perform an effective RDT analysis. An α-particle energy spectrum collected with the DSSD detectors in ^{193}Bi experiment is shown in Fig. 4.1.

The present study considerably extends the knowledge of the ^{193}Bi nucleus and results in a rather complicated level scheme, shown in Fig. 4.2.

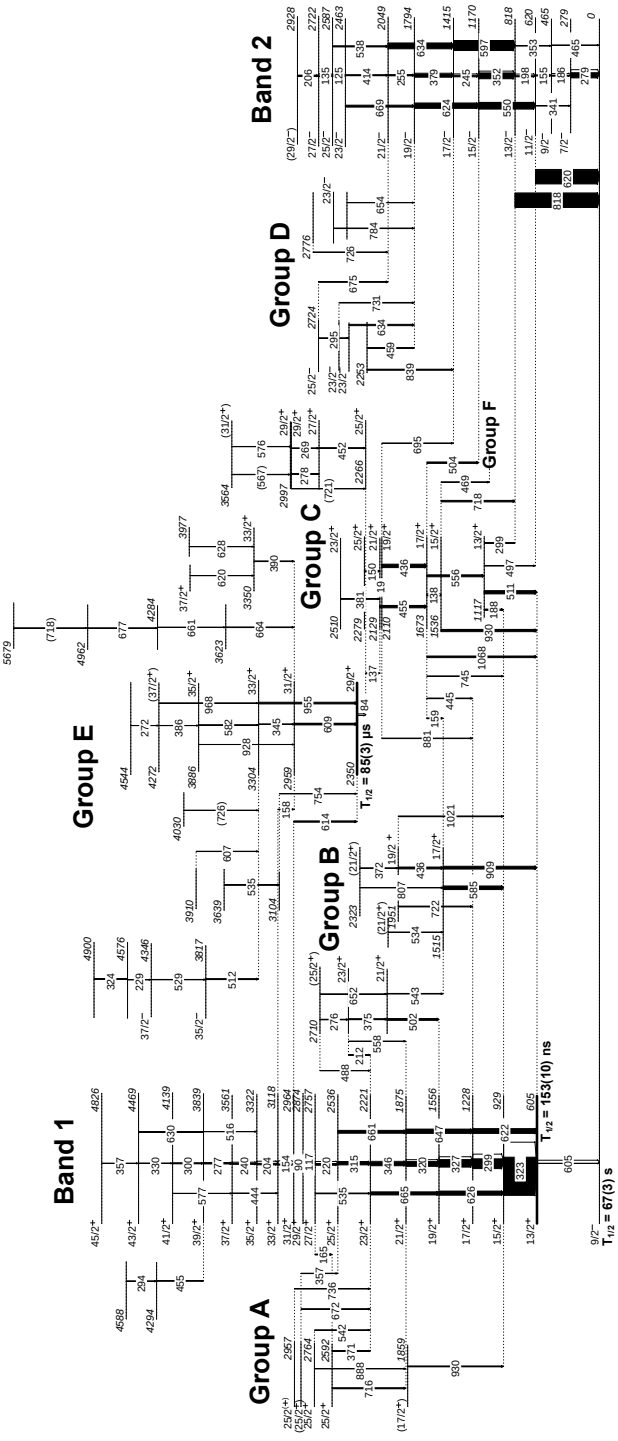

Figure 4.2: Level scheme of ^{193}Bi.

Figure. 4.2. - Continued.

Table 4.1: Energies E_γ, relative intensities (obtained from JUROGAM II data) I_γ, excitation energies E_i, and initial and final spins I_i^π and I_f^π, respectively, for the γ-ray transitions assigned to ^{193}Bi. Also angular distribution ratios R_{exp}(DCO) and linear polarization asymmetry factors A_P are shown. The intensities have been normalized with respect to the 323.4 keV $15/2^+ \rightarrow 13/2^+$ transition. The systematic error of about 0.3 keV should be added to the fitting errors given for most of the transitions listed in the first column.

E_γ (keV)	I_γ (%)	E_i (keV)	I_i^π	I_f^π	R_{exp}	A_P
Band 1						
90.0(5)	22(2)	2964	$31/2^+$	$29/2^+$		
117.1(1)	15.9(6)	2874	$29/2^+$	$27/2^+$	0.69(4)	
153.6(1)	29(1)	3118	$33/2^+$	$31/2^+$	0.78(4)	
164.5(1)	5.3(3)	2757	$27/2^+$	$25/2^+$		
203.9(1)	40(2)	3322	$35/2^+$	$33/2^+$	0.63(3)	-0.10(5)
220.4(1)	47(2)	2757	$27/2^+$	$25/2^+$	0.73(2)	-0.073(4)
239.8(1)	30(1)	3561	$37/2^+$	$35/2^+$	0.60(3)	-0.016(13)
276.5(1)	22.9(9)	3839	$39/2^+$	$37/2^+$	0.76(3)	-0.06(1)
294.4(1)	5.9(4)	4588				
299.2(1)	258(8)	1228	$17/2^+$	$15/2^+$	0.68(2)	-0.032(1)
299.8(1)	17.0(9)	4139	$41/2^+$	$39/2^+$	0.6(1)	
315.2(1)	63(2)	2536	$25/2^+$	$23/2^+$	0.79(4)	
323.4(1)	1000(57)	929	$15/2^+$	$13/2^+$	0.74(4)	-0.012(1)
327.4(1)	196(6)	1556	$19/2^+$	$17/2^+$	0.68(2)	-0.004(1)
330.3(2)	4.1(4)	4469	$43/2^+$	$41/2^+$	0.82(16)	
345.7(1)	86(3)	2221	$23/2^+$	$21/2^+$	0.68(2)	-0.059(6)
356.7(2)	2.5(3)	4826	$45/2^+$	$43/2^+$	0.7(2)	
443.8(4)	5.6(6)	3561	$37/2^+$	$33/2^+$		
454.9(2)	1.9(4)	4294		$39/2^+$		
516.4(2)	6.3(8)	3839	$39/2^+$	$35/2^+$	1.6(5)	
576.6(6)	6(1)	4139	$41/2^+$	$37/2^+$	0.85(25)	
604.7(1)[1]		605	$13/2^+$	$9/2^-$		
622.4(1)	121(5)	1228	$17/2^+$	$13/2^+$	1.30(16)	0.086(10)
626.2(1)	102(4)	1556	$19/2^+$	$15/2^+$	1.48(6)	0.094(9)
630.4(4)	1.9(3)	4469	$43/2^+$	$39/2^+$		
646.9(1)	108(4)	1875	$21/2^+$	$17/2^+$	1.47(6)	0.091(4)
660.7(1)	74(3)	2536	$25/2^+$	$21/2^+$	1.15(14)	0.060(3)
665.2(1)	80(3)	2221	$23/2^+$	$19/2^+$	1.2(1)	0.072(7)
Band 2						
124.6(1)	7.9(4)	2587	$25/2^-$	$23/2^-$		
134.7(1)	12.9(5)	2722	$27/2^-$	$25/2^-$	0.62(9)	
155.2(1)	7.0(5)	620	$11/2^-$	$9/2^-$		
186.3(1)	24(1)	465	$9/2^-$	$7/2^-$	0.52(14)	

Table 4.1 – Continued.

E_γ (keV)	I_γ (%)	E_i (keV)	I_i^π	I_f^π	R_{exp}	A_P
198.2(1)	29(2)	818	$13/2^-$	$11/2^-$	0.73(7)	
206.3(1)	12.6(6)	2928	$(29/2^-)$	$27/2^-$		
245.2(1)	42(2)	1415	$17/2^-$	$15/2^-$	0.67(5)	-0.12(2)
255.1(1)	18.3(8)	2049	$21/2^-$	$19/2^-$	0.66(10)	
278.5(1)	103(4)	279	$7/2^-$	$9/2^-$	0.9(1)	
341.1(2)	5.4(7)	620	$11/2^-$	$7/2^-$		
352.1(1)	154(5)	1170	$15/2^-$	$13/2^-$	0.72(6)	-0.036(4)
353.1(2)	7.7(6)	818	$13/2^-$	$9/2^-$		
379.4(1)	84(3)	1794	$19/2^-$	$17/2^-$	0.64(4)	-0.050(1)
414.3(1)	20.3(9)	2463	$23/2^-$	$21/2^-$	0.43(6)	-0.12(2)
465.2(6)	4(1)	465	$9/2^-$	$9/2^-$		
538.4(1)	29(2)	2587	$25/2^-$	$21/2^-$	1.40(17)	0.07(1)
550.0(1)	173(6)	1170	$15/2^-$	$11/2^-$	1.27(10)	0.06(2)
597.0(1)	260(9)	1415	$17/2^-$	$13/2^-$	1.05(10)	0.016(1)
619.7(1)	358(29)	620	$11/2^-$	$9/2^-$	0.85(9)	-0.059(6)
624.3(1)	136(5)	1794	$19/2^-$	$15/2^-$	1.20(5)	0.024(2)
634.1(1)	148(5)	2049	$21/2^-$	$17/2^-$	1.57(9)	0.07(1)
668.9(1)	50(2)	2463	$23/2^-$	$19/2^-$	1.48(12)	0.103(11)
817.9(1)	377(18)	818	$13/2^-$	$9/2^-$	1.22(4)	0.039(3)
Band 3						
103.4(1)	9.7(5)	2194	$19/2^-$	$17/2^-$	0.41(3)	
143.0(1)	34(2)	2337	$21/2^-$	$19/2^-$	0.95(5)	
146.8(1)	31(1)	2484	$23/2^-$	$21/2^-$	0.83(4)	
185.5(1)	36(2)	2670	$25/2^-$	$23/2^-$	0.71(6)	
204.4(1)	10.5(5)	4213	$(37/2^-)$	$35/2^-$	0.67(4)	
212.7(1)	5.1(4)	4009	$35/2^-$	$33/2^-$	0.76(5)	
231.9(4)	1.2(3)	4242	$(37/2^-)$	$35/2^-$		
252.5(1)	43(2)	2922	$27/2^-$	$25/2^-$	0.61(6)	-0.008(1)
263.1(1)	6.2(4)	4060	$(35/2^-)$	$33/2^-$	0.67(5)	
278.6(1)	41(2)	3201	$29/2^-$	$27/2^-$	0.92(8)	-0.053(4)
284.0(1)	5.9(5)	2194	$19/2^-$	$17/2^-$		
295.7(1)	24(1)	3497	$31/2^-$	$29/2^-$	0.57(5)	-0.096(6)
298.8(1)	32(2)	3796	$33/2^-$	$31/2^-$	0.60(5)	-0.093(6)
(334.7(3))	2.8(4)	2922	$27/2^-$	$25/2^-$		
438.1(4)	2.9(6)	2922	$27/2^-$	$23/2^-$		
512.7(1)	8.4(5)	4009	$35/2^-$	$31/2^-$		
530.9(2)	7.5(6)	3201	$29/2^-$	$25/2^-$	2.1(3)	
574.3(1)	10.9(7)	3497	$31/2^-$	$27/2^-$	2.2(3)	0.105(14)
595.9(1)	21(1)	3796	$33/2^-$	$29/2^-$		
631.4(1)	13.3(8)	2194	$19/2^-$	$15/2^-$		

Table 4.1 – Continued.

E_γ (keV)	I_γ (%)	E_i (keV)	I_i^π	I_f^π	R_{exp}	A_P
Band 4						
253.1(1)	8.8(6)	916	$11/2^-$	$9/2^-$		-0.14(2)
313.3(1)	11.5(7)	1563	$15/2^-$	$13/2^-$	0.61(8)	-0.049(9)
333.7(1)	22(1)	1250	$13/2^-$	$11/2^-$	0.66(10)	
347.6(2)	4.5(6)	1910	$17/2^-$	$15/2^-$		
383.8(1)	43(2)	662	$9/2^-$	$7/2^-$	0.91(5)	
450.6(1)	12.5(8)	916	$11/2^-$	$9/2^-$		-0.035(4)
587.0(1)	19(1)	1250	$13/2^-$	$9/2^-$		
636.7(1)	22(2)	916	$11/2^-$	$7/2^-$	1.15(7)	
647.3(1)	43(2)	1563	$15/2^-$	$11/2^-$	1.53(16)	
661.1(2)	10.2(9)	1910	$17/2^-$	$13/2^-$		
661.6(3)	19(3)	662	$9/2^-$	$9/2^-$	0.60(11)	
677.9(4)	10.0(8)	2241	$19/2^-$	$15/2^-$	1.41(23)	
784.5(2)	8.8(7)	1250	$13/2^-$	$9/2^-$	1.81(22)	
844.0(1)	17(2)	1910	$17/2^-$	$13/2^-$		
915.5(1)	61(4)	916	$11/2^-$	$9/2^-$	0.45(8)	0.012(2)
Band 5						
48.8(5)[1]		2405	$(29/2^-)$	$25/2^-$		
261.3(1)	7.6(5)	3710	$(37/2^-)$	$(35/2^-)$	0.81(14)	
289.5(1)	16.5(8)	3448	$(35/2^-)$	$(33/2^-)$	0.93(9)	-0.033(5)
318.8(1)	6.3(5)	4029	$(39/2^-)$	$(37/2^-)$		
355.3(1)	32(1)	3159	$(33/2^-)$	$(31/2^-)$	0.80(7)	-0.06(2)
386.4(3)	2.0(3)	3670	$(37/2^-)$	$(33/2^-)$	1.32(24)	
398.8(1)	55(2)	2804	$(31/2^-)$	$(29/2^-)$	0.61(6)	-0.016(5)
466.2(3)	1.9(3)	3750		$(33/2^-)$		
478.5(1)	20(1)	3282	$(33/2^-)$	$(31/2^-)$	0.63(9)	
550.6(2)	4.9(7)	3710	$(37/2^-)$	$(33/2^-)$	1.5(2)	
580.2(3)	3.3(5)	4029	$(39/2^-)$	$(35/2^-)$		
644.1(4)	3.0(7)	3448	$(35/2^-)$	$(31/2^-)$		
753.9(2)	12.7(14)	3159	$(33/2^-)$	$(29/2^-)$		
879.0(5)	5.8(8)	3282	$(33/2^-)$	$(29/2^-)$		
Band 6						
190.1(1)	4.3(3)	1205	$(9/2^+)$	$(7/2^+)$		
200.2(1)	50(2)	507	$3/2^+$	$1/2^+$	0.78(7)	
229.3(1)	16.2(8)	736	$5/2^+$	$3/2^+$	0.94(11)	-0.05(3)
278.9(7)	1.8(7)	1015	$(7/2^+)$	$5/2^+$		
356.4(5)	1.1(3)	1322				
429.0(2)	13(2)	736	$5/2^+$	$1/2^+$		
433.0(1)	19.0(9)	1638	$(13/2^+)$	$(9/2^+)$		
459.5(2)	5.2(5)	966		$3/2^+$		

Table 4.1 – Continued.

E_γ (keV)	I_γ (%)	E_i (keV)	I_i^π	I_f^π	R_{exp}	A_P
469.3(1)	14.6(8)	1205	$(9/2^+)$	$5/2^+$		
503.1(2)	4.4(6)	2141	$(17/2^+)$	$(13/2^+)$		
504.1(2)	5.8(8)	1519	$(11/2^+)$	$(7/2^+)$		
508.2(1)	35(2)	1015	$(7/2^+)$	$3/2^+$	0.95(12)	
Group A						
357.0(2)	5.6(5)	2894	$(25/2^+)$	$25/2^+$	0.82(7)	-0.178(14)
371.0(1)	8.1(5)	2592	$25/2^+$	$23/2^+$		
542.2(3)	3.2(6)	2764	$25/2^+$	$23/2^+$	0.74(9)	
672.5(1)	13.9(8)	2894	$(25/2^+)$	$23/2^+$	0.86(6)	0.010(1)
716.3(1)	27(1)	2592	$25/2^+$	$21/2^+$	1.33(8)	0.12(1)
736.1(1)	12.8(7)	2957	$25/2^{(+)}$	$23/2^+$	0.74(9)	
887.7(1)	10.8(7)	2764	$25/2^+$	$21/2^+$	1.9(4)	
929.6(1)	22(2)	1859	$(17/2^+)$	$15/2^+$	0.48(7)	0.13(2)
Group B						
212.3(2)	3.8(4)	2434	$23/2^+$	$23/2^+$		
276.0(1)	8.7(6)	2710	$(25/2^+)$	$23/2^+$		
371.7(2)	6.7(7)	2323	$(21/2^+)$	$19/2^+$	0.61(9)	
375.4(1)	18.9(9)	2434	$23/2^+$	$21/2^+$	0.84(12)	
435.7(1)	41(2)	1951	$19/2^+$	$17/2^+$	0.58(6)	-0.005(1)
488.3(2)	7.4(6)	2710	$(25/2^+)$	$23/2^+$	0.44(5)	
502.5(1)	41(2)	2058	$21/2^+$	$19/2^+$	0.62(5)	
534.3(3)	5.5(9)	2049	$(21/2^+)$	$17/2^+$	1.10(8)	
543.2(1)	15.0(9)	2058	$21/2^+$	$17/2^+$	1.28(13)	
557.5(2)	7.1(7)	2434	$23/2^+$	$21/2^+$		
585.3(1)	86(3)	1515	$17/2^+$	$15/2^+$	0.66(3)	-0.04(1)
651.5(4)	3.3(7)	2710	$(25/2^+)$	$21/2^+$		
721.6(1)	21(1)	1951	$19/2^+$	$17/2^+$	0.63(6)	
807.3(2)	10.1(9)	2323	$(21/2^+)$	$17/2^+$	0.83(19)	
908.7(1)	74(4)	1515	$17/2^+$	$13/2^+$	1.30(12)	0.056(12)
1021.2(1)	19(1)	1951	$19/2^+$	$15/2^+$		
Group C						
$(18.7(5))^2$	0.44(3)	2129	$21/2^+$	$19/2^+$		
137.1(1)	8.6(5)	2266	$25/2^+$	$21/2^+$	1.38(12)	
137.6(1)	10.0(5)	1673	$17/2^+$	$15/2^+$	0.77(8)	
149.8(1)	11.1(6)	2279	$25/2^+$	$21/2^+$	1.32(17)	
159.3(1)	5.6(4)	1673	$17/2^+$	$17/2^+$	1.08(15)	
188.3(1)	10.1(8)	1117	$13/2^+$	$15/2^+$		
268.9(1)	5.3(3)	2987	$29/2^+$	$27/2^+$	0.38(6)	-0.048(6)
278.1(2)	5.0(5)	2997	$29/2^+$	$27/2^+$	0.51(6)	-0.23(3)

Table 4.1 – Continued.

E_γ (keV)	I_γ (%)	E_i (keV)	I_i^π	I_f^π	R_{exp}	A_P
299.4(4)	4(1)	1117	$13/2^+$	$13/2^-$		
381.0(2)	13(1)	2510	$23/2^+$	$21/2^+$	0.98(12)	-0.27(4)
436.2(1)	77(3)	2110	$19/2^+$	$17/2^+$	0.7(1)	-0.11(2)
445.4(2)	10.6(8)	1673	$17/2^+$	$17/2^+$		
452.2(1)	14.9(7)	2719	$27/2^+$	$25/2^+$	0.8(1)	
455.4(1)	61(3)	2129	$21/2^+$	$17/2^+$	0.98(20)	0.119(14)
469.5(1)	16(1)	1536	$15/2^+$	$13/2^-$	0.80(16)	
497.5(2)	13(1)	1117	$13/2^+$	$11/2^-$	0.85(12)	-0.053(9)
504.0(1)	38(2)	1673	$17/2^+$	$15/2^-$	0.80(6)	0.15(1)
511.3(1)	76(7)	1117	$13/2^+$	$13/2^+$	0.93(8)	-0.16(2)
556.4(1)	50(2)	1673	$17/2^+$	$13/2^+$	1.37(9)	
(567.5(1))	8.4(5)	3564	$(31/2^+)$	$29/2^+$		
576.2(2)	6.1(5)	3564	$(31/2^+)$	$29/2^+$	0.85(19)	
695.1(1)	13.1(9)	2110	$19/2^+$	$17/2^-$	1.47(21)	
717.9(1)	40(2)	1536	$15/2^+$	$13/2^-$	1.02(20)	0.10(1)
(721.1(2))	7.9(6)	2987	$27/2^-$	$23/2^-$		
744.7(2)	11.5(9)	1673	$17/2^+$	$15/2^+$	0.79(14)	
881.3(2)	13(1)	2110	$19/2^+$	$17/2^+$	0.79(13)	
930.0(1)	58(4)	1536	$15/2^+$	$13/2^+$	0.89(9)	-0.18(2)
1067.8(1)	43(3)	1673	$17/2^+$	$13/2^+$	1.08(15)	0.07(3)
Group D						
295.1(5)	1.9(5)	2724	$25/2^-$	$23/2^-$		
459.2(2)	7.7(7)	2253		$19/2^-$		
634.3(1)	34(2)	2428	$23/2^-$	$19/2^-$	1.35(7)	
654.1(3)	4.5(7)	2448		$19/2^-$		
674.6(1)	23(1)	2724	$25/2^-$	$21/2^-$	1.6(3)	
726.0(2)	7.9(6)	2776		$21/2^-$		
731.4(1)	15.4(9)	2526	$23/2^-$	$19/2^-$	1.33(23)	0.08(1)
784.0(1)	14.2(8)	2578	$23/2^-$	$19/2^-$	1.25(14)	
839.2(1)	29.6(14)	2254	$(19/2^-)$	$17/2^-$		
Group E						
84.0(5)[1]		2350	$29/2^+$	$25/2^+$		
158.5(3)	2.5(4)	3118	$33/2^+$	$31/2^+$		
229.4(3)	1.4(3)	4576		$37/2^-$		
271.9(5)	0.9(3)	4544		$(37/2^+)$		
323.6(2)	5.5(6)	4900				
345.4(1)	11(1)	3304	$33/2^+$	$31/2^+$	0.66(9)	
386.5(4)	1.8(4)	4272	$(37/2^+)$	$35/2^+$		
390.5(2)	10.4(9)	3350	$33/2^+$	$31/2^+$	0.92(14)	
512.3(1)	25(2)	3817	$35/2^-$	$33/2^+$	0.73(12)	0.080(14)

Table 4.1 – Continued.

E_γ (keV)	I_γ (%)	E_i (keV)	I_i^π	I_f^π	R_{exp}	A_P
528.6(1)	8.6(6)	4346	$37/2^-$	$35/2^-$	<1	
535.0(5)	1.5(5)	3639				
582.1(2)	9.6(9)	3886	$35/2^+$	$33/2^+$	0.9(2)	
606.5(3)	8(1)	3910		$33/2^+$		
609.1(1)	39(2)	2959	$31/2^+$	$29/2^+$	0.88(13)	-0.017(4)
614.0(1)	46(3)	2964	$31/2^+$	$29/2^+$	0.7(1)	-0.07(2)
619.9(3)	5.8(9)	3970	$37/2^+$	$33/2^+$	1.18(12)	0.13(2)
627.5(4)	0.7(6)	3977		$33/2^+$		
661.3(4)	2.2(5)	4284				
664.0(1)	16(1)	3623		$31/2^+$		
677.2(7)	0.7(3)	4962				
(718.4(6))	0.9(3)	5679				
(725.5(9))	1.0(6)	4030		$33/2^+$		
754.0(5)	16.2(8)	3104		$29/2^+$		
927.9(4)	1.9(4)	3886	$35/2^+$	$31/2^+$		
954.7(1)	44(6)	3304	$33/2^+$	$29/2^+$	1.31(18)	0.060(3)
967.7(3)	2.8(4)	4272	$(37/2^+)$	$33/2^+$		
Group F						
232.1(3)	1.4(3)	2091	$17/2^-$	$15/2^-$		
242.9(2)	5.5(4)	2194	$19/2^-$	$19/2^+$		
328.2(3)	4.5(7)	2091	$17/2^-$	$(15/2^-)$		
351.1(1)	2.2(6)	1521	$13/2^-$	$15/2^-$	0.99(9)	
352.4(2)	5.3(6)	2091	$17/2^-$	$17/2^-$		
365.1(2)	4.2(4)	2722	$27/2^-$	$25/2^-$	0.86(16)	
435.6(1)	10.1(7)	2484	$23/2^-$	$21/2^-$	0.89(16)	
446.8(1)	26(2)	1067	$13/2^-$	$11/2^-$	0.85(11)	-0.09(1)
(455.1(5))	1.4(6)	1521	$13/2^-$	$13/2^-$		
528.2(2)	4.8(5)	2091	$17/2^-$	$15/2^-$	0.74(10)	
567.0(1)	23(2)	1737	$17/2^-$	$15/2^-$	0.83(8)	-0.155(14)
569.4(1)	31(2)	2091	$17/2^-$	$13/2^-$	1.32(12)	
605.2(2)	12(1)	1521	$13/2^-$	$11/2^-$	0.95(13)	
619.9(3)	11(2)	2711		$17/2^-$		
670.3(1)	25(2)	1737	$17/2^-$	$13/2^-$	1.85(22)	
679.2(1)	24(1)	2194	$19/2^-$	$17/2^+$	0.8(2)	0.15(2)
689.6(1)	14.2(7)	2484	$23/2^-$	$19/2^-$	1.45(30)	
793.5(2)	9(1)	1860	$15/2^-$	$13/2^-$	0.64(10)	
862.4(1)	16.3(8)	2091	$17/2^-$	$17/2^+$	0.92(8)	0.040(5)
901.7(1)	33(2)	1521	$13/2^-$	$11/2^-$	0.7(1)	0.127(14)
913.4(3)	5.7(9)	1980		$13/2^-$		
920.9(1)	33(2)	2091	$17/2^-$	$15/2^-$	0.77(8)	-0.12(3)
1023.6(2)	9.5(6)	2091	$17/2^-$	$13/2^-$		

Table 4.1 – Continued.

E_γ (keV)	I_γ (%)	E_i (keV)	I_i^π	I_f^π	R_{exp}	A_P
1066.6(1)	104(10)	1067	$13/2^-$	$9/2^-$	1.37(20)	
1156.8(3)	5(2)	1763	$(15/2^-)$	$13/2^+$		
1272.8(1)	15.3(8)	2091	$17/2^-$	$13/2^-$	1.28(24)	
Other						
(97.5)[3]	9(1)					
146.0(5)[4]	4.1(3)					
289.0(5)[5]	9(3)					
307.4(1)	27(1)	2356	$25/2^-$	$21/2^-$	1.28(13)	-0.002(1)
319.8(1)	125(4)	1875	$21/2^+$	$19/2^+$	0.60(2)	-0.039(2)
352.3(1)	13.3(10)	1610	$(13/2^-)$	$(11/2^-)$	0.73(16)	-0.023(7)
363.4(2)	9.5(9)	642	$7/2^-$	$7/2^-$	1.16(11)	
(388.2(5))	1.2(3)	3220		$29/2^-$		
393.4(1)[6]	27(1)	1652	$(15/2^-)$	$(11/2^-)$	1.26(16)	
394.0(1)[6]	8.3(5)	2046	$(19/2^-)$	$(15/2^-)$	1.26(16)	-0.076(11)
436.3(3)	2.7(4)	2046	$(19/2^-)$	$(15/2^-)$	1.5(5)	
444.0(5)[4]	4.5(3)					
476.0(1)	10.5(5)	2832	$29/2^-$	$25/2^-$	1.2(2)	
501.5(1)	9.7(5)	2547	$(21/2^-)$	$(19/2^-)$	0.9(1)	-0.053(8)
535.2(1)	17.8(8)	2757	$27/2^+$	$23/2^+$	1.4(2)	
571.1(2)	4.4(4)	3119	$(23/2^-)$	$(21/2^-)$	0.6(1)	
638.1(3)	3.1(5)	1258	$(11/2^-)$	$11/2^-$		
647.3(1)	43(2)	1563	$15/2^-$	$11/2^-$	1.53(16)	
793.1(1)	6.2(7)	1258	$(11/2^-)$	$9/2^-$	0.44(5)	
1258.1(1)	19(2)	1258	$(11/2^-)$	$9/2^-$	0.82(11)	

[1] A γ-ray transition depopulating the isomeric state.

[2] The energy of this transition is obtained from the difference of the level energies of the $19/2^+$ and $21/2^+$ members of Group C.

[3] Seen in coincidence with the 143.0, 146.8, 185.5, 252.5 and 278.6 keV transitions in the prompt γ-ray spectra.

[4] Seen in delayed coincidence with the members of Band 2 and the 307 keV transition.

[5] Seen in coincidence with the members of Band 1 in the prompt γ-ray spectra.

[6] The R_{exp} and A_P value applies for both transitions. The ordering of these two transitions is not clear as they are too close to each other in the coincidence γ-ray spectrum.

4.1.1 Band 1 - $i_{13/2}$

The $13/2^+$ band-head of Band 1, located at an energy of 605 keV, has a half-life of $T_{1/2}$ = 153(10) ns [Nieminen04]. The $13/2^+$ isomeric state decays to the ground state via 605 keV $M2$ transition. The yrast band feeding the $13/2^+$ isomeric state (Band 1) was previously observed up to $I^\pi = (29/2^+)$ [Nieminen04], with only tentative spin assignment of the two uppermost states.
In the present study, Band 1 has been extended up to $I^\pi = 43/2^+$ and an energy of 4.736 MeV (for corresponding transitions see Fig. 4.3(a)). Sharp band-crossing is taking place in Band 1 above $I^\pi = 25/2^+$. The energy of the $29/2^+ \rightarrow 27/2^+$ transition overlaps with the Bi X-ray peak with an energy of 89.8 keV. Particularly in this case, it is important to carefully examine γ-ray spectra gated on various γ-ray transitions. A side-feeding of the strongly-coupled Band 1 at relatively high spin $I = 39/2^+$ state is observed.
When gating with the 154 keV $M1$ transition, depopulating the $33/2^+$ member of Band 1, a strong γ-ray peak with an energy of 614 keV is revealed. This partial decay-out of the band at $I^\pi = 31/2^+$ is the reason for reducing the intra-band intensity flow, and will be discussed more in detail in section devoted to the $29/2^+$ isomer.
All the conclusions made above are verified using recoil-gated γ-γ and where possible, also γ-γ-γ-data. The angular distribution ratios R_{exp} combined with the information on the linear polarization asymmetry factors A_P, listed in Table 4.1, confirm the placement of levels reported by Nieminen *et al.* [Nieminen04], and extend the information up to the uppermost state of Band 1 observed in this study. Due to lack of statistics, only limited number of transitions can also be assigned the linear polarization asymmetry factor A_P.

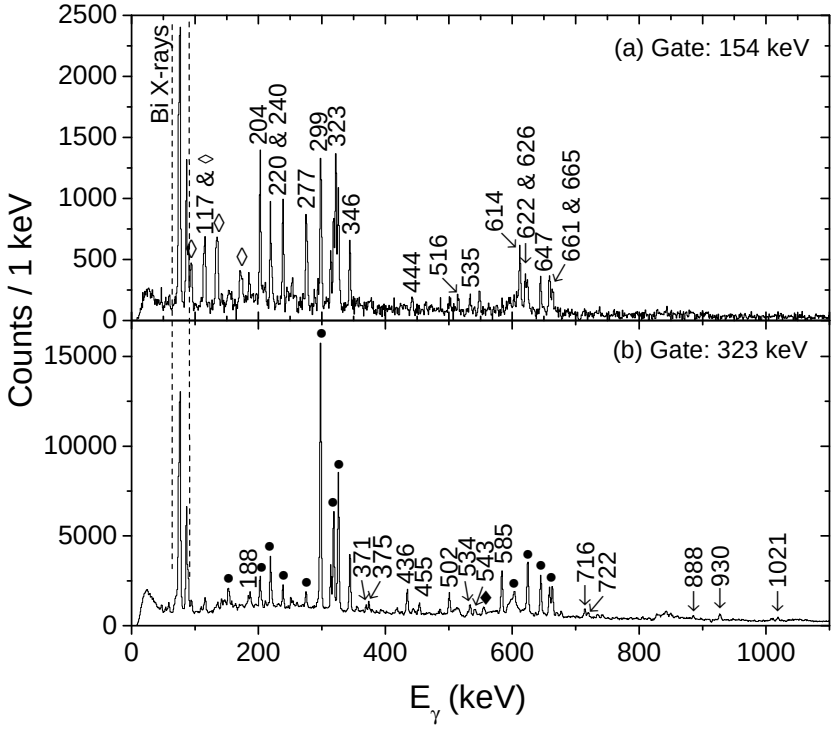

Figure 4.3: (a) An energy spectrum of prompt γ rays gated on the 154 keV transition. The peak assigned with energy 323 keV is a quadruplet consisting of 315, 320, 323 and 327 keV γ rays. (b) 323.4 keV-gated γ-ray energy spectrum, representing the transitions feeding Band 1. Peaks marked with circle symbol belong to γ-ray transitions of Band 1. Empty diamond symbols refer to γ-ray transitions originating in the decay of ^{165}Ho. Full diamond symbols denote the other γ-ray transitions belonging to ^{193}Bi.

4.1.2 Band 2 - $\mathbf{h}_{9/2}/\mathbf{f}_{7/2}$

The negative parity Band 2 was previously observed up to spin and parity of $(25/2^-)$ [Nieminen04]. The band-head remained unobserved and the uppermost states were only given tentative spin assignments. Nevertheless, the connection of Band 2 with the $9/2^-$ ground state was successfully established via strong 620 and 818 keV transitions, respectively, bypassing the band-head [Nieminen04].

The set of the strongest transitions of Band 2, predominantly intra-band $E2$ transitions, is used as a sum gate in the recoil-gated matrix of prompt γ-ray transitions (see Fig. 4.4). Transitions at energies of 124.6, 134.7 and 206.3 keV

are found to belong to Band 2. An $M1$ character has been assigned to all three transitions, which extend the band up to $I^{\pi} = 29/2^{-}$. The main decay out of the band via intense higher-energy γ-ray transitions with energies of 620 and 818 keV, depopulating the $11/2^{-}$ and $13/2^{-}$ states in Band 2, is the reason why the population of the band-head from the members of the band is weak. However, after close inspection of the coincident in-beam data, the $7/2^{-}$ band-head and also its decay to the ground state has been observed for the first time. The relevant transitions are energy labeled in Fig. 4.4. The intensities of these transitions are insufficient for any decent DCO or IPDCO analysis. Nevertheless, their ordering and/or placement in the level scheme, and hence electromagnetic character can be resolved on the basis of intensity ratios, energy sum arguments and γ-γ coincidence analysis.

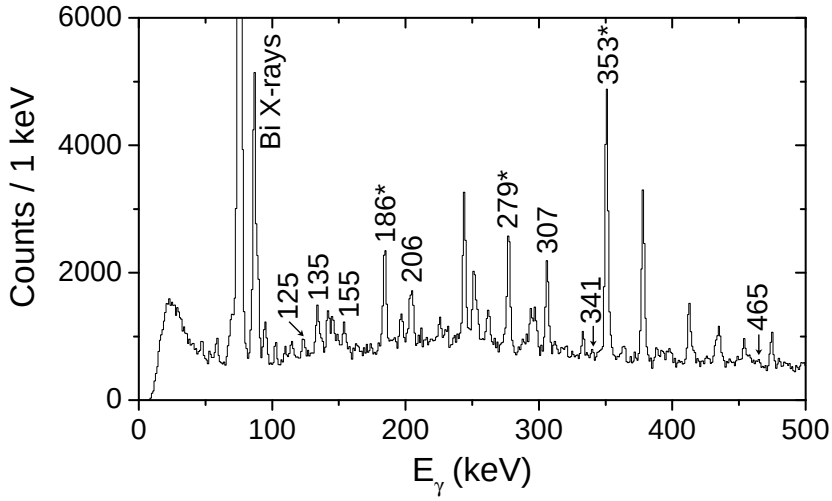

Figure 4.4: An energy spectrum of prompt γ rays gated on the 550, 634 and 818 keV transitions, showing the new transitions identified in this study. The extra intensity of the peaks with an asterisk sign comes from the other, strong γ-ray transitions feeding Band 2. Clear peaks without energy labels are all identified and they either belong to or feed Band 2 in ^{193}Bi.

4.1.3 Groups A, B and C

Bands 1 and 2 have extensive and rather complicated side-feeding. Band 1 is fed by de-excitation of the states with positive parity, forming Groups A, B and C. Most of these transitions are identified when gating with the 323.4 keV γ-ray transition in the prompt γ-γ matrix (see Fig. 4.3(b)). In total, more than 20 γ-ray transitions, with the energy ranging from 188 up to 1068 keV, have

been found to side-feed the Band 1 up to spin 25/2 (see Fig. 4.2). Majority of the states have been observed for the first time. Their population in this study is mostly weak, and in some cases the spin and parity assignments are only tentative. Despite the half-life (153 ns) of the $13/2^+$ band-head of Band 1, it is possible to gate with the corresponding 604.7 keV γ-ray transition with reasonable statistics at the target position and identify transitions populating the $13/2^+$ isomeric state.
As presented in Fig. 4.3(b), several transitions originating in the de-excitation of different states than those of Band 1 and feeding the $13/2^+$ isomeric state can be observed. They form one part of Group C.
Merging this observation with the one coming from the analysis of the delayed part of the isomer-tagged data enables to unambiguously identify the second $13/2^+$ state (Group C) in this nucleus. It mainly decays via emission of the 511.3 keV γ-rays to the $13/2^+_1$ state. Comparison of the corresponding γ-ray and conversion-electron spectra firmly excludes an $E0$ component for the 511.3 keV transition. On the basis of the angular distribution and linear polarization measurements, the 511.3 keV γ-ray transition is assigned a mixed $M1$+$E2$ character. Second main decay branch of the $13/2^+_2$ state is to the $11/2^-$ member of Band 2, via a 497.5 keV $E1$ transition. The previously observed $15/2^+$ and $17/2^+$ members of Group C (see Group A in [Nieminen04]), placed at 1.536 and 1.673 MeV, respectively, are found to have rather fragmented decays. The $13/2^+_2$ state is fed by 556 keV $E2$ transition, depopulating the $17/2^+$ state. This group of levels will be discussed more later.

4.1.4 Band 3 - $19/2^-$ and Band 4 - $\mathbf{h}_{9/2}$

In the previous study of ^{193}Bi [Nieminen04], one cascade of five low-energy γ-ray transitions (assigned as Group B in [Nieminen04]) remained floating, as the link to the rest of the level scheme could not be established. The lowest state of the cascade was suggested to be of isomeric character.
Inspection of prompt coincidences with these low-energy transitions reveals new γ-ray transitions with energies of 103.4, 143.0, 146.8, 204.4, 212.6, 231.9, and 263.1 keV, all associated with ^{193}Bi. The DCO analysis implies stretched dipole character for all of them. At first, the cascade of $M1$ transitions resembled a shears band similar to the one observed in ^{197}Bi [Mabala05], only located at lower excitation energy. This possibility has been ruled out by gating on the 143.0 and 146.8 keV transitions, respectively, and observing of several new γ-ray transitions grouped around 500 keV in the prompt coincident γ-ray energy spectrum. The energies of these γ-ray transitions are 438.1, 512.7, 530.9, 574.3 and 596.1 keV. After further analysis, an $E2$ character has been assigned to them. These transitions form, together with the previously identified cascade of transitions, a regular rotational band (Band 3). Using the Δ I = 2 intra-band transitions as a basis for the energy sum arguments, the ordering of transitions

within Band 3 can be firmly resolved. Finally, examining the γ-ray spectra gated on all known $M1$ members of Band 3 and their subsequent summation results in the extension of Band 3 up to an energy of 4242 keV and a spin and parity of $(37/2^-)$. There are no signs of any other $E2$ transitions above the $35/2^-$ state. The band structure starts to be irregular above this state, which may indicate that a band-crossing is also taking place in this band. The strongest transitions of Band 3 can be seen in Fig. 4.5.

The present data analysis reveals the decay of Band 3, which is prompt and fragmented. Many links between Band 3 and lower-lying collective and non-collective states have been identified (see Fig. 4.2), where the most prominent ones are discussed right below. Especially the 920.9 keV transition and the 569.4 keV plus 901.7 keV transitions combination are of the highest importance, as they connect Band 3 with negative parity Band 2 via an intermediate $17/2^-$ state (Group F) fed by the 103.4 keV $M1$ transition from the band-head of Band 3. The spins and parities of all states in Band 2 have been firmly assigned. Hence, the experimentally obtained knowledge of electromagnetic characters of these linking transitions allows to unambiguously determine the spins and parities of the most of Band 3 members. Since the decay of the $19/2^-$ state in Band 3 is quite complicated, and the state is fed by only one transition, together with the fact that the energies of $M1$ transitions within the band follow increasing trend with increasing spin, this state is assigned as a band-head.

Another important decay path of Band 3 proceeds via the 284 keV and 631 keV transitions to the newly found Band 4. The γ-ray spectra gated on the 284 and 916 keV γ-ray transitions (see Fig. 4.5) show transitions in this band. The γ-ray peak at 661 keV is identified to be a doublet, consisting of 661.1 and 661.6 keV γ-ray transitions. Gating predominantly with the 661.6 keV γ-ray (by placing a gate on the right side of the 661 keV γ-ray peak) (see Fig. 4.5(b)) reveals a γ-ray transition with the energy of 253.1 keV. Another γ-ray transition with almost equal energy can be seen in the level structure of ^{193}Bi. Nonetheless, the possibility of contaminating the 661.6 keV-gated γ-ray spectrum is firmly excluded. It is found that neither of the 253.1 keV and 661.6 keV transitions, is in coincidence with the 915.5 keV transition (see Fig. 4.5(c)). In both 661.6- and 915.5-gated γ-ray spectra, a group of the same lower-energy γ-ray transitions can be seen. The DCO analysis supports the $M1$ character assignment to aformentioned transitions.

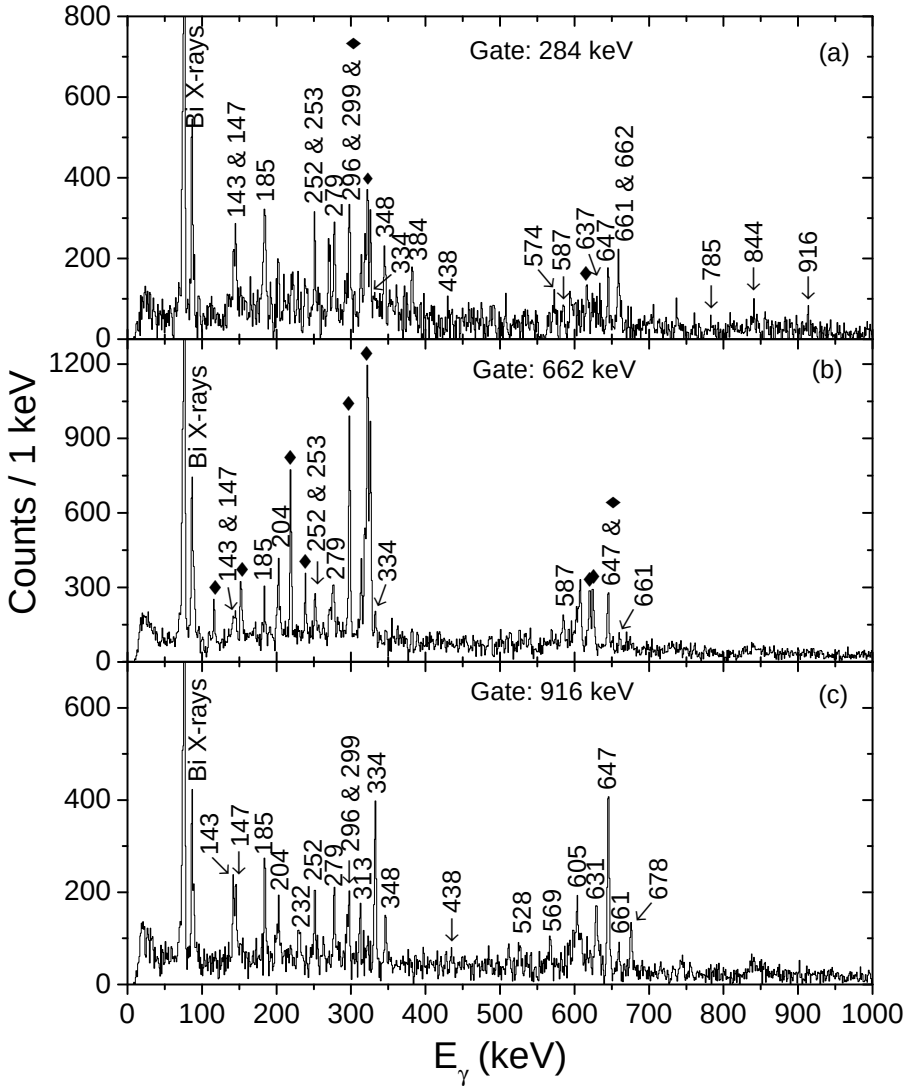

Figure 4.5: (a) 284 keV- and (b) 661.6 keV-gated γ-ray spectrum. Peaks marked with the diamond symbol refer to Band 1 γ-ray transitions and are due to the 661 keV transition in Band 1. (c) 915.5 keV-gated γ-ray spectrum.

Moreover, as demonstrated in Fig. 4.5, the gated spectra also involve a separate group of higher-energy γ-ray transitions centered around 600 keV, characteristic for regular cascades of $E2$ transitions. None of the low- and higher-energy transitions just mentioned belong to Band 3 or Group F. They form a cascade of $M1$ and $E2$ transitions, characteristic for strongly-coupled rotational band.

The observations just discussed lead to conclusion that the 661.6 keV γ-ray transition depopulates the $I^{\pi} = 9/2^{-}$ band-head of Band 4. In our study, Band 4 is observed up to an energy of 2.241 MeV and spin and parity of $19/2^{-}$. This newly observed strongly coupled band is found to be the main decay path of Band 3. Similarly to other rotational bands in this nucleus, the decay of the lower-spin states is rather fragmented.

4.1.5 Groups D and F

Many new γ-ray transitions are observed when gating on the γ rays from the lower part of the Band 2 in the prompt γ-γ matrix. They are divided to form two separate groups.
Group D in Fig. 4.2 is formed by the states, each of which is connected via only one transition with Band 2. Determination of spins and parities of Group D states is rather challenging, as the population of these states is weak. Nevertheless, the DCO analysis is possible to perform for some of the transitions (see Table 4.1), proving the negative parity for the majority of the states of Group D.
The second group of states (Group F) is placed on the right next to Band 2, shown in Fig. 4.2. The strongest of the transitions present in this group has energy of 1067 keV. It is found to depopulate the $13/2^{-}$ state to the $9/2^{-}$ ground state. When placing a gate on the 1067 keV γ ray in the same prompt γ-γ matrix, another relatively strong γ-ray transition with energy of 670 keV is revealed. Angular distribution measurement assigns a stretched quadrupole multipolarity to both transitions. Since no other comparably strong transitions are observed to be in coincidence with the 670 and/or 1067 keV transitions, the presence of another rotational band has been excluded.
Many other γ-ray transitions can be identified in the γ-ray energy spectra gated on the 1067 keV γ ray. On the basis of the DCO analysis and information obtained from the linear polarization measurements performed for these γ-ray transitions (see Table 4.1), all the states of Group F are assigned a negative parity.
Groups D and F, together with the positive parity Group C have been found to feed the negative parity states of Band 2 starting from spin 7/2 up to 21/2 (see Fig. 4.2).

4.1.6 Band 5 - $(29/2^{-})$ isomeric state

In the study by Nieminen *et al.* [Nieminen04], the $(29/2^{-})$ isomeric state was observed. The spin and parity assignment of this isomeric state was based on the systematic studies in this region of nuclear chart. At that time, it was known that the main decay flows to negative parity Band 2. The transition

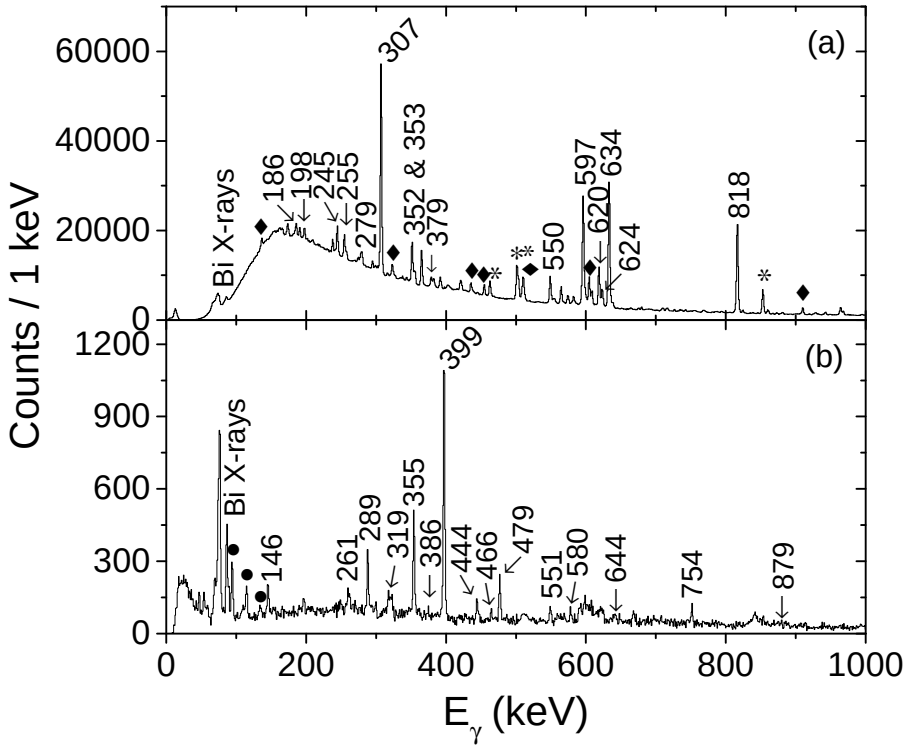

Figure 4.6: (a) A spectrum of γ-ray transitions observed at the focal plane clover detectors between 0 - 15 μs after the recoil implantation in the DSSD. Peaks marked with the diamond symbol represent γ-ray transitions originating in the decay of the $29/2^+$ isomer (see Fig. 4.2). (b) Energy spectrum of prompt γ-ray transitions gated on the 307 keV delayed γ-ray transition. Peaks marked with circles belong to ^{165}Ho.

depopulating the $(29/2^-)$ isomeric state remains unobserved. Instead, the γ-ray transition assigned as Δ was placed in the level scheme to depopulate this isomeric state to the intermediate $(25/2^-)$ state.
Nieminen *et al.* [Nieminen04] reported the half-life of 3.0(1) μs for the $(29/2^-)$ isomeric state. In Fig. 4.6(a) the γ-ray spectrum measured with the focal plane Ge detectors within 15 μs after the recoil implantation in the DSSDs is shown. All the prominent peaks in this spectrum are associated with the decay of this isomer. By projecting and fitting the time differences between the detection of the (ΔE-ToF condition) recoil and the most intense peak in Fig. 4.5(a), a delayed γ-ray transition with an energy of 307.4 keV, the half-life of this isomeric state can be remeasured. The final value of $T_{1/2}$ = 3.02(8) μs (see Fig. 4.7) is in a very good agreement with the previous observation. In order to examine the feeding pattern of the $(29/2^-)$ isomeric state, two approaches

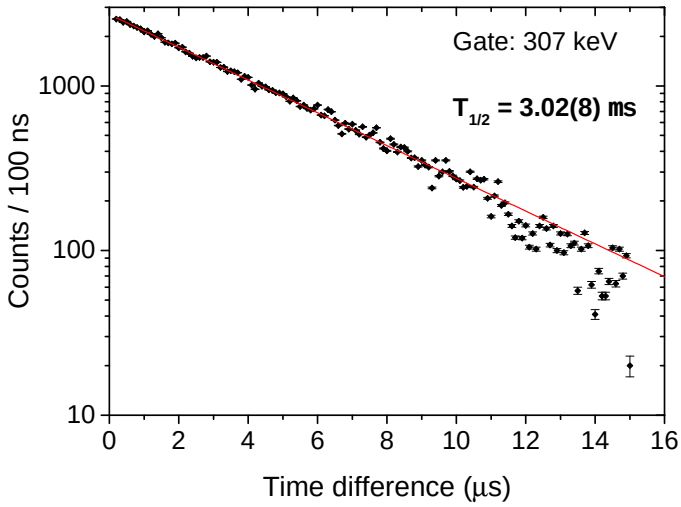

Figure 4.7: (Color online) Spectrum of time differences between recoil implantation and detection of the 307 keV transition in the focal plane clover detectors. The exponential decay law function was fitted to the data and is shown as the solid line through data points.

have been chosen. First, the 307.4 keV γ-ray transition is used as a gate in the delayed-prompt γ-γ coincidence matrix. As presented in Fig. 4.6(b), new γ-ray transitions with energies of 261, 319, 386, 466, 551, 580, 644 and 879 keV are observed. In the following step, the ordering of transitions in the structure built on top of the $(29/2^-)$ isomeric state is resolved by generating and inspection of an isomer-tagged γ-γ coincidence matrix of prompt γ-ray transitions. The search-time window for detecting the delayed γ-ray transitions is again 15 μs wide. As a result, the structure built on top of this isomer is extended to higher spin and energy, forming band-like structure Band 5 (see Fig. 4.2). Apparently, the 307.4 keV transition cannot depopulate the $(29/2^-)$ isomeric state, because it is also seen in the prompt γ-ray data of this experiment (see Fig. 4.4). Since no other comparably strong γ-ray transitions can be identified in the delayed γ-ray spectrum (see Fig. 4.6(a)), except those of Band 2, the de-excitation of the $(29/2^-)$ isomeric state must proceed via emission of another low-energy γ-ray transition. In previous study by Nieminen *et al.* [Nieminen04], the upper energy limit of 60 keV was given for the transition labeled as Δ. This limit was estimated based on the γ-ray and X-ray intensity analysis, and level energy systematics. The transition was preliminarily assigned an $E2$ character, thus being highly converted, $\alpha_{tot} \geq 71.8(10)$ [Kibedi08]. Due to low transition energy, the K-conversion is not possible. The L-conversion, which is dominating process for a (max) 60 keV γ-ray transition, would produce conversion electrons with energies less than 50 keV. In the present experiment, the PIN diode

detector of the focal plane setup has an energy threshold set close to 100 keV, thus considerably reducing the probability of their detection.
Spectrum of delayed γ-ray transitions detected in the focal plane planar detector gated on the prompt 398.8 keV transition, feeding the isomeric state, does not give clear evidence for Δ transition. Even gating with the individual transitions below the $(29/2^-)$ isomer in the focal plane clover detectors and looking at the corresponding coincidences in the planar detector γ-ray spectra does not reveal any such transition either. However, summing up all the planar detector spectra gated with the clean gates with energies of 379, 550, 597, 634 and 818 keV gives a clear evidence for the existence of the low-energy delayed γ-ray transition, with energy of 49 keV, as shown in Fig. 4.8. This γ-ray energy fits well within the energy limits given by level energy systematics. Moreover, in case of delayed-prompt γ-ray transitions coincidences, a peak at the same energy is also observed when applying the sum gate of prompt transitions feeding the isomeric state and detected in JUROGAM II. The 49 keV γ-ray transition is therefore attributed with the decay of the $(29/2^-)$ isomer. Consequently, it implies an excitation energy of 2.405 MeV for this isomeric state.
In order to assign a multipolarity and electromagnetic character to the 307.4 keV γ-ray transition, a conversion electron intensity analysis is utilized. For this purpose, electron-γ coincidences are inspected using the delayed γ-ray gated PIN diode spectra. As a result of gating on the strongest γ-ray transitions of Band 2, a conversion electron intensity ratio K/(L+M+N+...) = 1.37(12) is measured for the 307.4 keV γ-ray transition. This value overlaps with the theoretical value 1.26(4) for an $E2$ transition [Kibedi08]. This transition character assignment is also supported by the result of the DCO analysis, which gives R_{exp} = 1.28(13) for the 307.4 keV transition, hence indicating stretched quadrupole character.
Our studies also indicate an $E2$ character for the observed 49 keV transition. For the 49 keV $E2$ transition, the theoretical value for the total internal conversion electron coefficient is $\alpha_{th,Tot}$ = 192(3) [Kibedi08]. Comparison of the intensity balances between the 49 and 307.4 keV transitions gives an internal conversion coefficient α_{Tot} = 185(20), and matches the theoretical value for $E2$ transition rather well.
Results just presented make the ^{193}Bi the lightest Bi isotope, in which the full decay path of the $29/2^-$ isomer has been observed so far. Contrary to this observation, the $E1$ transitions were found to depopulate the $29/2^-$ isomeric states in ^{203,205,207}Bi [Lonnroth79, Hubel83], which are the only other known cases.

4.1.7 $29/2^+$ isomeric state

In the previous study [Nieminen04], one more long-lived isomeric state was reported. Its half-life and excitation energy remained unknown at that time. For

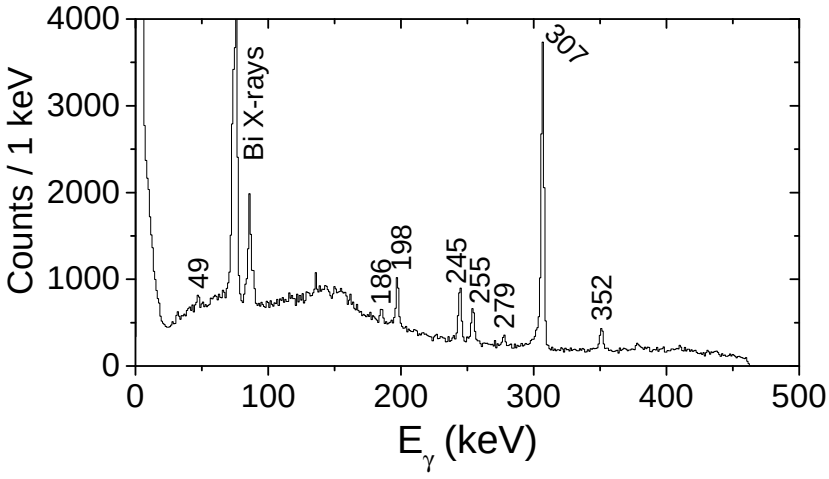

Figure 4.8: The spectrum of γ rays detected in the planar detector and in coincidence with the strongest γ-ray transitions in Band 2 detected in the focal plane clover detectors within 15 μs after recoil implantation.

the half-life, only a lower limit of $\sim$ 10 μs was suggested due to limitations of the DAQ system.
In Fig. 4.6(a), several transitions forming part of the fragmented de-excitation path from the isomeric state can be seen. It is obvious from the figure that a search-time window of 15 μs is not sufficient for the relevant transitions. Attempts to gain more statistics using longer search time between recoil implantation and the detection of the delayed γ-ray transitions do not improve the quality of the spectra due to substantially increasing background. On the other hand, employing recoil-electron correlations turns out to be very effective. A spectrum presented in Fig. 4.9(a) is generated by selecting the delayed γ-ray transitions, which are in prompt coincidence with electrons ($E_{electron}$ = 10 - 600 keV) detected in the same DSSD pixel as the recoil within time interval 15-400 μs (15 μs starting time due to the electronic read-out dead-time). Observations made in the analysis of the isomer-tagged focal plane γ-γ coincidence data of the present experiment confirm the conclusion in [Nieminen04], that the long-lived isomeric state de-excites via the 2110 and 2129 keV states (see Fig. 4.2). These levels are identified by observing the 436 and 455 keV γ-ray peaks in panel (a) of Fig. 4.9. As they appear to be the strongest transitions in the isomeric state decay path, they are also exploited for the isomeric state half-life determination, since no other isomeric state is expected to exist in between the corresponding states and the isomeric state of interest. A search-time window of 15 μs - 3 ms is chosen for selecting the delayed γ-ray transitions in order to minimize the uncertainty. As a result, the time projection (Recoil-γ Δt) of the 455 keV transition together with the corresponding

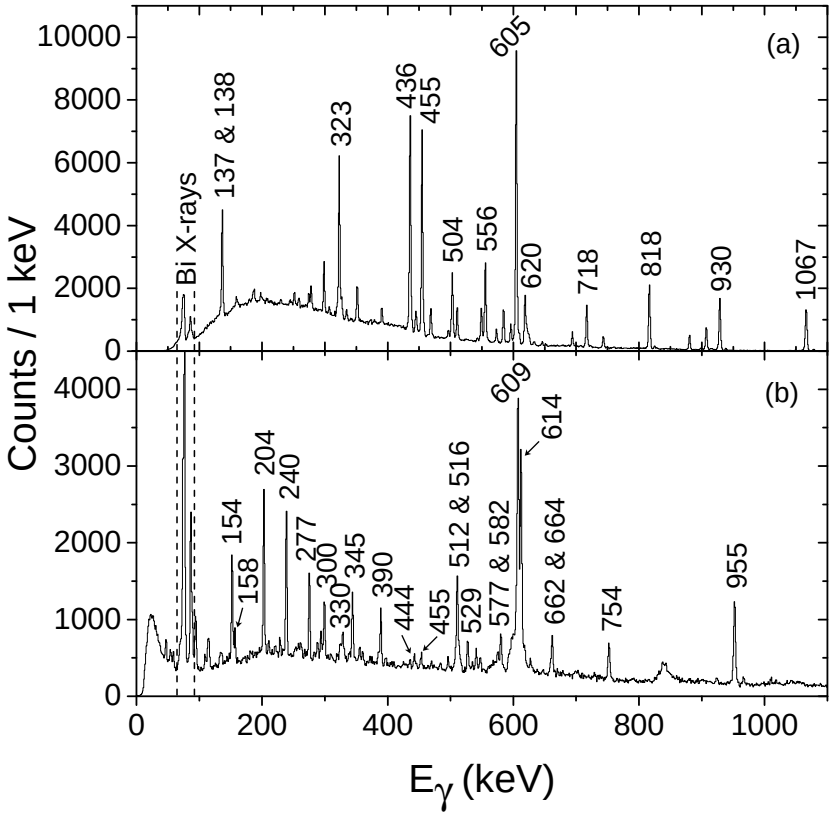

Figure 4.9: (a) An energy spectrum of γ rays detected in the focal plane clover detectors, in prompt coincidence with the electrons ($E_{electron}$ = 10 - 600 keV) detected in the same DSSD pixel as a recoil within 15-400 μs. (b) A spectrum of prompt γ rays followed by the decay of a long-lived isomeric state at the focal plane (panel (a)). All the prominent peaks are energy labeled.

fit is displayed in Fig. 4.10. It results in the measured half-life $T_{1/2}$ = 85(3) μs for the isomeric state. Time projections created by selecting and combining different γ-ray transitions of Group C (see Fig. 4.2) show similar lifetimes, and therefore only one example case is presented here.
In addition to the γ-ray transitions labeled in panel (a) of Fig. 4.9, other new transitions, all associated with the decay of the isomeric state, can be identified using the same isomer-tagged γ-γ matrix (see Group C in Fig. 4.2).

One 138 keV transition itself cannot explain the delayed γ-γ coincidences. It also appears to be self-coincident transition. In [Nieminen04], an 137 keV transition was placed between the 1673 and 1536 keV levels. In the present study,

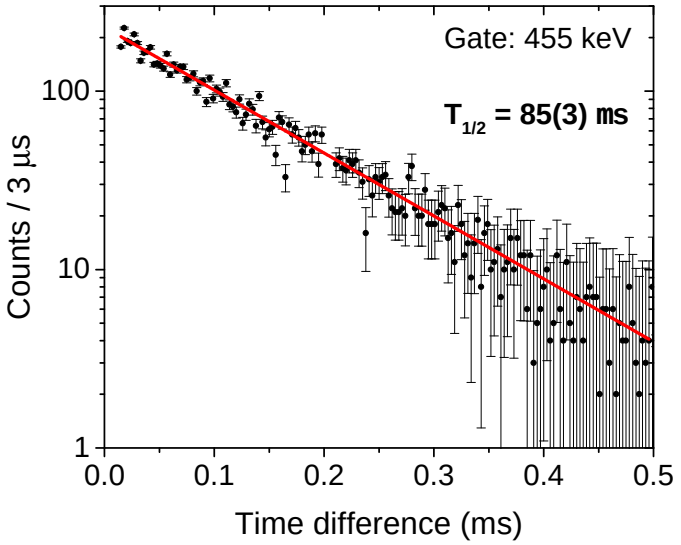

Figure 4.10: (Color online) Time difference spectrum of the recoil implantation and observation of the 455 keV transition (as one of the many transitions below the long-lived isomer) in the focal plane clover detectors. The exponential decay law was fitted to the data and is shown as the solid line through data points.

this transition has an energy of 138 keV and is assigned to be of $M1$ character. Another transition with almost equal energy of 137 keV is placed to feed the 2129 keV level. it is found that the decay path of the isomeric state must proceed via this transition. However, it is not possible for the isomeric state to be depopulated by emission of the 137 keV γ ray, because the γ-ray peak with the same energy is also seen in the isomer-tagged prompt γ-γ coincidence matrix. The isomer-tagged part of JUROGAM II data gives consistent results regarding the level structure of Group C. The part of the level structure of Group C lying above 2266 keV is all constructed on the basis of prompt γ-γ coincidences.

In the planar γ-ray spectra gated on the 137, 138, 436 and 455 keV transitions, a transition with an energy of 84 keV can be seen. Even though the 84 keV γ-ray peak is closely attached to the K X-ray peak, the statistics of the present experiment is high enough to firmly clarify this observation. The 84 keV γ-ray transition is assumed to directly depopulate the isomeric state. On the basis of the energy sum arguments, it subsequently implies an excitation energy of 2.350 MeV for the 85 μs isomeric state.

Two conditions have to be fulfilled to create the spectrum of isomer-tagged prompt JUROGAM II events shown in panel (b) of Fig. 4.9. First, only electrons detected in the DSSD within the time-window of 15-400 μs after recoil implantation are taken into account. Secondly, these correlated electrons have

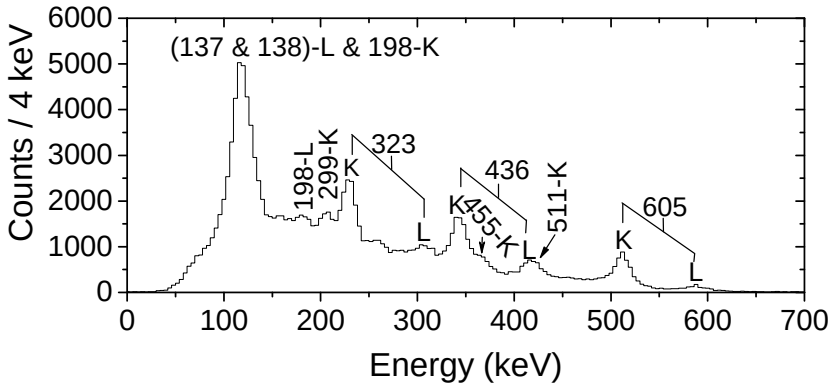

Figure 4.11: Recoil-DSSD-X-electron correlated conversion electron energy spectrum detected in PIN diodes; Δt (Re-DSSD-X-e$^-$) = 15 - 400 μs and Δt (PIN-e$^-$-DSSD-X-e$^-$) = -300 - 600 ns.

to be in prompt coincidence with the delayed γ-ray transitions (Δt = 30-450 ns). Importance of this spectrum is in setting the another constraint for the excitation energy of the 85 μs isomeric state and, as will be apparent later, also for its spin and parity assignment. In the low-energy part of this spectrum, γ-ray transitions assigned to Band 1 above the back-bending appear. Contrary to the 609.1 keV γ-ray transition, the 614.0 keV γ-ray transition is also seen when gating on the 153.6 keV γ-ray transition of Band 1 (see Fig. 4.3(a)). The 614.0 keV transition, visible also in Fig. 4.9(b), is found to drag the intensity out of Band 1 and directly feed the isomeric state. The cascade 158 + 609.1 keV provides a parallel link.

Results of the DCO analysis in combination with the linear polarization measurements dictate a stretched $M1$ character for both the 609.1 and 614.0 keV transitions. Ordering of the 153.6, 609.1 and 614.0 keV transitions in the level scheme then immediately implies a stretched $M1$ character for the 158 keV transition (see Fig. 4.2). More importantly, it leads to conclusion that the isomeric state has a spin and parity of $29/2^+$ and is located at an excitation energy of 2.350 MeV.

A level structure built on top of the $29/2^+$ isomeric state is constructed and labeled as Group E in Fig. 4.2. The corresponding γ-ray transitions are identified on the basis of prompt coincidences in the isomer-tagged JUROGAM II array γ-γ matrix, and its projection is present in panel (b) of Fig. 4.9. The $31/2^+$ states of Band 1 and Group E are only 5 keV apart (see Fig. 4.2). Due to closeness of these states, they are mixed, which is the most probable explanation for decay out of Band 1 to $29/2^+$ isomeric state. For several important transitions located below the $29/2^+$ isomeric state, values of their internal conversion coefficients are extracted from the isomer-tagged data collected at RITU focal plane. In order to get necessary information, the transition inten-

sities in Figs. 4.9(a) and 4.11 are compared. The 323 keV γ-ray transition is used for deducing of a normalization factor between these two spectra.
In case of Re-DSSD-X-electron correlated PIN diode energy spectrum shown in Fig. 4.11, the electron detection efficiencies from [Andreyev04] have been used. In this conversion electron energy spectrum, the peak with the lowest energy is located at $\sim$ 120 keV and corresponds mainly to L-conversion of the 137.1 keV and 137.6 keV transitions. Along with these transitions, there is also contribution to this peak from electron conversions of low-energy transitions with energies of 155, 159, 186, 188 and 198 keV. For most of these transitions, the contribution is negligible. Nonetheless, the intensity originating in K-conversion of the 198 keV $M1$ transition is noticeable and has to be subtracted from the total intensity of the 120 keV conversion electron peak. The theoretical internal conversion coefficient values α_{th}(L+M+...) for the previously discussed 137 keV $E2$ and 138 keV M1 transitions are 1.48(2) and 0.77(1) [Kibedi08], respectively. As mentioned above, the internal conversion of these two transitions creates a single peak in Fig. 4.11. Despite this difficulty, the experimental internal conversion coefficient is calculated, α(L+M+...) = 1.35(20), and is well understood as a weighted average of the two theoretical values for the $M1$ and $E2$ transitions. As can be seen in Fig. 4.11, the energy threshold of PIN diode detectors caused insensitivity for measuring the L-conversion of the 84 keV transition, and thus it cannot be analyzed in the similar way. Nevertheless, information obtained in Fig. 4.11 confirms the electromagnetic character assignments of the 436 keV and 455 keV γ-ray transitions.
In the same spectrum, the intensities of the peaks corresponding to K-conversion of these two transitions are very different. On the other hand, the 436 keV and 455 keV γ-ray intensities, as presented in panel (a) of Fig. 4.9, are almost equal. Therefore, they must be of different electromagnetic character. The experimental K-conversion coefficients are: (i) 436 keV, $\alpha_K = 0.133(19)$; (ii) 455 keV, $\alpha_K = 0.032(6)$. A consistency with the theoretical values: (i) $\alpha_{th,K} = 0.1379(20)$ for a pure $M1$ transition and (ii) $\alpha_{th,K} = 0.0262(4)$ for a pure $E2$ transition [Kibedi08] is rather good. Combination of the experimental internal conversion coefficients with the results of the DCO and linear polarization analyses leads to conclusion that the 137.1 keV and 455 keV transitions both have an $E2$ character. This yields a spin and parity of $25/2^+$ for the level located at an excitation energy of 2266 keV (see Fig. 4.2) and depopulated by an 137.1 keV transition. Once put all together, our analysis implies an $E2$ character for the 84 keV transition, and hence firmly confirms the spin and parity $I^\pi = 29/2^+$ for the 85 μs isomeric state.
The decay of the states located below the $29/2^+$ isomer is quite fragmented and creates a net of states and transitions labeled as Group C in Fig. 4.2. Description of Group C is summarized in a devoted section hereinbefore. The number of decays to positive ($M1$ transitions) and negative parity states ($E1$ transitions) is almost equal.

4.1.8 Band 6 - $1/2^+$ intruder state

Band 6 is built on top of the $1/2^+$ proton intruder state, located at 307(7) keV [Coenen85]. This intruder state predominantly decays via emission of an α particle. The emission of an $M4$ transition to the $9/2^-$ ground state is due to its high multipolarity extremely hindered. The structure above this intruder state can therefore be studied by means of the RDT technique. Selection of the transitions preceding to the recoil decay is done by gating with the α particles originating in the α decay of the band-head. Nieminen *et al.* [Nieminen04] reported the level sequence feeding the $1/2^+$ intruder state. Due to poor statistics, only tentative spin assignment of the levels was provided. The placement of several transitions was not resolved. Nonetheless, the γ-ray transition with an energy of 200 keV, tentatively assigned with $M1$ character, was placed directly feeding the $1/2^+$ intruder state.
As a result of the analysis of the α-tagged data of the present experiment, a band like structure (Band 6) feeding the $1/2^+$ intruder state is constructed. Panel (a) of Fig. 4.12 shows the energy spectrum of prompt γ-ray transitions as obtained by tagging with the 6475 keV α particles from the α decay of the $1/2^+$ intruder state. In the present study, the uppermost level of the band lies at excitation energy of 2.141 MeV and has a spin and parity $I^\pi = (17/2^+)$. Gating with the transitions located below the $(9/2^+)$ state of this band, only two intraband $E2$ γ-ray transitions connecting the $(13/2^+)$ and $(17/2^+)$ states can be seen. The energy of the $(15/2^+)$ state remains unknown. The band structure resembles a case when a strongly-coupled band becomes decoupled at higher spins. The intensity pattern of the $M1$ transitions observed in the analysis follows a zig-zag trend (see Table 4.1 and Fig. 4.2) characteristic for a regular rotational band, with stronger $M1$ transitions feeding the states of the favored signature. For the half-life of the $1/2^+$ intruder state in ^{193}Bi, distinct values can be found in literature, particularly $T_{1/2} = 1.9(4)$ s [Coenen85], $T_{1/2} = 3.15$ s [Gauvin72] and $T_{1/2} = 3.48(18)$ s [Tarantin71]. In this work, a search-time of 9.6 s is used in the α-decay analysis of the $1/2^+$ intruder state.
Due to the discrepancy between values of the aforementioned half-lives, a decay time analysis using a logarithmic time scale method [Schmidt00] of the present α-tagged part of data was performed. One complication arises from the fact that in the experimental data, the random rate in the DSSDs is comparable to the half-life of the $1/2^+$ state. Random and α-particle like treated recoils, and scattered beam particles (events that do not leave any energy signal in MWPC) represent the major components of the unwanted background in the decay-time distribution. To reduce the effect of random correlations on the half-life determination, only three corners of the DSSD (10×10 strips size) are used to collect the necessary information. Additionally, only part of data recorded at lower count rate is used. The decay-time distribution obtained by this method and fitted using function defined by Eq. 8 in [Schmidt00] is presented in Fig. 4.13. From the fit to the experimental data, an apparent

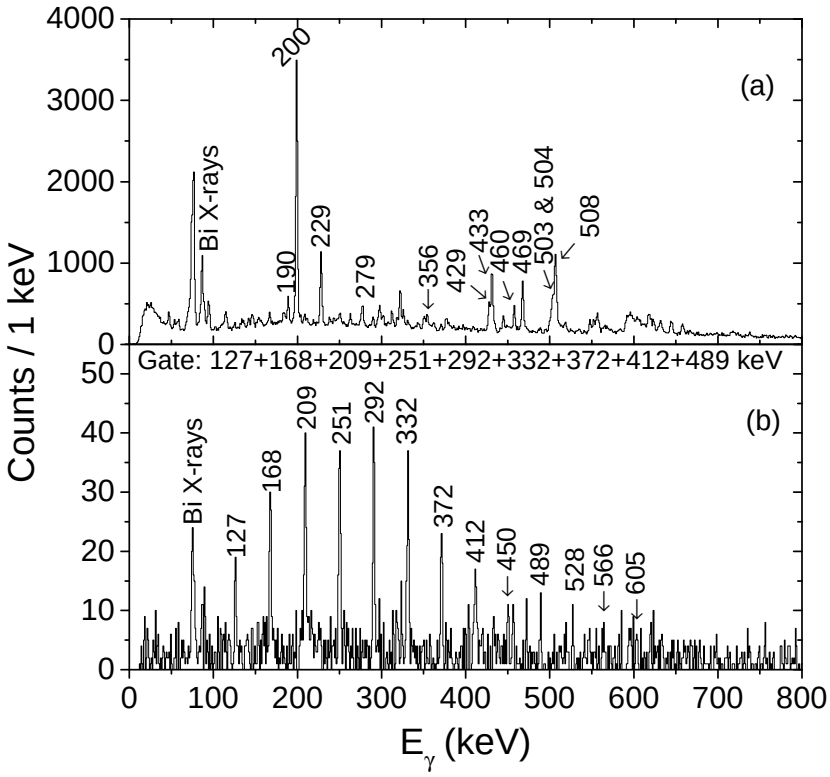

Figure 4.12: (a) Singles spectrum of γ rays tagged by the α decay of the $1/2^+$ proton intruder state. Search time of 9.6 s was used. (b) Sum of prompt γ-ray spectra gated with transitions connecting members of a superdeformed band assigned to ^{193}Bi. A matrix of JUROGAM II prompt γ-γ coincidences tagged with the α decay of the $1/2^+$ proton intruder state was used.

half-life $T_{1/2} = 2.68(4)$ s is obtained for the $1/2^+$ intruder state. Even though the effort is made to minimize the number of random correlations, the random background peak with its half-life 21(1) s is noticeable in this spectrum, and moreover, it is not well separated from the decay-time peak of the $1/2^+$ state. As a direct consequence, this overlap of the peaks causes the observation of the shorter than real half-life of the $1/2^+$ intruder state.

Since the half-life of the $1/2^+$ intruder state is not much shorter than the value of related random recoil rate, hence causing the overlap of the peaks in Fig. 4.13, an additional correction [Leino81] to the half-life is made. This correction should always be made, when the life-time of the true α decay is comparable with the rate of random events. In Fig. 4.13, also a small fraction of events, where the α decay is correlated with random recoil, is involved in the distribution obtained with half-life 2.68 s. For this reason, the fitted decay

constant is sum of $\lambda_{1/2^+}$ and λ_{bgr}. Finally, implementation of the corrected decay-time constant expression into the fitting function and applying it on the decay-time distribution measured at lower count rate gives the true half-life $T_{1/2} = 3.07(13)$ s.
A possibility exists for the $1/2^+$ intruder state to also decay via an EM transition to the $7/2^-$ band-head of Band 2. The transition would have an energy 28(7) keV. Internal conversion process is dominating for the $E3$ transition with such low energy. However, correlation with electrons and additional gating with bismuth X-rays does not provide a clean spectrum in this case. In addition, detection efficiency for so low-energy conversion electrons is a limiting factor.

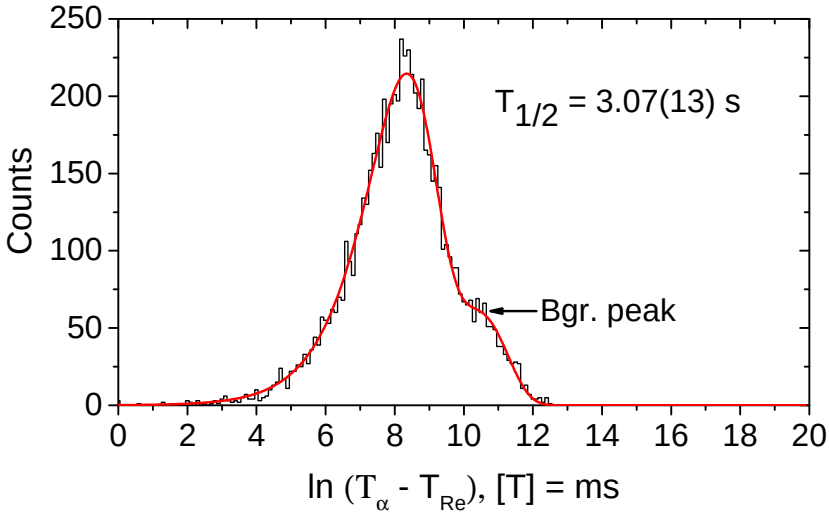

Figure 4.13: (Color online) The distribution of time differences between the recoil implantation and the detection of an α particle from the $1/2^+$ proton intruder α decay in the corners of the DSSD. Only part of data obtained with lower count rate of recoils was used to generate this distribution.

4.1.9 Superdeformed band

The analysis of the present data reveals the presence of a band of thirteen coincident transitions extending from 127 to (605) keV. An average energy difference of these transitions is 40 keV, i.e., consistent with the spacing expected for a superdeformed (SD) shape in this region [Chasman89]. The newly observed SD band is found by tagging on α decays of the $1/2^+$ proton intruder state. The total intensity of the band represents $\sim$ 3.9 % of the total population of this state. Summation of γ-ray spectra in coincident with the cleanest

Table 4.2: The energies (E_γ), relative intensities ($I_{\gamma(\alpha)}$) in the α-tagged gated spectrum, relative intensities ($I_{\gamma(rec.)}$) in the recoil-gated spectrum (rec-γ-γ-γ), excitation energy (E_i), spin and parity (I_i^π and I_f^π) of the initial and final states of the γ-ray transitions assigned to the SD band in ^{193}Bi.

E_γ (keV)	$I_{\gamma(\alpha)}$(%)	$I_{\gamma(rec.)}$(%)	E_i (keV)	I_i^π	I_f^π
126.6(2)[a]	0.72(19)		X + 127	$(15/2^+)$	$(11/2^+)$
168.3(1)	1.45(34)	0.8(6)	X + 295	$(19/2^+)$	$(15/2^+)$
209.5(1)	1.95(17)	1.22(34)	X + 504	$(23/2^+)$	$(19/2^+)$
250.9(1)	1.86(41)	1.97(36)	X + 755	$(27/2^+)$	$(23/2^+)$
291.7(1)	1.8(4)	1.75(29)	X + 1047	$(31/2^+)$	$(27/2^+)$
331.7(1)	1.62(37)	2.3(3)	X + 1379	$(35/2^+)$	$(31/2^+)$
372.2(1)	1.13(27)	1.71(23)	X + 1751	$(39/2^+)$	$(35/2^+)$
411.8(1)	0.84(22)	1.3(2)	X + 2163	$(43/2^+)$	$(39/2^+)$
450.4(2)	0.43(13)	1.25(20)	X + 2613	$(47/2^+)$	$(43/2^+)$
489.2(2)	0.36(12)	0.9(2)	X + 3102	$(51/2^+)$	$(47/2^+)$
527.8(1)	0.26(9)	1.44(20)	X + 3630	$(55/2^+)$	$(51/2^+)$
(566.0(2))	0.22(8)	1.1(2)	X + (4196)	$(59/2^+)$	$(55/2^+)$
(604.5(1))	0.22(9)	1.95(25)	X + (4800)	$(63/2^+)$	$(59/2^+)$
1836(5)[b]	0.9(2)				

[a] $I_{\gamma(rec.)}$ cannot be obtained from the LEVIT8R.
[b] A γ-ray transition seen in mutual coincidence with 168.3 and 331.7 keV transitions.

gates is presented in panel (b) of Fig. 4.12 (see also Table 4.2). A mutual coincidence of all the transitions in this cascade is confirmed by summing the spectra gated on all members of the SD band up to 489 keV transition, except a weak 450 keV transition, in LEVIT8R [Radford95a, Radford95b] using the recoil-gated γ-γ-γ cube. In the data, no signature partner of this band is found. In contrast to ^{193}Bi, two SD bands have been reported in ^{191}Bi [Nyman15]. It is the lightest bismuth isotope, in which superdeformation has been experimentally observed. These SD bands are interpreted as signature partner bands built on the proton $i_{11/2}$ $1/2^+$ [651] configuration. The newly found SD band in ^{193}Bi is identical to the other of the bands ($\alpha = +1/2$) in ^{191}Bi.
Considering the decay of the SD band to the $1/2^+$ intruder state, γ-ray transitions are searched for energies up to 4 MeV. In the assumption that a band head of SD band decays to the 307 keV energy level, the corresponding linking transition should be clearly visible in the related spectrum. In the α-tagged γ-ray spectrum presented in Fig. 4.14 there is evidence of a weak γ-ray transition with an energy of about 1836 keV. This transition is in clear coincidence with the 168 and 332 keV members of the observed SD band. In order to confirm the possible linking transitions connecting the SD band with Band 6, more statistics is required.

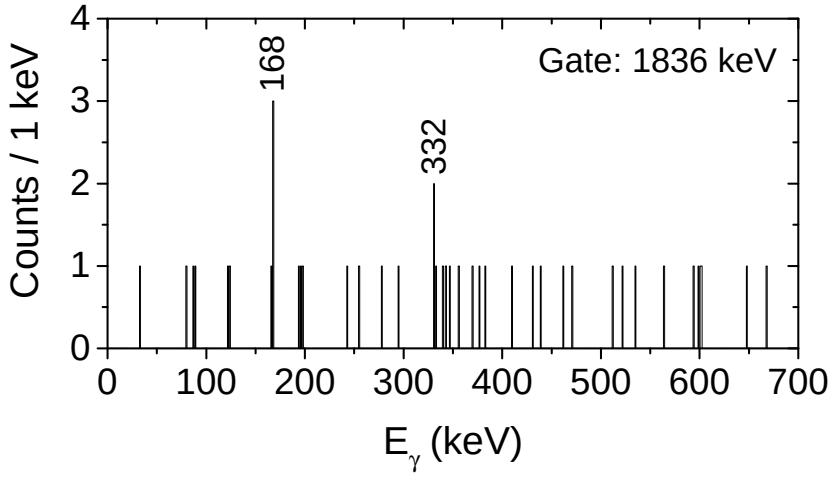

Figure 4.14: Prompt γ-ray spectrum tagged by the α decay of the $1/2^+$ proton intruder state and gated with the 1836 keV transition.

4.2 ^{195}Bi

In the experiment devoted to study the competing structures in ^{195}Bi, a fusion-evaporation reaction ^{159}Tb(^{40}Ar,xn)$^{199-x}$Bi was employed. The experiment itself was divided into two parts. In order to conduct the data analysis based on the recoil-gating and isomer-tagging techniques, a thin ^{159}Tb target deposited on the C-foil was bombarded with a stable ^{40}Ar beam, accelerated by K-130 MeV cyclotron to an energy of 175 MeV. The average beam intensity I_b was 9 pnA. In the JUROGAM II standalone part of the present experiment, a thick Au layer was used as a backing for the Tb target in order to stop the recoils inside the target chamber. While the beam energy optimized for production of ^{195}Bi nuclei remained the same, beam current was decreased to an average value of 3 pnA. As already demonstrated in panel (a) of Fig. 3.5, the JUROGAM II spectra collected in the backed-target part of the experiment contain γ-rays of a wide range of nuclei. Among others, products of transfer reactions, Coulomb excitations and fission have been observed in the relevant γ-ray spectra. The backed target experiments can be used to study short-lived isomeric states. In the present experiment, only isomeric states with half-lives longer than $\sim$ 90 ns could be studied separately at the target position, as the time resolution of the JUROGAM II array is found to be of the order of 80 - 90 ns, depending on the γ-ray energy.

In ^{195}Bi, two α-decaying states are known. The $9/2^-$ ground state, E_α = 5420(5) keV and E_α = 5713(5) keV, with a total α-decay branch of b_α = 0.03 % and an α-decay half-life of $T_{1/2}$ = 160(11) s. For the $1/2^+$ proton intruder

state located at E_{ex} = 410 keV, the α-decay characteristics are: E_α = 6106(5) keV, b_α = 33 % and $T_{1/2}$ = 87(1) s [Coenen85]. Such long half-lives in combination with small α-decay branches are not suitable for RDT analysis, as they do not provide clean recoil-α correlations. Regarding the knowledge on the structure of ^{195}Bi nucleus, quite limited information was available until the present study. The previous information on the ^{195}Bi was covered by experimental studies done by Lönnroth *et al.* [Lonnroth86], and rather recent one by Pai *et al.* [Pai12]. Two short-lived isomeric states, together with a band-like structure built upon the $13/2^+$ isomeric state have been reported.
Analysis of experimental data was performed in the similar way as described for ^{193}Bi data. The same set of spectroscopic tools was applied. If not otherwise specified, a time-window of 5 μs is used to search for recoil-delayed γ-rays correlations in the focal plane detector system. All the conclusions made in the following sections are verified by careful examination of γ-γ, and where possible, also γ-γ-γ coincidence data. As a result, a level scheme for ^{195}Bi is constructed and presented in Fig. 4.15. Widths of the transitions are proportional to the intensities in the recoil-gated JUROGAM II data. All the corresponding γ-ray transitions are listed in Table 4.3. Few example γ-ray spectra, which contributed most to construction of the level scheme are displayed, i.e. in Figs. 4.16 - 4.21.

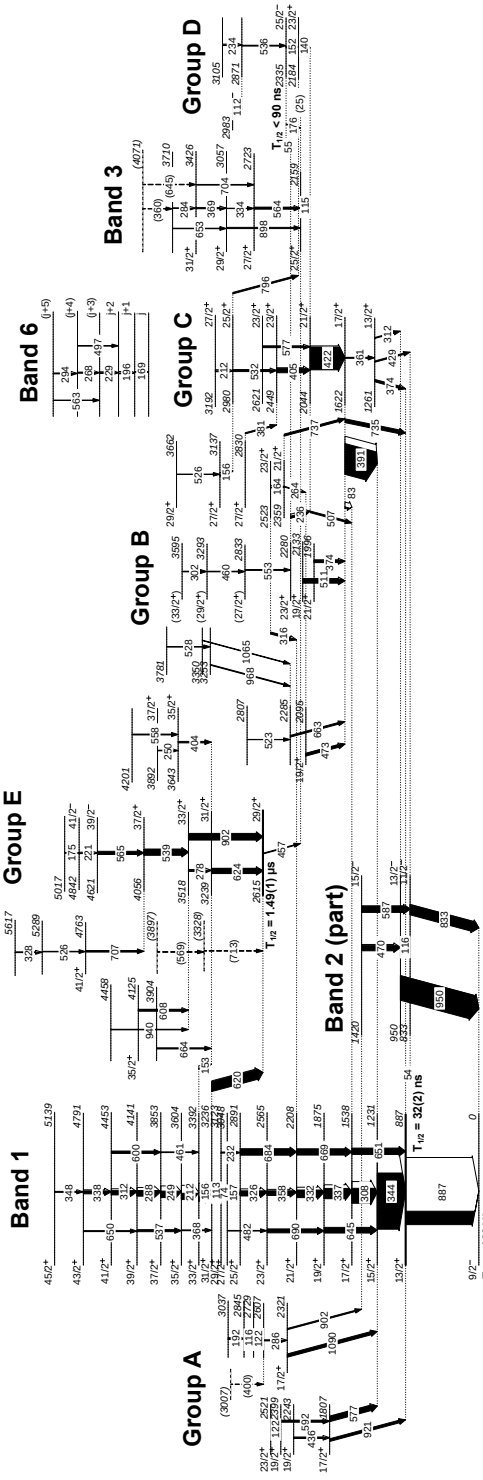

Figure 4.15: Level scheme of ^{195}Bi

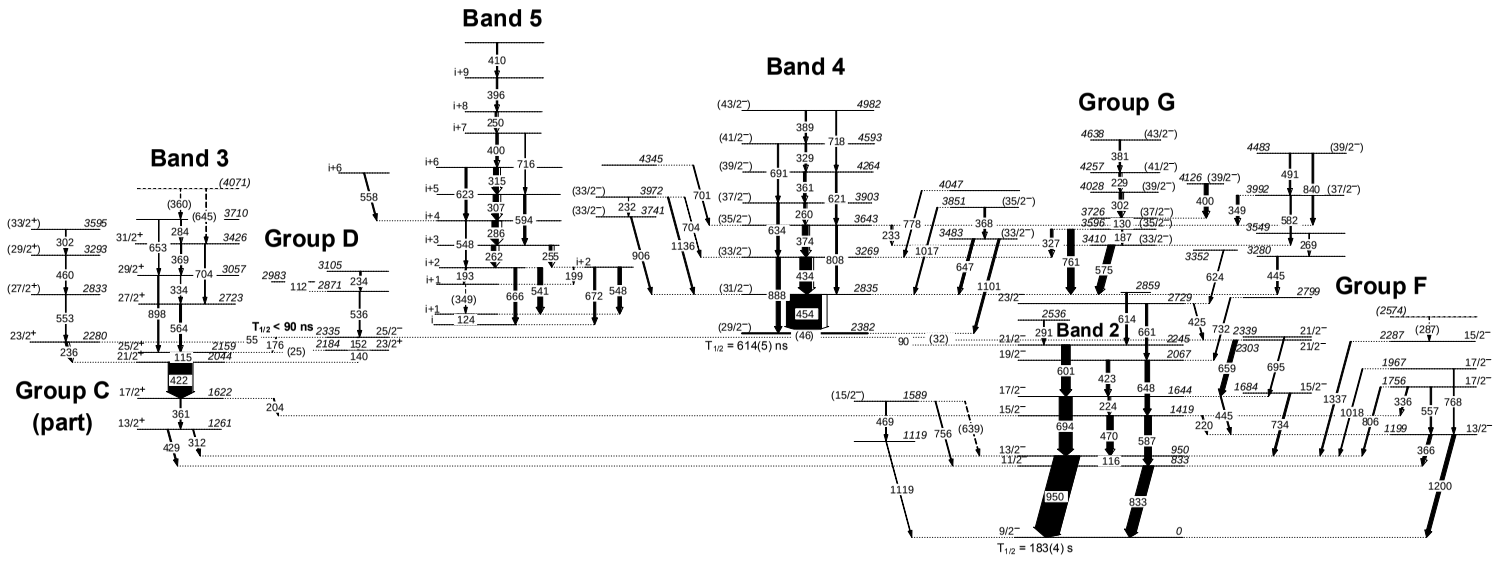

Figure. 4.15. - Continued.

Table 4.3: Energies E_γ, relative intensities (obtained from JUROGAM II data) I_γ, excitation energies E_i, and initial and final spins I_i^π and I_f^π, respectively, for the γ-ray transitions assigned to ^{195}Bi. Also angular distribution ratios R_{exp}(DCO) and linear polarization asymmetry factors A_P are shown. The intensities have been normalized with respect to the 343.8 keV $15/2^+ \rightarrow 13/2^+$ transition. The systematic error of about 0.3 keV should be added to the fitting errors given for most of the transitions listed in the first column.

E_γ (keV)	I_γ (%)	E_i (keV)	I_i^π	I_f^π	R_{exp}	A_P
Band 1						
54.5(5)[1]		887	$13/2^+$	$11/2^-$		
74.0(5)[2]		3122	$29/2^+$	$27/2^2$		
112.5(1)	25(1)	3236	$31/2^+$	$29/2^+$	0.75(9)	
156.2(1)	81(4)	3392	$33/2^+$	$31/2^+$	0.68(6)	
156.6(1)	40(2)	3048	$27/2^+$	$25/2^+$	0.60(6)	
211.6(1)	113(5)	3604	$35/2^+$	$33/2^+$	0.71(6)	
231.9(1)	13(1)	3123	$29/2^+$	$25/2^+$	0.96(12)	
249.4(1)	117(5)	3853	$37/2^+$	$35/2^+$	0.68(6)	
288.2(1)	101(4)	4141	$39/2^+$	$37/2^+$	0.63(7)	
307.7(1)	266(10)	1538	$17/2^+$	$15/2^+$	0.70(6)	-0.037(2)
311.7(1)	77(3)	4453	$41/2^+$	$39/2^+$	0.83(13)	
325.9(1)	91(3)	2891	$25/2^+$	$23/2^+$	0.76(7)	
332.3(1)	136(5)	2208	$21/2^+$	$19/2^+$	0.71(7)	
337.0(1)	184(7)	1875	$19/2^+$	$17/2^+$	0.75(7)	
338.2(1)	53(3)	4791	$43/2^+$	$41/2^+$	0.76(7)	
343.8(1)	1000(50)	1231	$15/2^+$	$13/2^+$	0.84(6)	
348.2(3)	12(1)	5139	$45/2^+$	$43/2^+$	0.87(22)	
358.1(1)	84(3)	2565	$23/2^+$	$21/2^+$	0.73(5)	
368.2(3)	13(1)	3604	$35/2^+$	$31/2^+$	1.3(3)	
460.6(1)	12(1)	3853	$37/2^+$	$33/2^+$		
482.2(2)	10(1)	3048	$27/2^+$	$23/2^+$	1.32(23)	
537.4(1)	35(2)	4141	$39/2^+$	$35/2^+$	1.59(17)	
599.7(1)	41(2)	4453	$41/2^+$	$37/2^+$		
644.7(1)	100(4)	1875	$19/2^+$	$15/2^+$	1.32(10)	0.059(4)
649.6(2)	17(1)	4791	$43/2^+$	$39/2^+$		
651.4(1)	115(6)	1538	$17/2^+$	$13/2^+$	1.24(12)	
669.2(1)	112(5)	2208	$21/2^+$	$17/2^+$	1.19(11)	
683.7(1)	116(4)	2891	$25/2^+$	$21/2^+$	1.17(12)	
690.2(1)	70(3)	2565	$23/2^+$	$19/2^+$	1.23(13)	
886.6(1)[1]		887	$13/2^+$	$9/2^-$		
Band 2						
116.1(2)	3.6(8)	950	$13/2^-$	$11/2^-$		
224.4(1)	23(1)	1644	$17/2^-$	$15/2^-$	0.66(10)	

Table 4.3 – Continued.

E_γ (keV)	I_γ (%)	E_i (keV)	I_i^π	I_f^π	R_{exp}	A_P
423.1(1)	52(2)	2067	$19/2^-$	$17/2^-$	0.69(10)	
469.8(1)	98(4)	1419	$15/2^-$	$13/2^-$	0.70(9)	
586.7(1)	114(4)	1419	$15/2^-$	$11/2^-$	1.33(13)	
601.0(1)	146(5)	2245	$21/2^-$	$17/2^-$	1.21(13)	
647.5(1)	79(3)	2067	$19/2^-$	$15/2^-$	1.14(13)	
661.3(1)	38(2)	2729	$23/2^-$	$19/2^-$	1.23(21)	
693.9(1)	223(8)	1644	$17/2^-$	$13/2^-$	1.11(11)	
832.8(1)	176(7)	833	$11/2^-$	$9/2^-$	0.67(8)	
949.8(1)	440(32)	950	$13/2^-$	$9/2^-$	1.32(11)	0.039(22)
Band 3						
283.9(3)	5.7(7)	3710		$31/2^+$		
334.4(3)	5(1)	3057	$29/2^+$	$27/2^+$		
(360.2(3))	4.9(8)	(4071)				
369.2(1)	16(1)	3426	$31/2^+$	$29/2^+$	0.6(1)	
563.6(1)	32(2)	2723	$27/2^+$	$25/2^+$	0.59(8)	
(644.6(2))	9.3(9)	(4071)		$31/2^+$		
652.6(7)	8.7(9)	3710		$29/2^+$		
703.6(1)	11(1)	3426	$31/2^+$	$27/2^+$	1.28(25)	
897.9(1)	22(1)	3057	$29/2^+$	$25/2^+$	1.57(23)	
Band 4						
(46.0(5))[3]		2382	$(29/2^-)$	$25/2^-$		
260.1(1)	33(2)	3903	$(37/2^-)$	$(35/2^-)$	0.82(9)	
329.2(1)	22(1)	4594	$(41/2^-)$	$(39/2^-)$		
361.1(1)	36(2)	4264	$(39/2^-)$	$(37/2^-)$	0.82(11)	
373.9(1)	101(4)	3643	$(35/2^-)$	$(33/2^-)$	0.70(7)	
388.8(1)	19(1)	4982	$(43/2^-)$	$(41/2^-)$		
434.1(1)	203(7)	3269	$(33/2^-)$	$(31/2^-)$	0.60(6)	
453.6(1)	609(20)	2383	$(31/2^-)$	$(29/2^-)$	0.64(6)	
620.8(1)	28(2)	4264	$(39/2^-)$	$(35/2^-)$	1.21(18)	
633.5(1)	41(2)	3903	$(37/2^-)$	$(33/2^-)$	1.33(15)	
691.3(1)	22(2)	4594	$(41/2^-)$	$(37/2^-)$	1.5(3)	
718.3(1)	14(1)	4982	$(43/2^-)$	$(39/2^-)$	1.4(3)	
807.5(1)	31(2)	3643	$(35/2^-)$	$(31/2^-)$	1.37(20)	
888.0(1)	72(4)	3269	$(33/2^-)$	$(29/2^-)$	1.23(15)	
Band 5						
123.9(1)			i+1	i	0.9(1)	
192.9(1)	8.4(6)		i+2	i+1	1.15(13)	
198.6(2)	5.8(6)		i+2	i+1		
250.2(1)	30(1)		i+8	i+7	0.84(9)	

Table 4.3 – Continued.

E_γ (keV)	I_γ (%)	E_i (keV)	I_i^π	I_f^π	R_{exp}	A_P
255.3(1)	50(2)		i+3	i+2	0.75(8)	
261.6(1)	79(3)		i+3	i+2	0.72(9)	
286.4(1)	110(4)		i+4	i+3	0.7(1)	
307.2(1)	92(3)		i+5	i+4	0.74(8)	
315.4(1)	86(3)		i+6	i+5	0.86(9)	
(348.6(1))	1(1)		i+1	i+1		
395.6(1)	21(1)		i+9	i+8	0.95(11)	
399.5(1)	34(2)		i+7	i+6	0.59(7)	
410.3(1)	18(1)			i+9		
541.4(1)	78(5)		i+2	i+1	0.98(10)	
547.7(1)	55(4)		i+2	i+1	0.66(8)	
548.0(1)	13(1)		i+4	i+2	1.36(36)	
593.6(1)	40(2)		i+5	i+3	1.1(2)	
622.6(1)	35(2)		i+6	i+4	1.06(11)	
665.6(1)	51(3)		i+2	i	1.46(16)	
671.9(1)	36(3)		i+2	i	1.39(19)	
716.5(1)	7.1(8)		i+7	i+5		
Band 6[4]						
169.0(2)			j+1	j	0.88(14)	
195.6(2)	17(2)		j+2	j+1	0.93(17)	
228.9(2)	15(1)		(j+3)	j+2		
268.4(1)	12(1)		(j+4)	(j+3)	(0.92(17))	
294.2(2)	10(1)		(j+5)	(j+4)	(0.98(19))	
496.6(9)	3(1)		(j+4)	j+2	(1.46(31))	
563.4(4)	5(1)		(j+5)	(j+3)	(1.6(3))	
Group A						
115.9(1)	10(1)	2845				
121.8(1)	13(1)	2729				
122.3(2)	6(1)	2521	$23/2^+$	$19/2^+$	1.25(10)	
192.5(1)	11(1)	3037				
286.1(2)	12(1)	2607		$17/2^+$		
(400(1))	3(1)	(3007)				
435.9(2)	21(2)	2243	$19/2^+$	$17/2^+$	0.73(6)	
576.6(1)	90(4)	1807	$17/2^+$	$15/2^+$	0.67(7)	
591.5(1)	33(2)	2399	$19/2^+$	$17/2^+$	0.61(6)	
901.7(2)	27(2)	2321	$17/2^+$	$15/2^-$		
920.9(1)	47(4)	1807	$17/2^+$	$13/2^+$	1.52(13)	
1090.1(1)	57(3)	2321	$17/2^+$	$15/2^+$	0.85(11)	
Group B						

Table 4.3 – Continued.

E_γ (keV)	I_γ (%)	E_i (keV)	I_i^π	I_f^π	R_{exp}	A_P
156.2(1)	16(1)	3136	$27/2^+$	$25/2^+$	0.7(1)	
163.6(1)	11(1)	2523	$23/2^+$	$21/2^+$	1.1(2)	
235.6(1)	37(1)	2280	$23/2^+$	$21/2^+$	0.9(1)	
264.1(3)	6.7(7)	2359	$21/2^+$	$19/2^+$		
302.0(1)	11(1)	3595	$(33/2^+)$	$(29/2^+)$	0.7(1)	
315.7(1)	26(2)	2523	$23/2^+$	$21/2^+$	0.67(8)	
374.3(1)	45(2)	1996	$21/2^+$	$17/2^+$	1.17(14)	
381.1(1)	19(1)	2830	$27/2^+$	$23/2^+$	1.5(2)	
459.7(1)	10(1)	3293	$(29/2^+)$	$(27/2^+)$	0.9(2)	
473.3(1)	44(2)	2095	$19/2^+$	$17/2^+$	0.75(12)	
511.3(1)	74(3)	2133	$19/2^+$	$17/2^+$	0.63(8)	
522.6(3)	4.6(8)	2807			1.4(4)	
525.8(2)	5.5(8)	3663	$29/2^+$	$27/2^+$	0.6(2)	
528.4(2)	9(1)	3781				
553.4(1)	11(1)	2833	$(27/2^+)$	$23/2^+$		
662.6(1)	28(2)	2285		$17/2^+$		
737.0(1)	35(2)	2359	$21/2^+$	$17/2^+$	1.28(18)	
968.1(1)	14(1)	3253				
1065.1(2)	9(1)	3350				
Group C						
83.0(5)[2]		1622	$17/2^+$	$17/2^+$		
203.8(1)	15(1)	1622	$17/2^+$	$15/2^-$	0.64(13)	
211.7(1)	16(1)	3192	$27/2^+$	$25/2^+$	0.67(11)	
311.7(1)	16(2)	1261	$13/2^+$	$13/2^-$	0.85(14)	
360.6(3)	17(1)	1622	$17/2^+$	$13/2^+$	1.25(18)	
373.8(2)	34(6)	1261	$13/2^+$	$13/2^+$	0.66(5)	
391.3(1)	537(17)	1622	$17/2^+$	$15/2^+$	0.83(7)	-0.013(1)
404.9(1)	75(3)	2449	$23/2^+$	$21/2^+$	0.66(7)	
421.8(1)	412(13)	2044	$21/2^+$	$17/2^+$	1.16(9)	0.023(1)
428.6(2)	23(2)	1261	$13/2^+$	$11/2^-$	0.83(13)	
506.8(1)	28(2)	2044	$21/2^+$	$17/2^+$	1.06(9)	
531.6(1)	32(1)	2980	$25/2^+$	$23/2^+$	0.66(7)	
577.1(1)	28(2)	2621	$23/2^+$	$21/2^+$	0.60(6)	
734.9(1)	67(4)	1622	$17/2^+$	$13/2^+$	1.06(15)	
796.2(1)	25(1)	2980	$25/2^+$	$23/2^+$	0.64(18)	
Group D						
(25.0(5))[5]		2184	$23/2^+$	$25/2^+$		
(32.0(5))[5]		2335	$25/2^-$	$21/2^-$		
55.0(5)[6]		2335	$25/2^-$	$23/2^+$		
90.0(5)[2]	16(9)	2335	$25/2^-$	$21/2^-$		

Table 4.3 – Continued.

E_γ (keV)	I_γ (%)	E_i (keV)	I_i^π	I_f^π	R_{exp}	A_P
111.6(2)	6.2(7)	2983			0.98(22)	
114.8(1)	19(1)	2159	$25/2^+$	$21/2^+$	1.13(8)	
140.2(1)	18(1)	2184	$23/2^+$	$21/2^+$	0.69(9)	
151.6(1)	20(1)	2335	$25/2^-$	$23/2^+$	0.81(6)	
176.0(1)	8.4(7)	2335	$25/2^-$	$25/2^+$	1.25(9)	
234.3(3)	13(1)	3105			0.82(6)	
457.1(3)[7]		2615	$25/2^+$	$29/2^+$		
535.6(2)	14(1)	2871		$25/2^-$		
Group E						
152.6(1)	14(1)	3392	$33/2^+$	$31/2^+$	0.84(14)	
175.0(2)	3.4(4)	5017		$41/2^-$		
221.1(1)	12(1)	4842	$41/2^-$	$39/2^-$	0.95(18)	
249.5(2)	6(1)	3892	$37/2^+$	$35/2^+$	0.62(11)	
278.2(1)	22(2)	3518	$33/2^+$	$31/2^+$	0.64(11)	
328.2(1)	8.6(7)	5617				
403.6(1)	25(2)	3643	$35/2^+$	$31/2^+$	1.24(18)	
526.1(1)	8.8(8)	5289		$41/2^+$		
538.7(1)	108(4)	4056	$37/2^+$	$33/2^+$	1.27(13)	0.099(12)
557.7(1)	15(1)	4201		$35/2^+$		
564.7(1)	57(2)	4621	$39/2^-$	$37/2^+$	0.58(9)	0.055(8)
(568.6(3))	7(1)	(3897)				
607.6(1)	32(3)	4125	$35/2^+$	$33/2^+$	0.83(19)	
620.2(1)	174(8)	3236	$31/2^+$	$29/2^+$	0.62(7)	-0.085(7)
623.9(1)		3239	$31/2^+$	$29/2^+$	0.81(16)	-0.109(20)
664.4(1)	3904	20(2)		$31/2^+$		
706.6(1)	27(1)	4763	$41/2^+$	$37/2^+$	1.45(25)	
(712.6(3))		(3328)				
902.3(1)	119(10)	3518	$33/2^+$	$29/2^+$	1.13(14)	
940.3(2)	10(1)	4458		$33/2^+$		
Group F						
219.6(2)	11(1)	1419	$15/2^-$	$13/2^-$	0.66(15)	
(286.7(4))	2.9(6)	(2574)		$15/2^-$		
290.8(1)	12(1)	2536		$21/2^-$		
336.4(1)	17(1)	1756	$17/2^-$	$15/2^-$	0.89(13)	
366.2(1)	45(2)	1199	$13/2^-$	$11/2^-$	0.69(10)	
425.3(2)	11(1)	2729	$23/2^-$	$21/2^-$		
445.3(1)	18(1)	1644	$17/2^-$	$13/2^-$	1.43(29)	
469.3(3)	8(1)	1588	$(15/2^-)$			
556.7(1)	24(2)	1756	$17/2^-$	$13/2^-$	1.14(21)	
613.8(1)	29(2)	2859		$21/2^-$		

Table 4.3 – Continued.

E_γ (keV)	I_γ (%)	E_i (keV)	I_i^π	I_f^π	R_{exp}	A_P
623.6(2)	12(1)	3352		$23/2^-$		
(639.3(3))	12(2)	1588	$(15/2^-)$	$13/2^-$		
659.4(1)	78(3)	2303	$21/2^-$	$17/2^-$	1.46(17)	
695.1(2)	27(3)	2339	$21/2^-$	$17/2^-$	1.48(29)	
731.6(2)	16(1)	2799		$19/2^-$		
734.1(1)	31(2)	1684	$15/2^-$	$13/2^-$	0.86(14)	
755.7(2)	14(2)	1588	$(15/2^-)$	$11/2^-$	1.15(25)	
767.7(1)	12(1)	1967	$17/2^-$	$13/2^-$		
806.1(2)	21(2)	1756	$17/2^-$	$13/2^-$	1.32(32)	
1017.5(2)	15(2)	1967	$17/2^-$	$13/2^-$	1.27(34)	
1118.8(3)	9(1)	1119		$9/2^-$		
1199.9(1)	67(5)	1199	$13/2^-$	$9/2^-$	1.24(20)	
1337.2(1)	23(2)	2287	$15/2^-$	$13/2^-$	0.59(16)	
Group G						
129.6(1)	12(1)	3726	$(37/2^-)$	$(35/2^-)$	0.77(12)	
186.6(3)	6.1(5)	3596	$(35/2^-)$	$(33/2^-)$	0.54(15)	
228.9(1)	28(1)	4257	$(41/2^-)$	$(39/2^-)$	0.91(10)	
231.6(1)	1.6(7)	3971	$(33/2^-)$	$(33/2^-)$		
233.2(1)	19(1)	3643	$(35/2^-)$	$(33/2^-)$	0.61(9)	
268.8(4)	4(1)	3549				
302.0(1)	53(2)	4028	$(39/2^-)$	$(37/2^-)$	0.94(10)	
326.9(1)	33(2)	3596	$(35/2^-)$	$(33/2^-)$	0.91(11)	
349.0(1)	37(2)	3992	$(37/2^-)$	$(35/2^-)$		
368.4(1)	24(2)	3851	$(35/2^-)$	$(33/2^-)$		
380.9(1)	20(1)	4638	$(43/2^-)$	$(41/2^-)$	0.84(14)	
400.3(1)	58(2)	4126	$(39/2^-)$	$(37/2^-)$	0.70(8)	
444.6(1)	21(2)	3280		$(31/2^-)$		
490.9(1)	22(1)	4482	$(39/2^-)$	$(37/2^-)$	0.5(1)	
557.7(1)	20(1)	4153	$(41/2^-)$	$(37/2^-)$	1.24(18)	
574.6(1)	110(4)	3410	$(33/2^-)$	$(31/2^-)$	0.61(7)	
581.8(1)	20(1)	3992	$(37/2^-)$	$(33/2^-)$	1.24(18)	
647.5(1)	40(2)	3483	$(33/2^-)$	$(31/2^-)$	0.77(13)	
701.5(1)	14(1)	4345		$(35/2^-)$		
703.6(3)	8(1)	3971	$(33/2^-)$	$(33/2^-)$		
761.2(1)	112(4)	3596	$(35/2^-)$	$(31/2^-)$	1.1(1)	
778.0(2)	14(1)	4047		$(33/2^-)$		
839.6(1)	29(2)	4482	$(39/2^-)$	$(35/2^-)$		
905.6(2)	21(2)	3741	$(33/2^-)$	$(31/2^-)$	0.72(16)	
1016.6(2)	20(2)	3851	$(35/2^-)$	$(31/2^-)$	1.6(4)	
1101.1(2)	37(5)	3483	$(33/2^-)$	$(29/2^-)$		
1136.1(1)	24(2)	3971	$(33/2^-)$	$(31/2^-)$	0.64(13)	

Table 4.3 – Continued.

E_γ (keV)	I_γ (%)	E_i (keV)	I_i^π	I_f^π	R_{exp}	A_P

4.2.1 Band 1 - $i_{13/2}$

In the study by Lönnroth [Lonnroth86], the delayed 888 keV $M2$ transition was placed in the level scheme as feeding the $9/2^-$ ground state of ^{195}Bi. In the time-delay curve for the 888 keV transition, a 32 ns time component was observed. Spin and parity $I^\pi = (13/2^+)$ were assigned to the 888 keV level. Pai *et al.* [Pai12] in their study assign the $13/2^+$ state at 887 keV to be a band-head of a rotational band.
A prompt γ-γ coincidence analysis confirms the observation in [Lonnroth86, Pai12], that the 344 keV transition feeds the $13/2^+$ state. The DCO analysis proves a stretched $M1$ character for this transition. The short life-time of the $13/2^+$ isomeric state allows to gate with the 887 keV $M2$ transition in the JUROGAM II γ-ray spectrum. As demonstrated in panel (a) of Fig. 4.16, the 344 keV transition is clearly dominating. Above the $15/2^+$ state, disagreements with the previously reported level schemes are found. Members of Band 1 in [Pai12] are different when compared to the present level scheme shown in Fig. 4.15. Panel (b) of Fig. 4.16 shows the 344 keV γ-ray gated spectrum. In this spectrum, among other strong transitions, the major part of γ-ray transitions feeding the $13/2^+$ isomeric state and forming Band 1 can be seen. In this study, the yrast band feeding the $13/2^+$ band-head (Band 1) is observed up to spin and parity $I^\pi = 45/2^+$ and energy of 5.139 MeV. Sharp band-crossing is taking place above $I^\pi = 25/2^+$. In the γ-ray spectrum gated on the 212 keV transition shown in Fig. 5.1(a), a transition at 620 keV is seen. It provides a link to another isomeric state in this nucleus, which will be discussed more in detail in the following sections.

In the planar spectra of delayed γ rays, a strong 55 keV transition appears. It is found that the corresponding γ-ray peak is a doublet. One delayed 54.5 keV $E1$ transition is placed in the level scheme as depopulating the $13/2^+$ band-head of Band 1. It feeds the $11/2^-$ state of Band 2 (see Fig. 4.15). No

[1] γ-ray transition depopulating $13/2^+$ isomeric state.
[2] The I_γ and R_{exp} could not be determined due to the strong contaminance of the peak by Bi K X-ray peak in the prompt γ-ray spectrum.
[3] γ-ray transition depopulating $(29/2^-)$ isomeric state.
[4] The intra-band transitions seen in coincidence with lower-lying members of Band 4 (strong coincidences with the 454 keV transition).
[5] The transition energy is determined by the difference of the initial and final level energies.
[6] The transition is seen in the planar spectra.
[7] γ-ray transition depopulating $29/2^+$ isomeric state. Transition seen in the focal plane data only.

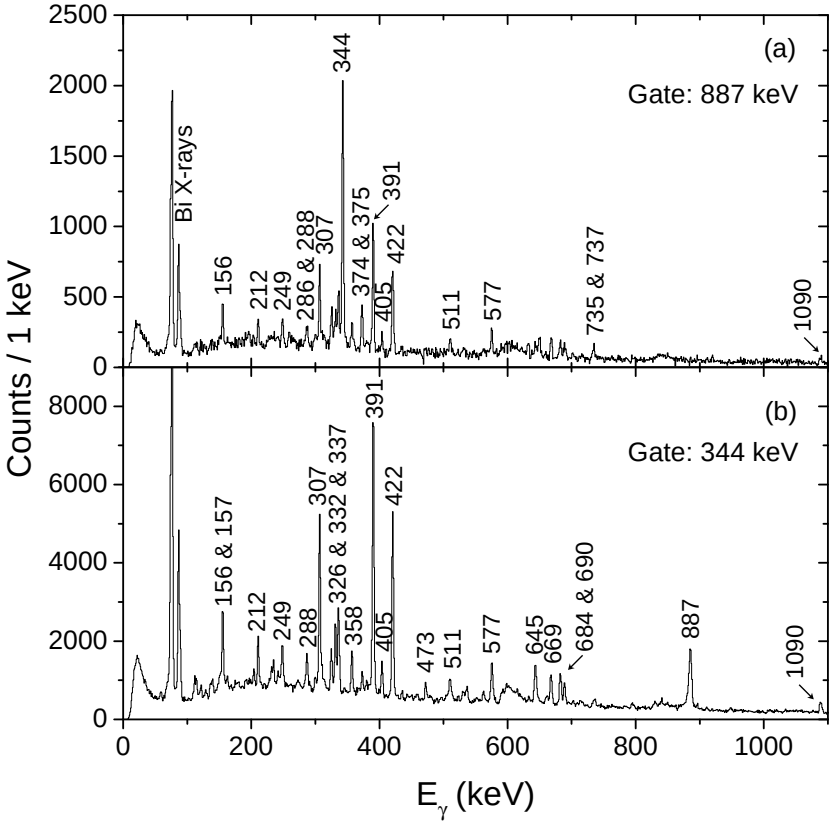

Figure 4.16: An energy spectrum of prompt γ rays gated with (a) 887 keV and (b) 344 keV γ-ray transition in ^{195}Bi data.

such direct link between positive and negative parity yrast bands is observed in ^{193}Bi nucleus.

4.2.2 Band 2 - $\mathbf{h_{9/2}/f_{7/2}}$

In this work, the negative parity band (Band 2) is observed for the first time. In contrary to ^{193}Bi, the $7/2^-$ band-head of Band 2 remains unobserved. The main decay-out of this band to $9/2^-$ ground state proceeds via emission of strong $E2$ γ-ray transition with energy of 950 keV. This transition bypasses the lower-energy transitions depopulating the states below $I^\pi = 11/2^-$ in Band 2.
Gates set on the 694, 833 and 950 keV transitions provide clean spectra for building Band 2. The transitions forming Band 2 are shown in Fig. 4.17. With the present statistics, it is possible to establish Band 2 up to spin and parity of $23/2^-$ and energy of 2.729 MeV. Similarly to Band 1, ordering of the intra-band transitions in the level scheme (see Fig. 4.15) is achieved by close inspection of γ-γ coincidences, energy sum arguments and intensity ratios.

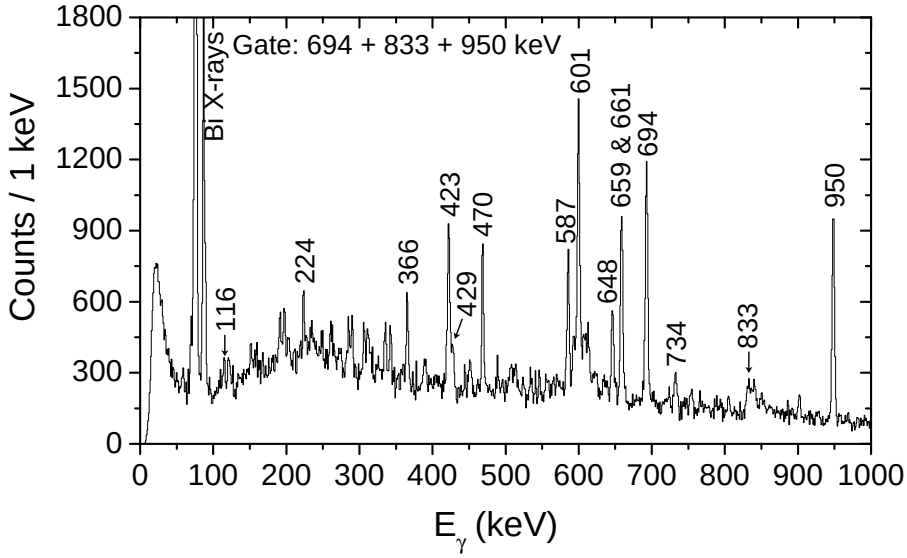

Figure 4.17: Sum of the prompt γ-ray spectra gated with 694, 833 and 950 keV transitions. In this spectrum, Band 2 members together with several side-feeding transitions can be seen.

4.2.3 Groups A, B and C

Group of positive parity states assigned as Group A is placed to the left of Band 1 in Fig. 4.15. Corresponding transitions are identified when gating with the 344 and 887 keV transitions in the prompt γ-γ coincidence matrix (see Fig. 4.16). Gating with the 887 keV transition in the γ-γ matrix of the backed target data also helps to resolve the placements and characters of the transitions side-feeding the $13/2^+$ isomeric state.
In Fig. 4.16, two strong γ-ray transitions with energies of 391 and 422 keV are observed. Due to their high intensities and prompt coincidences with the 344 keV transition, both transitions were previously placed as members band built on top of the $13/2^+$ isomeric state [Pai12]. In agreement with observations in [Lonnroth86], the 391 $M1$ and 422 keV $E2$ transitions are placed to depopulate the $17/2^+$ and $21/2^+$ states, respectively. In the present level scheme (see Fig. 4.15), these levels are placed as members of another group of positive parity states (Group C). Close inspection of prompt γ-γ coincidences reveals similar pattern in feeding Bands 1 and 2 from decay of the positive parity states of Group C as in the case of ^{193}Bi (see Group C in Fig. 4.2). The second $13/2^+$ state is identified and placed at an energy of 1261 keV. It decays to the $13/2^+$ isomeric state via emission of 374 keV $M1$ transition. Similarly to ^{193}Bi, it is fed by just one $E2$-type transition with energy of 361 keV. However, in contrast to ^{193}Bi, no $15/2^+$ state is observed.
Further examination of the 391- and 422-keV gated JUROGAM II coincident spectra reveals new transitions grouped together to form Group B in the level scheme (see Fig. 4.15). Most of the transitions in this group are of low intensity, and hence the spins and parities of corresponding levels remain tentative.

4.2.4 High-spin isomeric states

In [Lonnroth86], the existence of an isomeric state with $T_{1/2}$ = 750 ns and lying above 2311 keV was inferred. On the basis of the systematic behavior in heavier odd-A Bi isotopes, the isomeric state was expected to have a spin and parity of $29/2^-$. Pai *et al.* in their work [Pai12] suggested that the $29/2^-$ isomeric state decays to the $25/2^-$ state by a low-energy 86 keV $E2$ transition. Hence, they proposed the excitation energy of the $29/2^-$ isomeric state to be 2396 keV.
In the present work, an existence of the $29/2^-$ isomeric state is confirmed by the analysis of the focal plane data. However, a delayed 86 keV transition is observed neither in the focal plane clover nor in the planar γ-ray spectra.
In the focal plane clover spectrum, new transitions with energies of 140 and 176 keV are observed. Transitions of the same energies are also seen in the prompt γ-ray spectra, hence they cannot depopulate the $(29/2^-)$ isomeric state. The measured intensities are however much lower than the intensities of the 391

and 422 keV transitions in the prompt γ-ray spectra. It turns out that the 176 keV transition feeds the $25/2^+$ state at energy of 2.159 MeV. The 140 keV $M1$ transition is identified to depopulate the $23/2^+$ state placed at 2.184 MeV in the present level scheme (see Fig. 4.15). Inspection of the delayed-prompt coincidences reveals several new low-energy transitions. In the JUROGAM II data, a strong 454 keV γ-ray transition appears. It is found to be in prompt coincidence with another, relatively strong transition with an energy of 434 keV. Panel (a) of Fig. 4.18 shows the spectrum gated with the prompt 434 and 454 keV transitions, and measured by the planar detector. Along with the strongest transitions of Group C, the transitions with energies of 55, 90, 115, 140, 152 and 176 keV are seen in the gated planar spectrum. In the delayed γ-γ coincidence analysis, the 140 and 176 keV transitions, together with the previously observed 115 and 152 keV transitions are found to form a new level structure (Group D in Fig. 4.15) feeding the $21/2^+$ state of Group C. The information obtained from the DCO analysis dictates an $E1$ character for the 152 and 176 keV transitions, thus proving a negative parity for the I = 25/2 state of Group D. In order to explain different intensity patterns of the Group D transitions in JUROGAM II and focal plane data, respectively, the $25/2^-$ state must as well be of isomeric nature.

Considering the $25/2^-$ state of Group D, short level life-time cannot be extracted from the recoil-gated data of the present experiment, because this state is fed by the decay of an isomeric state with much longer life-time. Hence, the information on the shorter life-time gets lost. Additionally, γ-γ coincidence data of the backed target part of the experiment do not provide a clean decay curve for the Group D transitions due to JUROGAM II time-resolution being of the order of 80 ns. In [Lonnroth86] Lönnroth *et al.* on the basis of time-delay curve analysis concluded that the 151 keV transition depopulates a $T_{1/2} \approx 80$ ns isomeric state. In this work, this half-life value is adopted for the $25/2^-$ state de-exciting by emission of the 152 keV γ ray.

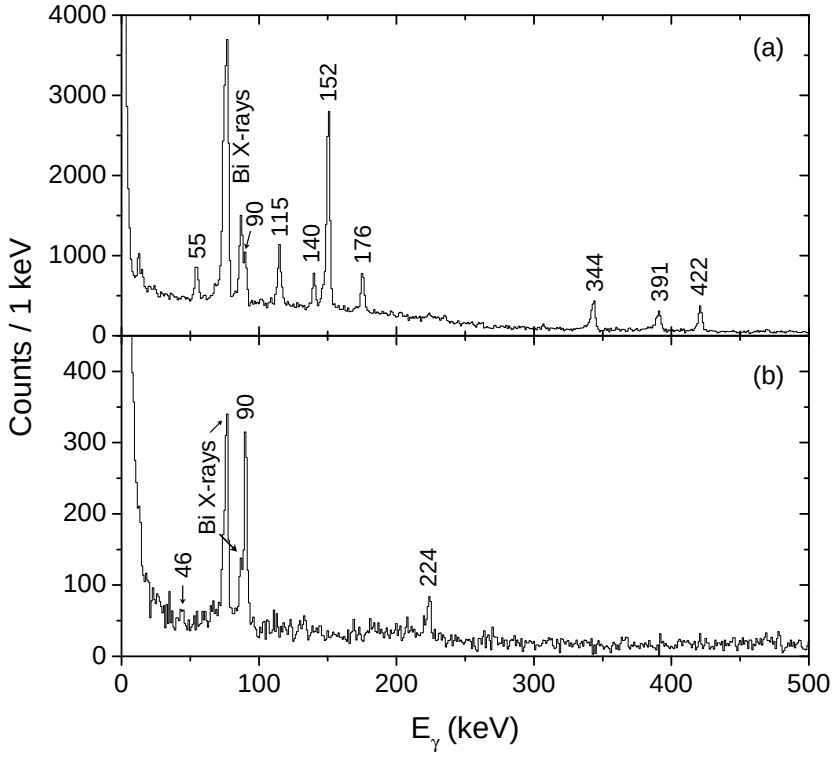

Figure 4.18: Gamma-ray spectra measured in the focal plane planar detector within 5 μs after the recoil implantation. (a) Sum of spectra gated with 434 and 454 keV prompt γ-ray transitions measured with JUROGAM II. (b) A spectrum gated with the 601 keV transition (Band 2) measured in focal plane clover detector.

When gating with the prompt 454 keV transition in the delayed-prompt γ-γ coincidence matrix, γ-ray transitions of Band 2 can be seen. Panel (b) of Fig. 4.18 shows the planar spectrum gated with the 601 keV transition (see Band 2 in Fig. 4.15) in the delayed γ-γ matrix. In this spectrum, the 90 keV transition is clearly visible. Additionally, none of the Group C or D transitions is seen in the spectrum. In the level scheme, the 90 keV transition is placed as depopulating the isomeric $25/2^-$ member of Group D and side-feeding Band 2. Approved by delayed γ-γ coincidence analysis, this placement implies an $E2$ character for the 90 keV transition.
Moreover, in Fig. 4.18(b), the 55 keV transition, observed when gating on the transitions above the isomer, is missing. Instead, a new low-energy transition with energy of 46 keV is observed. Low intensity of this transition does not allow for any further analysis of its character. Nevertheless, its energy is close

to the 49 keV transition placed as depopulating the $(29/2^-)$ isomeric state in ^{193}Bi (see Fig. 4.2). Finally, since no other γ-ray transitions are observed in Fig. 4.18, (similarly to ^{193}Bi) the 46 keV transition is tentatively associated with the decay of the $(29/2^-)$ isomeric state to $25/2^-$ member of Group D in ^{195}Bi. Based on the energy sum arguments, it places the $(29/2^-)$ isomeric state at an energy of 2.382 MeV in the level scheme (see Fig. 4.15). Subsequently, it implies an $E2$ character for the 46 keV transition.
Additionally, gating with the low-energy γ-ray transitions of Group D allows to identify transitions feeding structure of the $(29/2^-)$ isomeric state. In Fig. 4.19, a spectrum of prompt γ-rays measured with JUROGAM II and gated with the delayed 152 and 176 keV transitions in the delayed-prompt γ-γ matrix is presented. The structure of this spectrum proves the assumption made above that the 454 keV transition is the main feeding transition of the $(29/2^-)$ isomeric state.

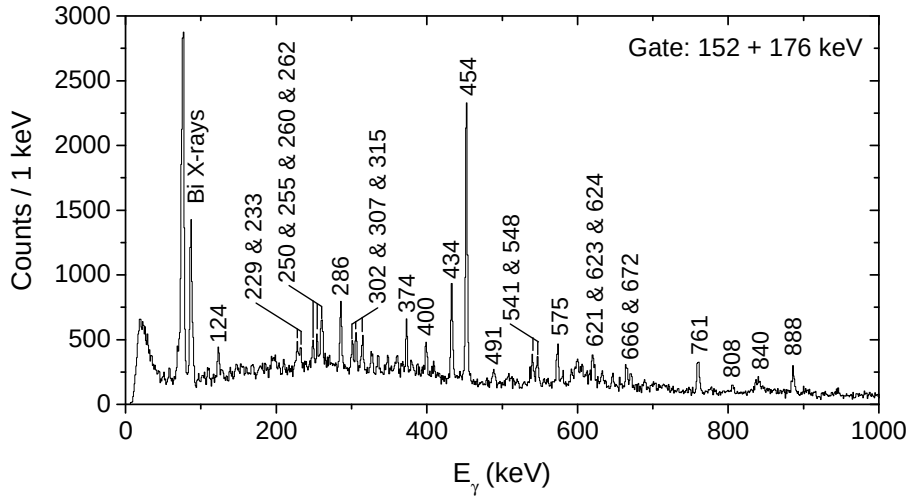

Figure 4.19: A spectrum of prompt γ-rays obtained when gating with the 152 and 176 keV transitions in the planar spectrum in ^{195}Bi experiment.

By projecting the time differences Δt (recoil - delayed γ) of the Group D transitions, a half-life of the $(29/2^-)$ state can be determined. In panel (a) of Fig. 4.21, the time-projection of the 152 keV γ-ray transition is shown. Using the exponential decay function to fit the Δt distribution results in a half-life value $T_{1/2} = 614(5)$ ns. Deviations of $T_{1/2}$ for other Group D transitions stay within the limit set by the uncertainty of the measured half-life.

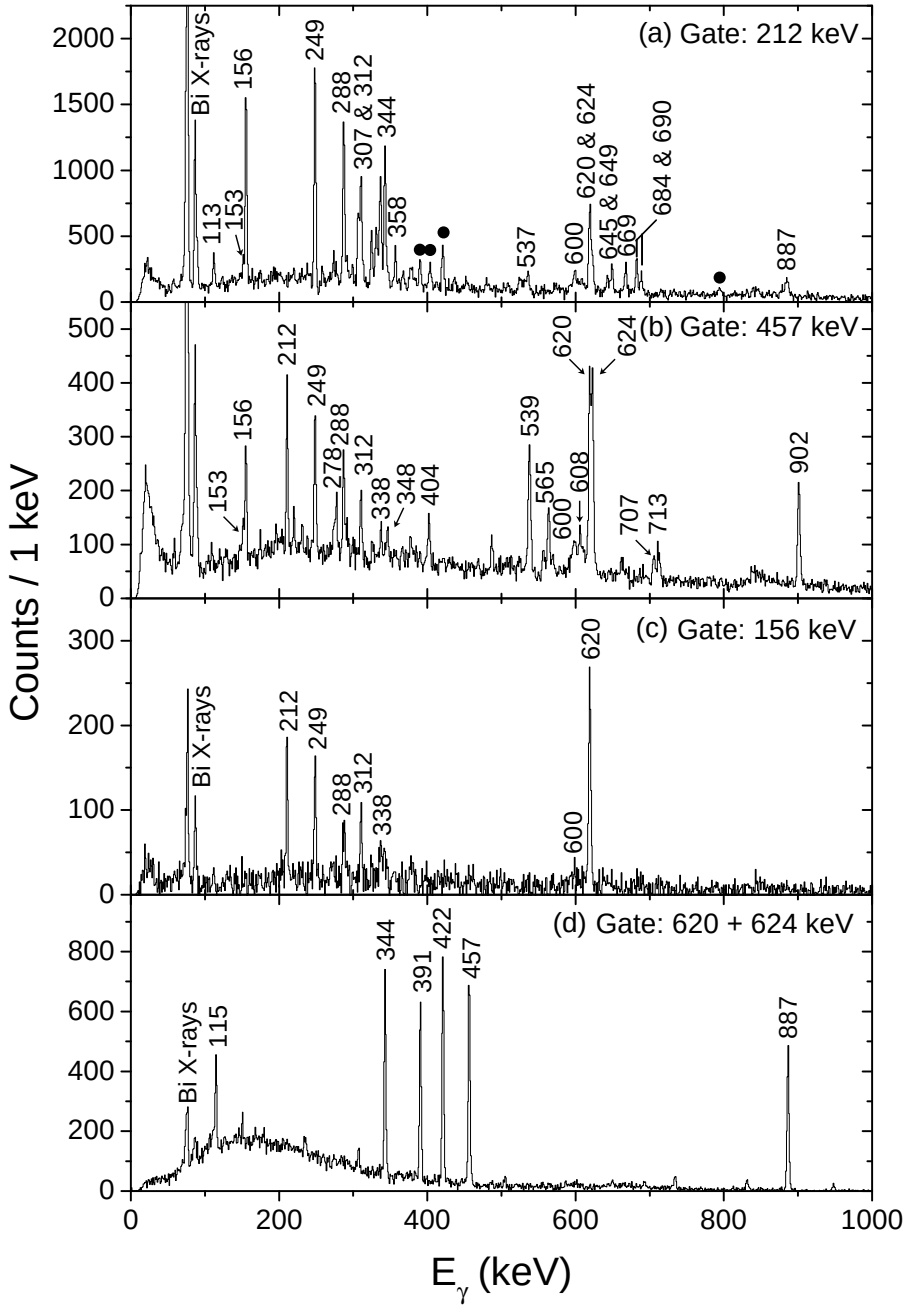

Figure 4.20: (a) A prompt γ-ray spectrum gated with the 212 keV transition. Circle symbols refer to γ-ray transitions in prompt coincidence with another 212 keV transition in ^{195}Bi (see Group B in Fig. 4.15). (b) A spectrum of prompt γ-rays gated with the delayed 457 keV transition in the delayed-prompt γ-γ coincidence matrix. (c) An isomer-tagged JUROGAM II spectrum, gated with the prompt 156 keV γ-ray transition. (d) A focal plane clover spectrum gated with the prompt 620 and 624 keV γ-ray transitions in the delayed-prompt γ-γ coincidence matrix.

One decay path of the $(29/2^-)$ isomeric state proceeds to Group C. Fitting the Δt time-projections of the 391 and 422 keV transitions, respectively, gives longer half-lives than the one measured for the $(29/2^-)$ isomeric state. This indicates an existence of another, longer living isomeric state in this nucleus. Gating on the transitions depopulating the states above $31/2^+$ member of Band 1 in the prompt γ-γ coincidence matrix reveals γ-ray transitions that do not belong to Band 1. Panel (a) of Fig. 4.20 displays a spectrum of prompt γ rays gated with the 212 keV transition and measured by JUROGAM II. Besides Band 1 transitions, three new γ-ray transitions with energies of 153, 620 and 624 keV can be seen in this spectrum. Transitions of the same energies are also observed in the prompt γ-ray spectrum gated with the delayed 457 keV transition in the delayed-prompt γ-γ coincidence matrix (see panel (b) of Fig. 4.20). The 457 keV transition is among the strongest transitions observed in the focal plane γ-ray spectra. However, it is not associated with the decay of the $(29/2^-)$ isomeric state. In Fig. 4.21(b), the time projection of the 457 keV γ-ray transition is presented, together with the measured half-life $T_{1/2} = 1.49(1)$ μs. This half-life is clearly distinct from the half-lives of other isomeric states present in this nucleus. It is evident that the 153, 620 and 624 keV γ-ray transitions are related to feeding of a new high-spin isomeric state in ^{195}Bi. The DCO analysis combined with the information obtained from the IPDCO analysis indicates a stretched $M1$ character to 153, 620 and 624 keV γ-ray transitions. The isomer-tagged prompt γ-ray spectrum gated with the 156 keV transition of Band 1, where a search-time window of 0 - 5 μs is used for selection of delayed γ-rays, confirms the conclusions made based on observations in Fig. 4.20(a) that Band 1 feeds a new high-spin isomeric state. Moreover, the 153 and 624 keV γ-ray transitions are not observed in Fig. 4.20(c). Therefore, they must originate in the decay of the $33/2^+$ member of Band 1. In addition, the 153 and 624 keV γ-ray transitions are found to be in coincidence. The 620 keV γ-ray transition is found to be in coincidence neither with the γ-ray transitions located below the $31/2^+$ member of Band 1 nor with the 153 or 624 keV γ-ray transitions. On the basis of γ-γ coincidences and energy-sum arguments, both 620 and 624 transitions are placed to directly feed a new isomeric state. As a result, the isomeric state with half-life of 1.49(1) μs is deduced to have a spin and parity of $I^\pi = 29/2^+$ and to locate at an energy of 2.615 MeV (see Fig. 4.15). Finally, a focal plane clover spectrum gated with the prompt 620 and 624 keV γ-ray transitions is presented in panel (d) of Fig. 4.20. The spectrum shows the γ-ray transitions involved in the decay-path of the $29/2^+$ isomeric state. The 457 keV γ-ray transition is identified to directly depopulate the isomeric state to $25/2^+$ state. Analysis of the backed target data confirms a stretched quadrupole multipolarity for the 457 γ-ray transition.

Among other important transitions already mentioned above, a high-energy 902 keV $E2$ transition is observed in γ-ray spectrum presented in panel (b) of Fig. 4.20. In contrary to observations for the 624 keV transition, no γ-ray transition at energy of 902 keV is observed either in panel (a) or panel (c) of Fig. 4.20. Hence, it must originate in the decay of the energy level located

above the non-yrast $I^{\pi} = 31/2^{+}$ state. The 902 keV $E2$ transition is identified to depopulate the non-yrast $I^{\pi} = 33/2^{+}$ state to $29/2^{+}$ isomeric state, and serves as an important building block in constructing the level structure labeled as Group E built on top of this long-lived isomeric state (see level scheme in Fig. 4.15).
Decay paths of both $29/2^{+}$ and $29/2^{-}$ isomeric states flow via members of Group C (for details see Fig. 4.15). Even though the energy difference of 233 keV between the $29/2^{+}$ and $(29/2^{-})$ isomeric states allows the existence of a measurable $E1$ transition, no connection between the two high-spin isomeric states is observed in the present data.

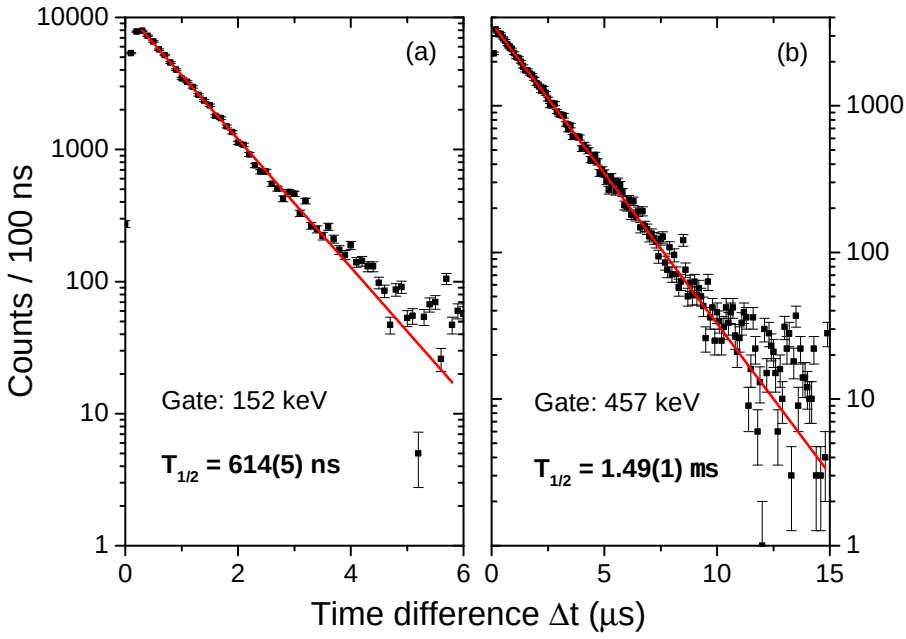

Figure 4.21: Time difference spectra of the recoil implantation and observation of the (a) 152 keV and (b) 457 keV transitions, respectively. The exponential decay curve is fitted to the data and is shown as the solid line through data points.

4.2.5 Bands 3 - 6

The $25/2^{+}$ state located at excitation energy of 2.159 MeV, besides the important role it plays in the decay-paths of both high-spin isomeric states, is also found to be the lowest state of a band-like structure (Band 3 in Fig. 4.15). Band 3 decays out via emission of a single 115 keV $E2$ transition. Due to weak

coincidences with the 360 and 645 keV intra-band transitions, the uppermost state of Band 3 is only tentatively placed at excitation energy of (4.071) MeV. The $(29/2^-)$ isomeric state turns out to be a band-head of a new band-like structure (Band 4). Among other transitions seen in Fig. 4.19, the transitions forming Band 4 are clearly recognized. Results of the DCO and IPDCO analyses are in agreement with the assignments of $M1$ and $E2$ characters, respectively, for most of the intra-band transitions. In this study, Band 4 is observed up to $I^\pi = (43/2^-)$ and an energy of 4.982 MeV.
In the JUROGAM II part of the present data, a cascade of five coincident low-energy γ-ray transitions with energies 169, 196, 229, 268 and 294 keV is found to be in coincidence with the 454 keV member of Band 4 and to feed the $(29/2^-)$ isomeric state. In addition, two weak $E2$ transitions with energies 497 and 563 keV are observed in the prompt γ-γ coincidence matrix. The two intra-band $E2$ transitions confirm an $M1$ character assigned to five low-energy γ-ray transitions. All together, they form a band-like structure Band 6 (see Fig. 4.15). In the present study, no connection to Band 4 is established.
In the same set of data, another set of transitions is identified to form a structure with characteristics similar to a rotational band (Band 5). No γ-ray transition is found to connect Band 5 with any member of Band 4. Level energies, together with spins and parities of the Band 5 members remain as well undetermined. However, prompt coincidences between Bands 5 and 6, respectively, and the 454 keV γ-ray transition feeding the $(29/2^-)$ isomeric state are observed in the isomer-tagged JUROGAM II γ-γ matrix. Therefore, the lowest members of both bands, even though floating, are placed above an excitation energy of 2.382 MeV.

4.2.6 Other transitions

Placed on the right to Band 2 in the ^{195}Bi level scheme (see Fig. 4.15) is the level structure labeled as Group F. In Fig. 4.17, a transition at 659 keV is marked. This transition does not belong to Band 2. However, it is observed to be in coincidence with no other transitions except those of Band 2. Therefore, it must be fed either by a very low-energy transition and/or by a transition depopulating an isomeric state. In the level scheme, the 659 keV transition is placed to depopulate $I^\pi = 21/2^-$ member of Group F (see Fig. 4.15). A low-energy 32 keV $E2$ transition is also tentatively placed to depopulate the $25/2^-$ member of Group D. The relatively high intensity of the 659 keV $E2$ transition can only be explained if the existence of the 32 keV γ-ray transition, placed as feeding the $21/2^-$ state, is considered. Especially the huge internal conversion coefficient $\alpha_{Th.}$(32 keV, E2) = 1333(19) [Kibedi08], together with the high energy threshold of the PIN diode detector makes it impossible to observe the 32 keV transition in the GREAT spectrometer.
A level structure labeled as Group G (see Fig. 4.15) is placed as side-feeding the

$(31/2^-)$ and $(33/2^-)$ members of Band 4. Energy level identification as well as their ordering within the group is done thanks to strong prompt coincidences with the 575 and 761 keV γ-ray transitions. Several strongest transitions of Group G, e.g. with energies of 302, 575 and 761 keV, can be seen in Fig. 4.19.

Chapter 5

Discussion

The ^{195}Bi isotope is 8 neutrons away from the neutron mid-shell. It is the reason why, until the present study, the ^{195}Bi nucleus was believed to posses very little collectivity. On the other hand, the nucleus ^{193}Bi is found to lie in a transitional region, since in the lighter Bi isotopes deformed structures dominate, whereas in the heavier isotopes the yrast structures can be explained assuming a spherical shape. That is why both collective oblate and spherical structures can be expected in ^{193}Bi. In the following section, the experimental data exhibiting an extensive manifestation of shape coexistence are presented. Such admixtures of structures are most likely the explanation for the richness of the level structures observed in both $A = 193$ and $A = 195$ Bi isotopes. Several observed level structures will be discussed. Most of these bands can be described by the coupling of an unpaired proton to the semi-magic lead core. Explanations in terms of aligned angular momenta i_x and comparisons of B($M1$)/B($E2$) ratios will be proposed.

5.1 Collective structures

5.1.1 $\pi \mathbf{i}_{13/2}$ band

In the mass region of the present study, sudden lowering of the $13/2^+$ level energies have been observed for bismuth isotopes, and is schematically shown in Fig. 5.1. The $13/2^+$ states are pushed down in energy due to their interaction with increasing number of neutron holes, which become available in more neutron-deficient nuclei by approaching the region away from the β-stability line towards neutron mid-shell. As presented in Fig. 5.1, the decrease

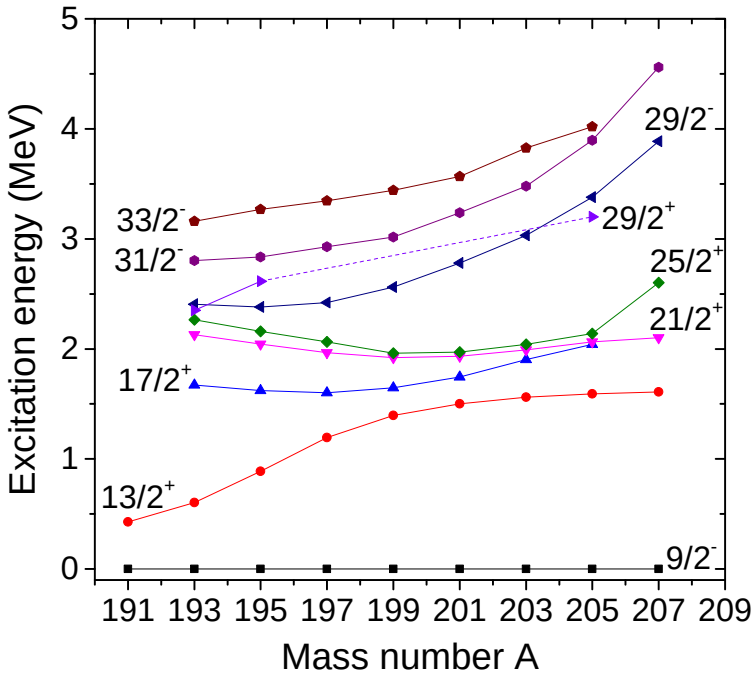

Figure 5.1: (Color online) Systematics of selected excited states in odd-A Bi isotopes. Where the exact excitation energy is not known due to unobserved low-energy transitions Δ, it is set to 40 keV for clarity. The data are taken from [Chapuran86, Mabala05] (^{197}Bi), [Piel85] (^{199}Bi), [Broda82, Piel85] (^{201}Bi), [Hubel78, Lonnroth82, Hubel83] (^{203}Bi), [Brock77, Lonnroth82, Hubel83] (^{205}Bi), [Bergstrom69, Lonnroth78, Lonnroth79] (^{207}Bi) and for ^{193,195}Bi from [Herzan15] and the present work.

of the $13/2^+$ level energies is especially apparent for the $A = 191 - 195$ bismuth isotopes. In those odd-A Bi nuclei, the $13/2^+$ states are found to have an isomeric character. Generally speaking, in the neutron-deficient bismuth nuclei with A $<$ 199, the $13/2^+$ isomeric states can be understood as the coupling of an $i_{13/2}$ proton to the oblate $2p$-$2h$ 0^+ intruder state of the neighboring even-even Pb core. Moreover, strongly-coupled rotational bands built on top of the $13/2^+$ isomeric states have been identified in ^{191,193,195}Bi isotopes [Nyman15, Nieminen04, Herzan15].

The smoothly increasing behavior of the transition energies of the resulting strongly coupled bands in ^{193,195}Bi built on top of the $13/2^+$ isomeric states terminates when the $25/2^+$ states are passed. In panels (a) and (b) of Fig. 5.2, the aligned angular momenta i_x as a function of the rotational frequencies for $i_{13/2}$ bands are presented. A sharp band-crossing takes place at $\hbar\omega \sim 0.2$ MeV, with about 10 - 11 $\hbar$ gain in alignment. For comparison, alignment plots for the

yrast bands in ^{190}Hg and ^{194}Po are shown in Fig. 5.2(c). In both Bi isotopes, the total gains in alignments in $i_{13/2}$ bands and the crossing-frequencies are consistent with those measured for ^{190}Hg and ^{194}Po. In these two even-even nuclei, the alignments have been attributed to the two $i_{13/2}$ neutrons, which is most likely the case also for Band 1. Sharp $i_{13/2}$ neutron alignments appear to be typical in this mass region for low and moderate oblate deformations. Both experimental and theoretical B($M1$)/B($E2$) ratios for Band 1 in ^{193,195}Bi are shown in panels (a) and (b) of Fig. 5.3. Theoretical calculations using parameters taken from [Nieminen04] nicely follow the trend given by experimental values, both below and above the band-crossings.

5.1.2 $\pi(\mathrm{f}_{7/2}/\mathrm{h}_{9/2})$ bands

In ^{193}Bi and ^{195}Bi, the yrast negative parity bands labeled as Band 2 are built on the 7/2[514] Nilsson configuration (mixed $\mathrm{h}_{9/2}/\mathrm{f}_{7/2}$). In ^{193}Bi nuclei, Band 2 has been observed up to spin $\mathrm{I}^{\pi} = (29/2^{-})$, which turns out to be the point with the maximum gain in the alignment brought by the $\mathrm{i}_{13/2}$ neutron pair in this rotational band. This is represented in panel (a) of Fig. 5.2 by the same trend in the evolution of i_x as a function of rotational frequency as in Band 1. In this case, the smooth increase of the $E2$ transitions energies ends at lower spin I = 23/2 (see Fig. 4.2). After the neutron $\mathrm{i}_{13/2}$ alignment, Band 2 is expected to be as yrast as Band 1. In the experiment of the present study, the band was not seen beyond the band crossing. For the configuration proposed for Band 2, the theoretical B($M1$)/B($E2$) ratios reproduce the experimental values very well (see Fig. 5.3(c)).
On the other hand, quite unfortunately, the information on Band 2 in ^{195}Bi is quite limited (see Fig. 4.15). Therefore, no major conclusions can be made by comparing measured values, plotted in panels (b) and (d) of Figs. 5.2 and 5.3, respectively, to those for ^{193}Bi. The uppermost state observed in the present study has spin I = 23/2, which is found to be insufficient for 2-neutron alignment, as shown in panel (b) of Fig. 5.2. In fact, sudden changes in $i_x(\omega)$ are noticeable. Additionally, the usual smooth increase of the $E2$ transition energies is not followed in the case of the favored signature band in ^{195}Bi. Considering panel (d) of Fig. 5.3, if the same deformation is assumed for Bands 2 in ^{193,195}Bi, the theoretical estimate for the B($M1$)/B($E2$) ratios does not follow the trend given by experimental points in ^{195}Bi. This may indicate that a sudden structural change occurs in Band 2 in ^{195}Bi already at rather low spin. Moreover, these observations suggest a smaller deformation for 7/2[514] proton orbital in ^{195}Bi.
In ^{193}Bi Band 4 seems to be similar to Band 2. As presented in panel (a) of Fig. 5.2, the extracted aligned angular momenta for Band 4 are slightly lower than those in Band 2. A configuration, where a proton occupies the 9/2[505] Nilsson orbital is assigned to this band. In addition, theoretical estimates for

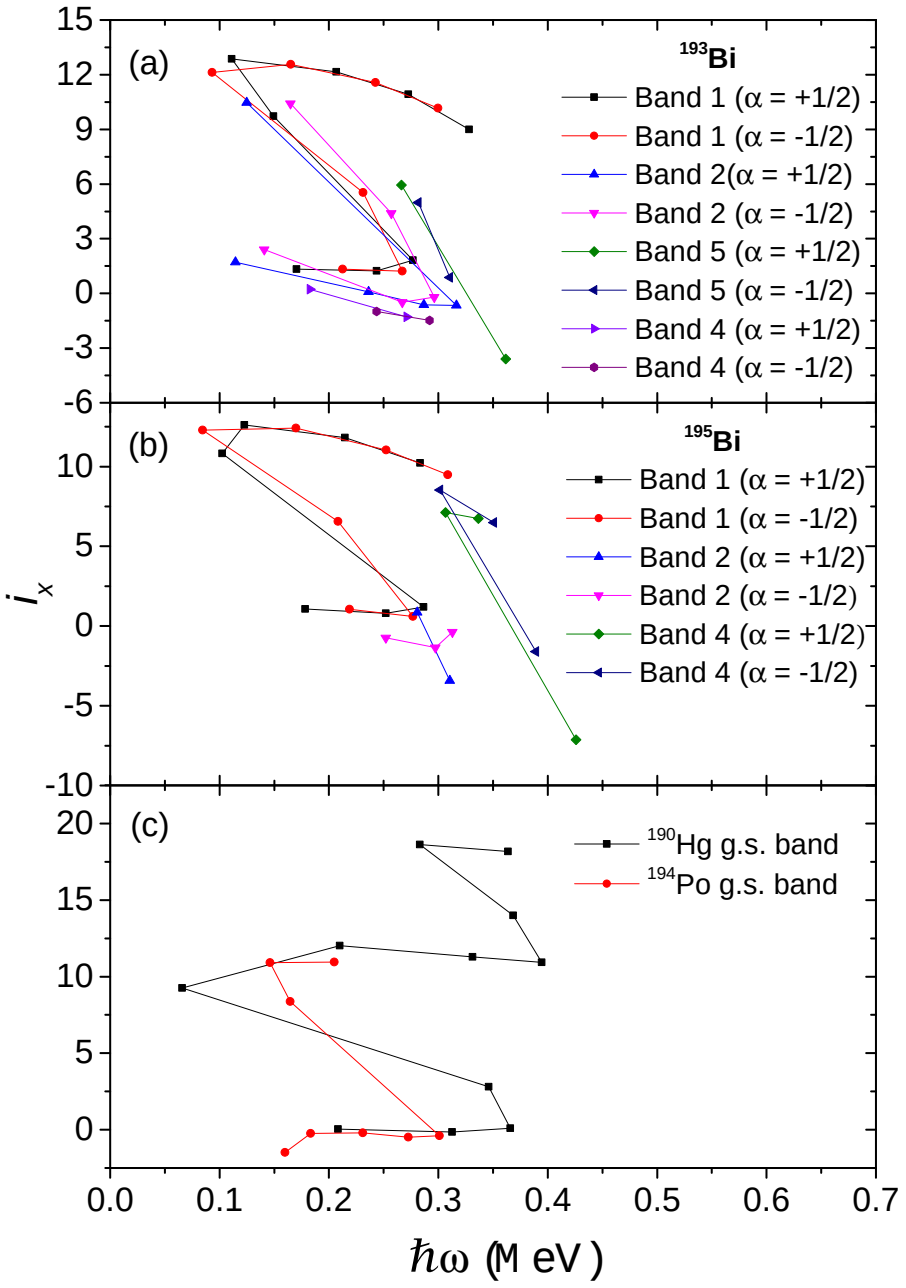

Figure 5.2: Aligned angular momenta i_x for the (a) favored ($\alpha = +1/2$) and unfavored ($\alpha = -1/2$) signatures of Band 1 ($\pi 13/2^+[606]$), Band 2 ($\pi 7/2^-[514]$), Band 4 ($\pi 9/2^-[505]$) and Band 5 in ^{193}Bi. (b) favored and unfavored signatures of Band 1 ($\pi 13/2^+[606]$), Band 2 ($\pi 7/2^-[514]$) and Band 4 in ^{195}Byi. (c) Yrast bands in ^{190}Hg [Bearden94] and ^{194}Po [Helariutta99]. In case of the Bi and Po isotopes, a reference with the Harris parameters $J_0 = 13\ \hbar^2/\mathrm{MeV}$ and $J_1 = 219\ \hbar^4/\mathrm{MeV}^3$ has been subtracted. Harris parameters $J_0 = 3\ \hbar^2/\mathrm{MeV}$ and $J_1 = 85\ \hbar^4/\mathrm{MeV}^3$ have been used for the rotational reference in ^{190}Hg.

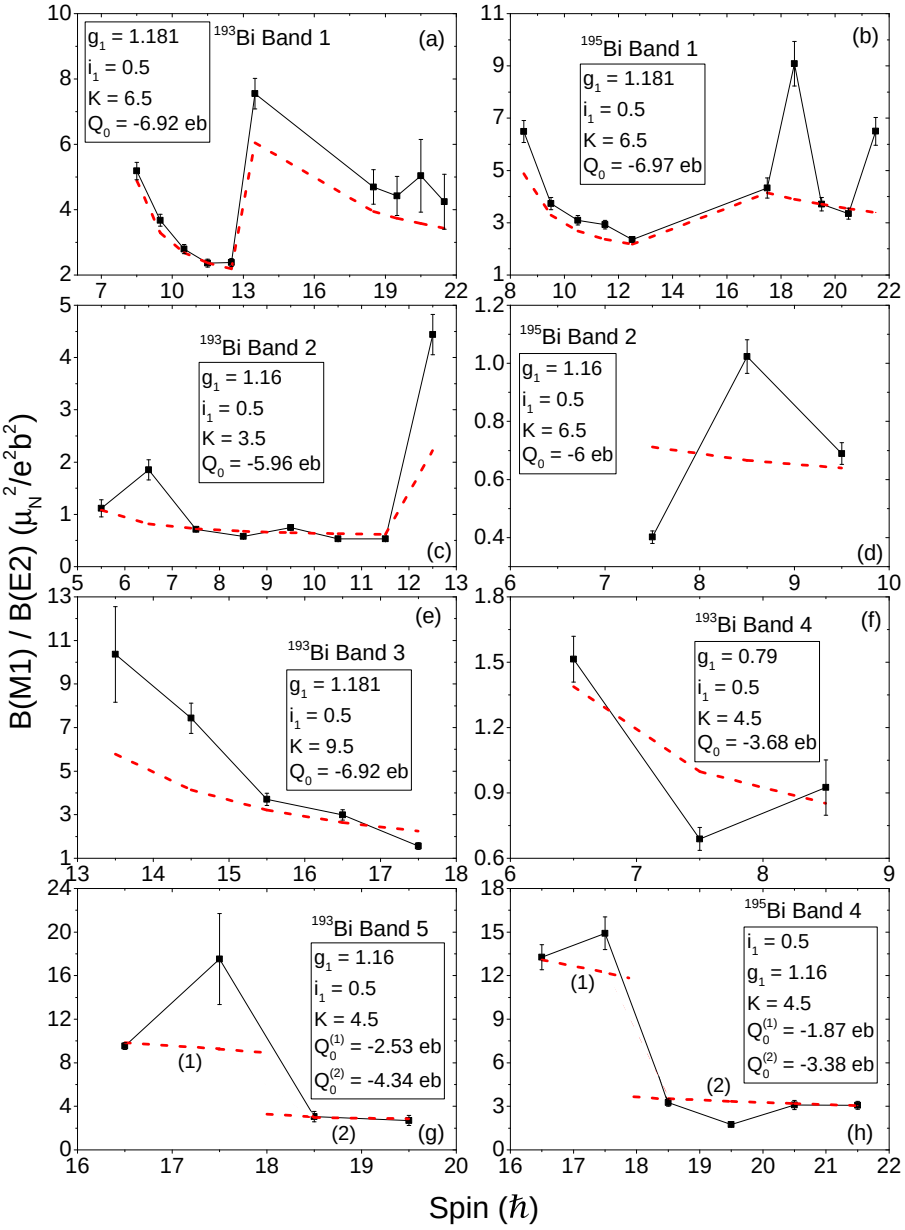

Figure 5.3: Experimental B($M1$)/B($E2$) ratios for (a) Band 1 (c) Band 2 (e) Band 3 (f) Band 4 (g) Band 5 in ^{193}Bi, and (b) Band 1 (d) Band 2 and (h) Band 4 in ^{195}Bi, together with semi-empirical estimates indicated by dashed red line. The parameter values for the odd proton used in the calculations are indicated.

the proposed configuration reproduce the experimental B($M1$)/B($E2$) ratios shown Fig. 5.3(f), even though a lower quadrupole moment has to be taken in the assumption compared to other bands in ^{193}Bi. A rotational band with the same configuration is not observed in ^{195}Bi.

5.1.3 Multi-quasiparticle configuration of Band 3 in ^{193}Bi

In the ^{193}Bi level scheme shown in Fig. 4.2, Band 3 is placed at relatively high excitation energy. The energy of the $19/2^-$ band-head, together with the assigned spin values for Band 3 members suggest it is most likely built on a 3-quasiparticle (qp) configuration. The aligned angular momenta plot for this band, among other bands in ^{193}Bi, is presented in Fig. 5.2(a). The gain of about 6 - 7 $\hbar$ in alignment with maximum possible K = 9.5 chosen is observed. Such an aligned angular momentum is understood as a presence of one $i_{13/2}$ neutron in the configuration. In Sec. 4.1, negative parity is assigned for Band 3. Hence a configuration with an $i_{13/2}$ proton and neutron coupled to a neutron occupying one of the negative parity orbitals close to Fermi surface is proposed. The 7^- and 9^- states in Po isotopes and their Pb isotones have been assigned with almost pure neutron 2 qp configurations, $\nu(i^{-1}_{13/2}p^{-1}_{3/2})$ and $\nu(i^{-1}_{13/2}f^{-1}_{5/2})$ for 7^- and 9^-, respectively [Helariutta99]. In the assumption of the same oblate deformation here as for $\pi i_{13/2}$ band, the calculated B($M1$)/B($E2$) ratios are found to reproduce the experimental values, especially at higher spin (see Fig. 5.3(e)). This remarkably good agreement is emphasized since Band 3 involves three quasi-particles in its configuration.

5.1.4 $1/2^+$ intruder states

The band-like structure (Band 6) in ^{193}Bi is built upon the $1/2^+$ proton intruder state, which is of *2p-1h* nature. The hole state determining the spin and parity of this intruder state is created by exciting a proton from $3s_{1/2}$ 1/2[400] Nilsson orbital to the $1h_{9/2}$ 9/2[505] Nilsson orbital (see Fig. 2.3). An oblate shape is attributed to such a configuration in odd-mass Bi nuclei [Nieminen04]. The oblate deformation of the nucleus, even though not significant, is sufficient enough to bring the 1/2[400] and 9/2[505] Nilsson orbitals closer to each other, so that the one proton excitation is energetically favorable.
As shown in Fig. 5.4 small increases in angular momenta alignments at low spins for ^{191,193}Bi are observed. Nyman *et al.* [Nyman15] attribute this gain in the alignment in ^{191}Bi to the crossing of a level structure with a lower deformation by a more deformed structure. This evokes a speculation that in ^{193}Bi a similar shape change occurs, but at a slightly higher rotational frequency.
Corresponding states have recently been observed also in ^{199,201}At [Auranen14] (see the level systematics therein for more details).

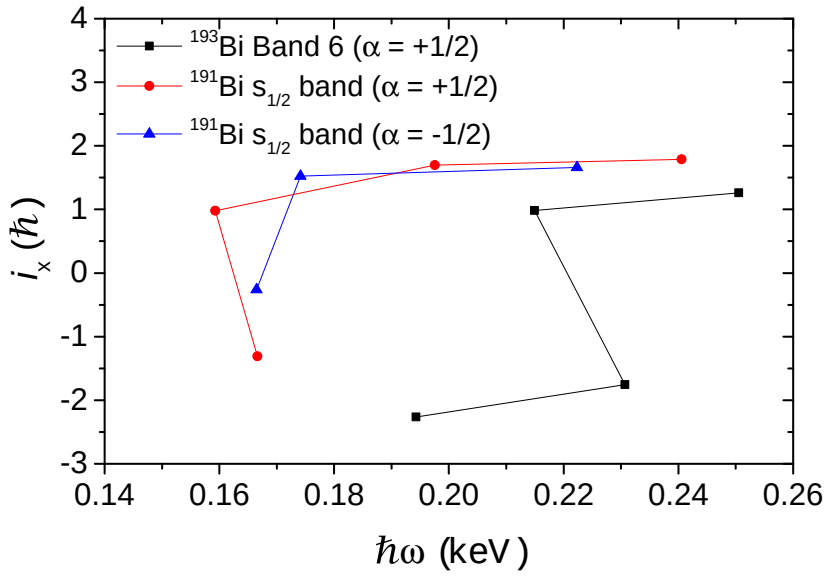

Figure 5.4: (Color online) Aligned angular momenta i_x for Band 6 in ^{193}Bi and the $s_{1/2}$ band in ^{191}Bi. Harris parameters $J_0 = 13\ \hbar^2/\text{MeV}$ and $J_1 = 219\ \hbar^4/\text{MeV}^3$ have been used for the rotational reference.

5.2 High-spin isomeric states

In the studies of heavier odd-A Bi isotopes, configurations of most of the high-spin isomeric states have been attributed to the coupling of an $h_{9/2}$ proton to the Pb core states [Lonnroth86, Lonnroth78, Lonnroth79, Lonnroth82]. When results of these systematic studies are taken in the assumption, the $29/2^-$ isomeric states in ^{193,195}Bi nuclei can be explained as members of the $\pi h_{9/2} \otimes \nu(i^{-2}_{13/2})_{12^+}$ multiplet [Piel85]. The same configuration is also assigned to the $31/2^-$ and $33/2^-$ states upon the $29/2^-$ isomeric state, respectively, which represent the maximum possible spin for such configuration. Starting from ^{193}Bi, the $29/2^-$ isomeric state keeps its isomeric character throughout the isotopic chain up to ^{207}Bi, where its energy is ~ 1.5 MeV higher, whereas the half-life drops down to $T_{1/2} = 12.7(9)$ ns [Lonnroth79]. A sudden change in the half-live of the $29/2^-$ isomeric states is actually noticeable already in the comparison of the two odd-A neighboring nuclei of the present study, where the $T_{1/2}$ is shorter by a factor of ~ 5 in ^{195}Bi. In both isotopes, this isomeric state decays to the $25/2^-$ state, which is also found to posses an isomeric character in ^{195}Bi. The $\pi h_{9/2} \otimes \nu(i^{-2}_{13/2})_{10^+}$ configuration is assigned for the $25/2^-$ state. Despite the fact that the energies of the transitions depopulating the $29/2^-$ isomeric states in ^{193,195}Bi are almost equal, the corresponding reduced transi-

tion strength B($E2$) = 0.255(5) W.u. in ^{195}Bi is five times larger than B($E2$) = 0.052(2) W.u. in ^{193}Bi [Herzan15]. Both reduced transition strengths seem to be slightly hindered when compared to 0.466 W.u. and 0.160 W.u. for the corresponding $12^+ \rightarrow 10^+$ isotone core transitions in ^{194}Pb [Kaci02] and ^{192}Pb [Plompen93], respectively. However, they both follow the gradually increasing trend given by the experimental values of their Pb isotones. This can be seen in panel (a) of Fig. 5.5, which shows the B($E2$) values plotted against the neutron number. Based on the plotted values, we can try to extrapolate this information to heavier nuclei and get a rough estimate of B($E2$) = 0.46 W.u. for the decay of the $29/2^-$ isomeric state in ^{197}Bi. If we put this value against the reduced transition strength of 0.638 W.u. for the corresponding core transition in ^{196}Pb, even better agreement between the isotonic parters is observed.

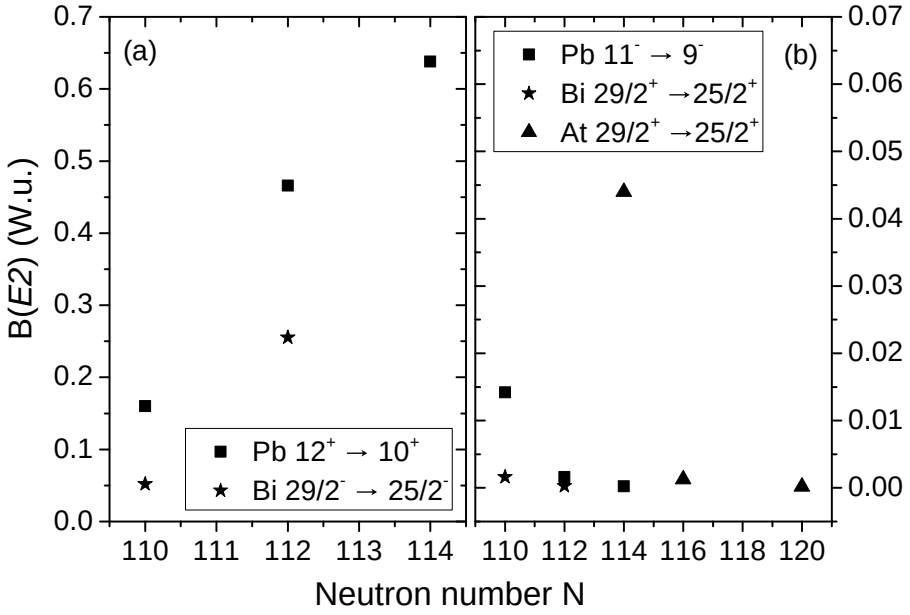

Figure 5.5: Experimental B($E2$) values for (a) the transitions depopulating the $29/2^-$ isomeric states in ^{193,195}Bi [Herzan15], and $12^+ \rightarrow 10^+$ core transitions in ^{192}Pb [Plompen93] and ^{194}Pb [Kaci02], respectively, and (b) the $29/2^+ \rightarrow 25/2^+$ transitions in ^{193,195}Bi [Herzan15], $11^- \rightarrow 9^-$ transitions in ^{192}Pb [Plompen93], ^{194}Pb [Kaci02], ^{196}Pb [Dracoulis05] isotopes, and ^{199,201,205}At [Auranen15] isotopes. Data for ^{195}Bi are from the present work. Consider the very fine scale of the y-axis of panel (b).

Band 5 in ^{193}Bi (see Fig. 4.2) has the same quasiparticle configuration as Band 2 after the neutron $i_{13/2}$ alignment. The same configuration is also assigned to

Band 4 in ^{195}Bi (see Fig. 4.15). An aligned angular momenta plot for this band is shown in panel (b) of Fig. 5.2. There is not enough experimental points for Band 2 in ^{195}Bi, but i_x of Band 5 can easily be compared with the i_x values of Band 2 in ^{193}Bi, presented in Fig. 5.2(a). The gain of about 10 $\hbar$ in the alignment, previously attributed to two $i_{13/2}$ neutron alignment, is apparent also here. Almost spherical shape is assumed for the few lowest members of Band 5 (^{193}Bi) and Band 4 (^{195}Bi), respectively. Panels (g) and (h) of Fig. 5.3 show the experimental B($M1$)/B($E2$) ratios for these two bands. In order to follow the experimental measured values, a change in deformation must be assumed for both bands. These adjustments of nuclear shape are represented by two different values of quadrupole moments denoted as $Q_0^{(1)}$ and $Q_0^{(2)}$. The superscripts (1) and (2) indicate the regions of spin values which a certain Q_0 value is applied to (see Fig. 5.3(g,h)). The experimental data indicate that both bands become more rotational-like with increasing spin, represented by lowering of the intra-band transition energies (see Figs. 4.2 and 4.15). It occurs as a direct consequence of increasing moment of inertia of the rotating nucleus. It remains to be seen in future experiments whether there are connections to Band 2 from the uppermost levels of Band 5 in ^{193}Bi and Band 4 in ^{195}Bi, respectively.

Owing to the excitation energy, the $29/2^+$ isomeric states in ^{193}Bi and ^{195}Bi have 3 qp configurations. High-spin states in neutron-deficient odd-A Bi isotopes were under intense investigation in the late 1970's and early 1980's, mainly studies performed by Lönnroth *et al.* [Lonnroth78, Lonnroth79, Lonnroth82, Lonnroth86] and Hübel *et al* [Hubel78, Hubel83]. However until now, no corresponding isomeric states have been reported. In heavier odd-A Bi isotopes the yrast $21/2^+$ and $25/2^+$ states are well known. Systematic behavior of these states is shown in Fig. 5.1. They have been found to remain isomeric up to ^{207}Bi [Bergstrom69, Lonnroth78, Lonnroth79]. However, no firm evidence for an isomeric character of these two states in very neutron-deficient ^{193,195}Bi nuclei is acquired in the present study. In heavier odd-A neighbors, these $21/2^+$ and $25/2^+$ isomeric states were previously explained as a $\pi h_{9/2}$ coupled to 7^- and 9^- states in Pb isotones [Piel85]. Such quasi-particle configurations cannot give rise to an isomeric state with spin of I = 29/2.

Isomeric states with a spin and parity of $I^\pi = 29/2^+$ have been reported in several proton-rich odd-A At isotopes [Bergstrom70, Sjoreen76, Davie84, Jakobsson10, Auranen15]. In literature, the $\pi(i_{13/2}h_{9/2}^2)$ configuration assignment is given to these isomeric states. Jakobsson *et al.* [Jakobsson10] reason that the $29/2^+$ state becoming isomeric is a direct consequence of the major difference between the two configurations, that of the $29/2^+$ isomeric state and the states due to coupling of the odd $h_{9/2}$ proton to the negative parity states below the 11^- isomer in the Po core.

In this study, the same configuration is proposed for the $29/2^+$ isomeric states in ^{193,195}Bi. In contrast to the previously discussed At isotopes, the excitation of a proton pair across Z = 82 shell gap is necessary in order to build such

configuration in Bi nuclei. This means that an extra energy must be brought into the system, which may also explain the higher excitation energies of these states in ^{193,195}Bi nuclei. Quite unfortunately, no corresponding state has yet been observed in the At isotones. Acting as a parent-α nucleus of ^{195}Bi, ^{199}At is the nearest At isotope, in which the $29/2^+$ isomeric state has been observed [Jakobsson10]. The reduced transition strength 0.044 W.u. for an $E2$-type γ-ray decay of this isomeric state was reported. One order of magnitude smaller reduced transition strength $1.26(4) \times 10^{-3}$ W.u. has been deduced for the $E2$ transition depopulating the $29/2^+$ isomer in ^{201}At [Auranen15E]. The experimentally observed 457 keV $E2$ transition depopulating the $29/2^+$ isomeric state in ^{195}Bi has a reduced transition strength $2.73(5) \times 10^{-4}$ W.u.. Similarly, in ^{193}Bi a B($E2$) value of $1.6(1) \times 10^{-3}$ W.u. corresponding to the $29/2^+ \rightarrow 25/2^+$ 84 keV $E2$ transition is measured [Herzan15]. This B($E2$) value is found to be perfectly overlapping with the value of reduced transition strength 1.6×10^{-3} W.u. for the corresponding $E2$ transition for the $11^- \rightarrow 9^-$ isomeric decay in ^{194}Pb [Kaci02]. Furthermore, the reduced transition strengths for the corresponding $E2$ transitions in ^{192}Pb and ^{196}Pb are 1.42×10^{-2} W.u. [Plompen93] and 2.1×10^{-4} W.u. [Dracoulis05], respectively. As shown in panel (b) of Fig. 5.5, a similar increasing trend of B($E2$) values as in Pb isotopes is also observed for At isotopes (see *e.g.*, Ref. [Auranen15] and refs. therein). Therefore, one can speculate that rather similar B($E2$) value as in ^{193}Bi and ^{194}Pb will also be observed in ^{197}At. Questionable is also the existence of the $29/2^+$ isomeric state in even lighter odd-A Bi isotopes, and whether the decays proceed via emission of an $E2$ γ rays, together with continuation in the upward trend of the corresponding reduced transition strengths towards proton dripline.

To conclude, it seems that the $29/2^+$ isomeric state in neutron-deficient odd-A Bi isotopes is a result of coupling of the $i_{13/2}$ proton to the oblate $8^+[\pi h^2_{9/2}]$ state in ^{192}Pb. As can be seen in Fig. 5.1, with the information available at the time of this study the $29/2^+$ level energies follow the trend given by the $13/2^+$ level systematic. Such configuration would be in agreement with the configuration proposed by Nieminen *et al.* [Nieminen04] for an isomeric weakly oblate band with $K = 29/2$. Even though there the coupling of the $h_{9/2}$ proton to Pb_{11^-} core state was suggested. In the study of ^{197}Bi [Chapuran86], an isomeric state with $T_{1/2} = 209$ ns and placed at energy of 2928 keV has been tentatively assigned with $I^\pi = (31/2^-)$. The 864 keV transition was placed to depopulate this isomeric state to $25/2^+$ state. Energywise, the $(31/2^-)$ level fits well to the energy systematics of the $29/2^+$ isomeric state in odd-A Bi isotopes shown in Fig. 5.1. If the assumption is made that the $(31/2^-)$ isomeric state in ^{197}Bi has a spin and parity of $I^\pi = 29/2^+$, then the reduced transition strength 8.195×10^{-5} W.u. is obtained for the corresponding 864 keV $E2$ transition. This would again be in agreement with the observed downward trend of the B($E2$) values as a function of increasing neutron number for Pb, Bi and At isotopes as presented in Fig. 5.5(b).

In ^{193}Bi, the $31/2^+$, $33/2^+$, $35/2^+$ and $37/2^+$ states at 2959, 3304, 3886 and

4272 keV, respectively, are interpreted as members of the band on top of the $29/2^+$ isomeric state. The negative parity states in Group E (see Fig. 4.2) can possibly arise from coupling of the $29/2^+$ isomeric state state to the 7^- and 9^- states ($\nu i_{13/2}p_{3/2}$ and $\nu i_{13/2}f_{5/2}$ configurations) [Helariutta99, Lagrange91] in even-even neighbors. Our knowledge of the level structure upon this isomeric state in ^{195}Bi (see Group E in Fig. 4.15) is rather limited. One way or another, the parity change is observed also there. It only appears at slightly higher spin. The same structural change of those states are taken in the assumption as in ^{193}Bi.

The de-excitation path from Band 1 to $29/2^+$ isomeric state observed in both the ^{193,195}Bi nuclei is surprising, since configurations of Band 1 and Group E are so different. The $31/2^+$ state in the level structure built on top of the isomeric state is only 5 keV apart from the $31/2^+$ state in Band 1 in ^{193}Bi (see Fig. 4.2). It is natural to expect a mixing of these two states. Following this intuitive guess, from the intensities of the 154 and 158 keV $M1$ transitions it is possible to estimate the amount of mixing assuming a simple two-state mixing model. The basic wave functions of the two $31/2^+$ states are products of the $\pi i_{13/2} \otimes \nu i^2_{13/2}$ ($\mid 1\rangle$ oblate) and $\pi i_{13/2}h^2_{9/2}$ ($\mid 2\rangle$ oblate) configurations. The two mixed $31/2^+$ states can be written as

$$\begin{aligned} \mid 31/2^+_1\rangle &= \alpha \mid 1\rangle + \beta \mid 2\rangle, \\ \mid 31/2^+_2\rangle &= \beta \mid 1\rangle - \alpha \mid 2\rangle, \end{aligned} \tag{5.1}$$

with $\alpha^2 + \beta^2 = 1$. The mixing amplitudes deduced from the experimental ratio of B($M1$) probabilities, $\frac{B(M1,158)}{B(M1,154)} = \frac{\beta^2}{\alpha^2} = 0.077$, are $\alpha = 0.96$ and $\beta = 0.27$. This implies an interaction energy of 1.3 keV, which corresponds to an energy shift of 0.085 ΔE$_u$ between the perturbed and unperturbed $31/2^+$ level energies. The ΔE$_u$ denotes the unperturbed splitting. Such an interaction energy is consistent with the mixing of two structures built on very different configurations. Finally, assuming experimentally observed 5 keV perturbed splitting results in ΔE$_u$ = 4.27 keV, hence indicating a very weak mixing of the aformentioned configurations.

In ^{195}Bi, the experimental ratio $\frac{B(M1,153)}{B(M1,156)} = 0.193$ gives the following mixing amplitudes: $\alpha = 0.92$ and $\beta = 0.40$. The interaction energy is 1.1 keV and corresponds to an energy shift of 0.239 ΔE$_u$. Considering the observed perturbed splitting ΔE$_p$ = 3 keV, the unperturbed splitting ΔE$_u$ = 2.03 keV is extracted from the experimental data in ^{195}Bi. The interaction energies deduced for mixing of the two $31/2^+$ states in ^{193,195}Bi are consistent with those observed in ^{163}Er between rotational bands built on different three-qp configurations [Hagemann97].

5.3 Non-collective states

Several positive parity states, belonging to Groups C in ^{193,195}Bi (see Figs. 4.2 and 4.15), can be interpreted by the coupling of the odd proton in the $h_{9/2}$ orbital to spherical negative parity core states in ^{192}Pb and ^{194}Pb, respectively. From the theoretical point of view, this has been done by using the cluster interaction approach [Piel85, Chapuran86]. Systematic behavior of these states is presented in Fig. 5.1. This approach yields good results especially for the $17/2^+$, $21/2^+$ and $25/2^+$ (member of Band 3 in ^{195}Bi) states. In both odd-A Bi nuclei of the present study, the second $13/2^+$ states can be understood as a proton occupying the spherical $i_{13/2}$ orbital. Energies of these levels are similar to the $13/2^+$ states in heavier odd-A Bi isotopes. Additionally, the $I^\pi = 13/2^-$ state, which locates at 1067 keV and 1200 keV in ^{193}Bi and ^{195}Bi, respectively, is attributed to the coupling of an $\pi h_{9/2}$ to a spherical ^{192,194}Pb$_{2^+}$ core states. In the level schemes discussed in this work, many other non-collective states with wide range of spin values and excitation energies can be seen to exist, however they cannot be easily explained.

5.4 Superdeformation

Considering odd-A Bi nuclei, SD bands have been observed in isotopes with $A = 191 - 197$ [Nyman15, Herzan15, Clark95, Clark96]. Theoretical calculations predict the $\pi i_{11/2}$ $1/2^+$ [651] orbital to be the lowest configuration in the SD minimum for odd-A Bi isotopes [Nazarewicz89, Satula91]. The properties of the previously observed single SD bands in ^{195,197} Bi nuclei are best reproduced if the odd proton occupies the [651]1/2 (α = -1/2) orbital [Clark96]. The SD band in ^{193}Bi observed in the present study is assigned with the favored signature of the theoretically predicted configuration. No signature partner band ($\alpha = +1/2$) has been found in odd-A Bi nuclei, apart from ^{191}Bi [Nyman15]. The SD band observed in ^{193}Bi is almost identical to the more strongly populated SD band (SD1, α = -1/2) in ^{191}Bi. The transition energies are less than 2 keV higher in ^{193}Bi. Moreover, a striking agreement is emphasized between the SD band in ^{193}Bi and the SD band 4 in ^{193}Tl, similarly interpreted as the negative signature of the [651]1/2 proton orbital [Bouneau98]. In this case, at lower rotational frequencies, the transition energy differences are below 1 keV. Predictions place the SD minimum at a lower excitation energy in this mass region than anywhere else. According to calculations performed by Hilaire and Girod [Hilaire07], in Bi isotopes a more pronounced SD minimum located at $\sim$2 MeV starts to appear in ^{188}Bi. In the calculations, the excitation energy is found to increase as a function of neutron number. Concerning ^{193}Bi, such a secondary minimum should be located at $\sim$ 2.4 MeV. In the α-tagged spectrum (see Fig. 4.12(b)), no transitions of band upon the $1/2^+$ intruder state

are present. This (non)observation offers an option that the intensity remains in the SD band down to the lowest possible spins. In the SD band observed in ^{193}Bi and built on the $1/2^+[651]$ configuration, the two lowest transitions, which are expected to have energies of about 87 and 46 keV, are not observed. Besides, if the 87 keV transition exists, it would be overlapping with a Bi X-ray peak located at 87.4 keV in the energy spectrum. Additionally, the internal conversion coefficients for the 46 and 87 keV $E2$ transitions are large, $\alpha_{tot,th}$ = 261(4) and $\alpha_{tot,th}$ = 12.82(18) [Kibedi08]), respectively, making these low-energy γ-ray transitions almost impossible to observe in the α-tagged energy spectrum shown in Fig. 4.12(b). It is taken into assumption that the intensity flows via these two transitions to the $3/2^+$ band head. Either the $3/2^+$ or the $1/2^+$ state is the lowest state for the configuration considered for the SD band observed in this work. As presented in Fig. 4.14, the 1836 keV γ-ray transition is found to be in coincidence with a couple of SD band transitions in ^{193}Bi data tagged on the α decay of the $1/2^+$ intruder state. Summing up the energies of the 1836 keV transition and the $1/2^+$ intruder state gives the total energy of 2.143 MeV that is reasonably close to the aforementioned position of the SD minimum predicted for ^{193}Bi.

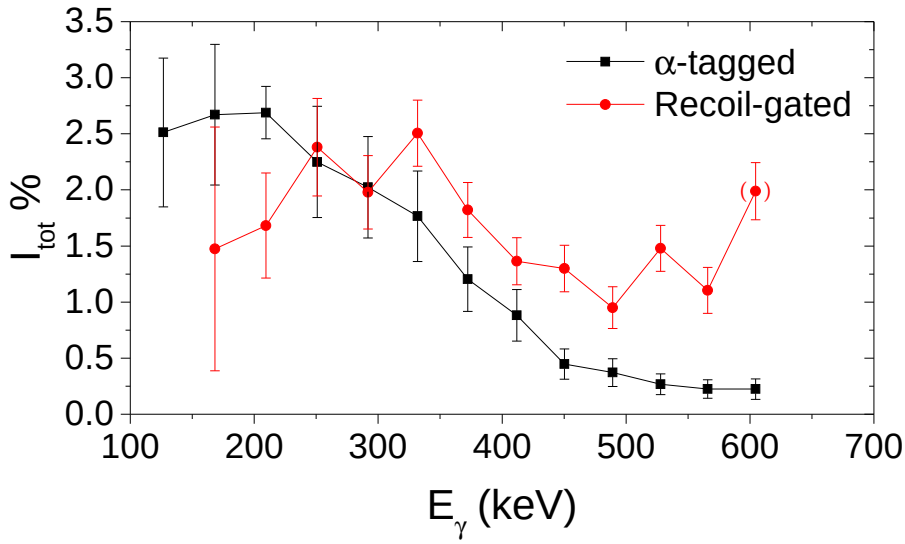

Figure 5.6: (Color online) Relative transition intensities of the γ rays in the SD band of ^{193}Bi as obtained from (black) the α-tagged γ-γ coincidence matrix gated on the sum of transitions (see Fig. 4.12(b)) and (red) recoil-gated γ-γ-γ cube. The data are normalized to the yield of the 323.4 keV transition of Band 1 in ^{193}Bi (see Fig. 4.2).

Finally, the ^{193}Bi SD band can be seen in both α-tagged γ-γ and recoil-gated γ-γ-γ coincidence data. However, the γ-ray intensity patterns are different for α-tagged and recoil-gated sum spectra, respectively (see Fig. 5.6), indicating that the observed SD band also feeds other states than those culminating in the $1/2^+$ isomeric state. It is not possible to identify corresponding transitions, as the RDT technique providing clean γ-ray energy spectra cannot be employed for the $9/2^-$ ground state due to its long half-life of 67 s.
In the present work, an SD band was also searched for in ^{195}Bi. However, no evidence is found in high-fold γ-ray data.

Chapter 6

Summary and future perspectives

In summary, excited states in ^{193,195}Bi have been observed using various tagging techniques. In ^{193}Bi, the previously known level structures were extended and new structures were revealed. Several structures can be understood assuming an oblate deformation, while some others require a spherical shape. Also, a rotational band showing properties typical for SD bands was identified. A candidate for a transition connecting the SD band with the $1/2^+$ proton intruder state was proposed. Using the GREAT spectrometer, new long-lived isomeric states having $I^\pi = 29/2^+$ were found in both the ^{193}Bi and ^{195}Bi. They are assumed to be associated with the $\pi(h^2_{9/2}i_{13/2})$ configuration. The $29/2^+$ isomeric states de-excite via hindered 84 and 457 keV $E2$ transitions in ^{193}Bi and ^{195}Bi, respectively, to the $25/2^+$ states of $\pi h_{9/2} \otimes \nu(i_{13/2}f_{5/2})$ parentage. In this work, the excitation energy of another isomeric state with $I^\pi = 29/2^-$ in ^{193}Bi could be determined. This state is associated with the $\pi h_{9/2} \otimes \nu(i^2_{13/2})_{12^+}$ configuration. An isomeric state with the same configuration was also identified to exist in ^{195}Bi. The delayed 46 keV $E2$ transition was tentatively assigned with the decay of this isomeric state.

No high-spin states, except those related to superdeformed shape, were observed in the study of ^{191}Bi [Nyman09]. The observations of the high-spin isomeric states in ^{193,195}Bi nuclei call for a search of these states in even more neutron-deficient Bi isotopes. It will be interesting to see whether the $29/2^+$ isomeric states continue to follow the excitation energies of the deformed $13/2^+$ states in lighter odd-A Bi isotopes. Even though the fusion-evaporation reaction cross-section for producing the ^{195}Bi nuclei is higher than for the ^{193}Bi

nuclei, no sign of the SD band was found in the recoil-gated high-fold γ-ray data. This indicates that the SD band in less populated in ^{195}Bi when compared to ^{191,193}Bi.

Bibliography

[Alvarez93] C. Rossi Alvarez, Nucl. Phys. News **3**, 10 (1993).

[Andersson76] G. Andersson, Nucl. Phys. A **286**, 205 (1976).

[Andreyev04] A.N. Andreyev *et al.*, Nucl. Instr. and Meth. A **533**, 422 (2004).

[Auranen14] K. Auranen *et al.*, Phys. Rev. C **90**, 024310 (2014).

[Auranen15] K. Auranen *et al.*, Phys. Rev. C **91**, 024324 (2015).

[Auranen15E] K. Auranen *et al.*, Phys. Rev. C **92**, 039901(E) (2015).

[Bearden94] I.G. Bearden *et al.*, Nuclear Physics A **576**, 441 (1994).

[Beausang92] C. W. Beausang *et al.*, Nucl. Instrum. Methods Phys. Res., Sect. A **313**, 37 (1992).

[Bengtsson79] R. Bengtsson and S. Frauendorf, Nucl. Phys. A **327**, 139 (1979).

[Bergstrom69] I. Bergström *et al.*, Phys. Rev. **181**, 1642 (1969).

[Bergstrom70] I. Bergström *et al.*, Phys. Scr. **1**, 243 (1970).

[Bouneau98] S. Bouneau *et al.*, Phys, Rev. C **58**, 3260 (1998).

[Brock77] R. Brock *et al.*, Nucl. Phys. A **278**, 45 (1977).

[Broda82] R. Broda *et al.*, Nucl. Phys. A **389**, 366 (1982).

[Carpenter90] M.P. Carpenter *et al.*, Phys. Lett. B **240**, Is. **1-2**, 44 (1990).

[Chapuran86] T. Chapuran et al., Phys. Rev. C **33**, 130 (1986).

[Chasman89] R.R. Chasman *et al.*, Phys. Rev. Lett. B **219**, 227 (1989).

[Clark95] R.M. Clark *et al.*, Phys. Rev. C **51**, R1052 (1995).

[Clark96] R.M. Clark *et al.*, Phys. Rev. C **53**, 117 (1996).

[Coenen85] E. Coenen *et al.*, Phys. Rev. Lett. **54**, Issue **16**, 1785 (1985).

[Cullen98] D.M. Cullen *et al.*, Phys. Rev. C **58**, 846 (1998).

[Davie84] R.F. Davie *et al.*, Nucl. Phys. A **430**, 454 (1984).

[Donau87] F. Dönau, Nucl. Phys. A **471**, 469 (1987).

[Dracoulis05] G. Dracoulis *et al.*, Phys. Rev. C **72**, 064319 (2005).

[Duchene99] G. Duchene *et al.*, Nucl. Instrum. Methods Phys. Res., Sect. A **432**, 90 (1999).

[Frauendorf81] S. Frauendorf, Phys. Lett. B **100**, 219 (1981).

[Galindo93] A. Galindo-Uribarri *et al.*, Phys. Rev. Lett. **71**, 231 (1993).

[Gamow28] G. Gamow, Z. Phys. **51**, 204 (1928).

[Gauvin72] H. Gauvin *et al.*, Phys. Rev. Lett. **29**, 958 (1972).

[Georgiev93] A. Georgiev and W. Gast, IEEE Trans. Nucl. Sci. **40**, 770 (1993).

[Gurney28] R.W. Gurney, E.U. Condon, Nature **122**, 439 (1928).

[Hagemann97] G.B. Hagemann *et al.*, Nucl. Phys. A **618**, 199 (1997).

[Harris65] S.M. Harris, Physical Review **138**, 509 (1965).

[Helariutta99] K. Helariutta *et al.*, Eur. Phys. J. A **6**, 289 (1999).

[Henry91] E.A. Henry *et al.*, Z. Phys. A - Hadrons and Nuclei **338**, 469 (1991).

[Herzan15] A. Herzáň *et al.*, Phys. Rev. C **92**, 044310 (2015).

[Heyde81] K. Heyde *et al.*, Phys. Rep. **102**, 291 (1981).

[Hilaire07] S. Hilaire and M. Girod, Eur. Phys. J. A **33**, 237 (2007).

[Hubel78] H. Hübel *et al.*, Nucl. Phys. A **294**, 177 (1978).

[Hubel83] H. Hübel *et al.*, Z. Phys. A **314**, 89 (1983).

[Hurstel02] A. Hürstel *et al.*, Eur. Phys. J. A **15**, 329 (2002).

[Jakobsson10] U. Jakobsson *et al.*, Phys. Rev. C **82**, 044302 (2010).

[Julin01] R. Julin, K. Helariutta, and M. Muikku, J. Phys. G **27**, R109 (2001).

[Kaci02] M. Kaci *et al.*, Nucl. Phys. A **697**, 3 (2002).

[Kibedi08] T. Kibedi *et al.*, Nucl. Instrum. Methods Phys. Res. A **589**, 202 (2008).

[Klein29] O. Klein and Y. Nishina, Z. Phys. **52**, 853 (1929).

[Krane73] K.S. Krane, R.M. Steffen and R.M. Wheeler, Nucl. Data Tables **11**, 351 (1973).

[Krane88] K.S. Krane, *Introductory nuclear physics.*, John Wiley & Sons, Inc. (1988). ISBN 978-0-471-80553-3.

[Krasznahorkay98] A. Krasznahorkay *et al.*, Phys. Rev. Lett. **80**, 2073 (1998).

[Krieger92] S.J. Krieger, P. Bonche, M.S. Weiss, Nucl. Phys. A **542**, 43 (1992).

[Lagrange91] J.M. Lagrange *et al.*, Nucl. Phys. A **530**, 437 (1991).

[Lauritsen92] T. Lauritsen *et al.*, Phys. Rev. Lett. **69**, 2479 (1992).

[Lazarus01] I.H. Lazarus *et al.*, IEEE Trans. Nucl. Sci. **48**, 567 (2001).

[Lee02] J.H. Lee *et al.*, J. of Korean Phys. Soc. **40**, 793 (2002).

[Leino81] M. E. Leino, S. Yashita, and A. Ghiorso, Phys. Rev. C **24**, 2370 (1981).

[Leino95] M. E. Leino *et al.*, Nucl. Instrum. Methods. Phys. Res. B **99**, 653 (1995).

[Lonnroth78] T. Lönnroth and B. Fant, Physica Scripta **18**, 172 (1978).

[Lonnroth79] T. Lönnroth, J. Blomqvist, I. Bergström and B. Fant, Physica Scripta **19**, 233 (1979).

[Lonnroth82] T. Lönnroth, Z. Phys. A **307**, 175 (1982).

[Lonnroth86] T. Lönnroth *et al.*, Phys. Rev. C **33**, 1641 (1986).

[Mabala05] G.K. Mabala *et al.*, Eur. Phys. J. A **25**, 49 (2005).

[Mayer50] M.G. Mayer, Phys. Rev. **78**, 16 (1950).

[McNabb96] D.P. McNabb *et al.*, Phys. Rev. C **53**, 541 (1996).

[Nazarewicz89] W. Nazarewicz, R. Wyss, and A. Johnson, Nucl. Phys. A **503**, 285 (1989).

[Newton67] J.O. Newton *et al.*, Nucl. Phys. A **95**, 357 (1967).

[Nieminen04] P. Nieminen *et al.*, Phys. Rev. C **69**, 064326 (2004).

[Nilsson95] S.G. Nilsson, I. Ragnarsson, *Shapes and shells in nuclear structure.*, Cambridge University Press, 1st edition (1995). ISBN 0-521-37377-8.

[Nyman09] M. Nyman, *Shape coexistence in light bismuth and astatine isotopes - an in-beam and decay spectroscopic study*, Research report No. 12 (2009). ISBN 978-951-39-3717-1.

[Nyman15] M. Nyman *et al.*, Eur. Phys. J. A **51**, 31 (2015).

[Pai12] H. Pai *et al.*, Phys. Rev. C **85**, 064317 (2012).

[Page03] R.D Page *et al.*, Nucl. Instr. and Meth. B **204**, 634 (2003).

[Paul95] E.S. Paul *et al.*, Phys. Rev. C **51**, 78 (1995).

[Piel85] W.F. Piel, Jr. *et al.*, Phys. Rev. C **31**, 2087 (1985).

[Pilotte94] S. Pilotte *et al.*, Phys. Rev. C **49**, 718 (1994).

[Plompen93] A.J.M. Plompen *et al.*, Nucl. Phys. A **562**, 61 (1993).

[Radford95a] D.C. Radford, Nucl. Instrum. Methods Phys. Res. A **361**, 297 (1995).

[Radford95b] D.C. Radford, Nucl. Instrum. Methods Phys. Res. A **361**, 306 (1995).

[Rahkila08] P. Rahkila, Nucl. Instr. and Meth. A **595**, 637 (2008).

[Saren11] J. Sarén *et al.*, Nucl. Instr. and Meth. A **654**, 508 (2011).

[Satula91] W. Satula, S. Cwiok, W. Nazarewicz, R. Wyss, and A. Johnson, Nucl. Phys. A **529**, 289 (1991).

[Schiffer90] K. Schiffer and B. Herskind, Nucl. Phys. A **520**, 521c (1990).

[Schmidt86] K.H. Schmidt *et al.*, Phys. Lett. B **168**, 39 (1986).

[Schmidt00] K.H. Schmidt, Eur. Phys. J. A **8**, 141 (2000).

[Scholey01] C. Scholey *et al.*, Phys. Rev. C **63**, 034321 (2001).

[Schuck97] C. Schück *et al.*, Phys. Rev. C **56**, 1667 (1997).

[Simon86] R.S. Simon *et al.*, Z. Phys. A **325**, 197 (1986).

[Singh96] B. Singh, R.B. Firestone and S.Y.Frank Chu, Nuclear Data Sheets **78**, Issue **1**, 1 (1996).

[Sjoreen76] T. P. Sjoreen *et al.*, Phys. Rev. C **14**, 1023 (1976).

[Starosta99] K. Starosta *et al.*, Nucl. Instr. Meth. Phys. Res. A **423**, 16 (1999).

[Tarantin71] N.I. Tarantin *et al.*, Sov. J. Nucl. Phys. **12**, No. **3**, 248 (1971).

[Weisskopf51] V.F. Weisskopf, Phys. Rev. **83**, 1073 (1951).

[Wilson03] A.N. Wilson *et al.*, Phys. Rev. Lett. **90**, 142501 (2003).

[Wilson05] A.N. Wilson *et al.*, Eur. Phys. J. A **24**, 179 (2005).

[Yamazaki67] T. Yamazaki, Nuclear Data A **3**, 1 (1967).